Morphology and Placement Control of Microdomain Structure in Block Copolymer Thin Film for Fabricating Ultra High Density Pattern

Yasuhiko Tada

2012

Table of Contents

CHAPTER1 GENERAL INTRODUCTION

1.1 Background and Objective of This Thesis

Lithography technology is a method to form fine patterns by transferring a geometric pattern from a photo mask to photo resist on a substrate. The technology has strongly supported the development of semiconductor industry. However, it is difficult for current conventional lithography technique to make patterns at dimensions below ca. 40 nm because of the diffraction limit of light and the rapidly increasing cost. Many studies have suggested the alternative techniques to maintain the progress of semiconductor industry. In the International Technology Roadmap for Semiconductors roadmap 2011, directed self-assembly is introduced as a technology which satisfy requirements for 16 nm node.[1]

Directed self-assembly (DSA) is generally recognized as an efficient method using self-assembling system, such as block copolymers (BCPs),[2-5] nanoparticles,[6–8] anodization of aluminum,[9–12] and DNA[13–15] for patterning on length scales that are difficult for current lithography to achieve. In particular, DSA of BCPs has attracted much attention for next generation lithography technique due to their ability to make fine patterns at nano-meter scale.

BCPs can be simply defined as the polymers being formed by connecting two or more chemically different polymer chains with a covalent bond at their ends. The BCP phase separate within the polymer chain as called “microphase separation” and self-assemble to form periodic structures, which are known as “microdomain structures” because the covalent bond linking the blocks prevents the macroscopic phase separation. Typical dimensions of the microdomain structures range 5—100 nm scales, which can satisfy the requirements of semiconductor industry for the fabrication of further integrated circuits.

However, self-assembling system of BCPs have much challenges for practical use in electronics applications, such as magnetic storage media,[16–20] flash memory devices,[21]

semiconducor capacitors.[22,23] One of the key challenges is to control the placement and the feature of microdomain to create a specific structure, such as combinations of the line, jog, bend, and T-junction geometries.[27-30] Furthermore, when the microdomain structures of BCPs thin films are applied as a etch mask to transfer patterns to an underlying substrate, BCPs must have high etch contrast between the blocks.[20,31]

In particular, a next generation technology of magnetic storage media, namely bit-patterned media,[16,17] requires to fabricate isolated single domain magnetic islands. The domain spacing is calculated to be ≤20 nm scale all over disk to achieve recording density beyond 1 tera bits per square inch. Therefore, it is urgent that DSA technique of BCPs is established to attain bit-patterned media because it is difficult for current lithography to achieve such scale.

In this thesis, I apply DSA of diblock copolymers (diBCPs) to form ultra high density pattern for bit-patterned media. As described above, control of placement and morphology of microdomain structure in diBCP thin film are required to attain the high density pattern with the sufficient uniformity and placement accuracy. The key factors to control the morphology and placement are to clarify the interfacial energy between substrate surface and polymer chain, the conformational energy of polymer chain, the mobility of the polymer, and so on in the thin film. If these factors are understood fully, this can help us not only to achieve ultra high density pattern, but also to form complex patterns, such as jog, bend, and T-junction geometries. As described below Sections, I review factors to control the morphology and placement of the microdomain structures.

1.2 Phase Behavior of Block Copolymers

As described above, BCPs are formed by connecting two or more chemically different polymer segments covalently bound in a single chain.[32] The simplest BCP is diBCP consisting A and B polymer chain, as shown in Figure 1-1. When A and B polymer chain

are sufficient immiscible and have mobility for phase separating, diBCP can form a variety of morphologies such as a body centered lattice of spheres, hexagonally packed cylinders, and parallel-oriented lamellae in the thermodynamically equilibrium state, as shown in Figure 1-1.[33–36] Extensive studies have reported that these phase behavior of diBCPs is determined by the volume fraction of one of the blocks, f, and the strength of the repulsive interaction from both experimental and theoretical perspectives.[34,37–41] The repulsive interaction is characterized by the product χN, where χ is Flory-Huggins interaction parameter[42,43] and N is degree of polymerization in the diBCP. χ is inversely proportional to the temperature.

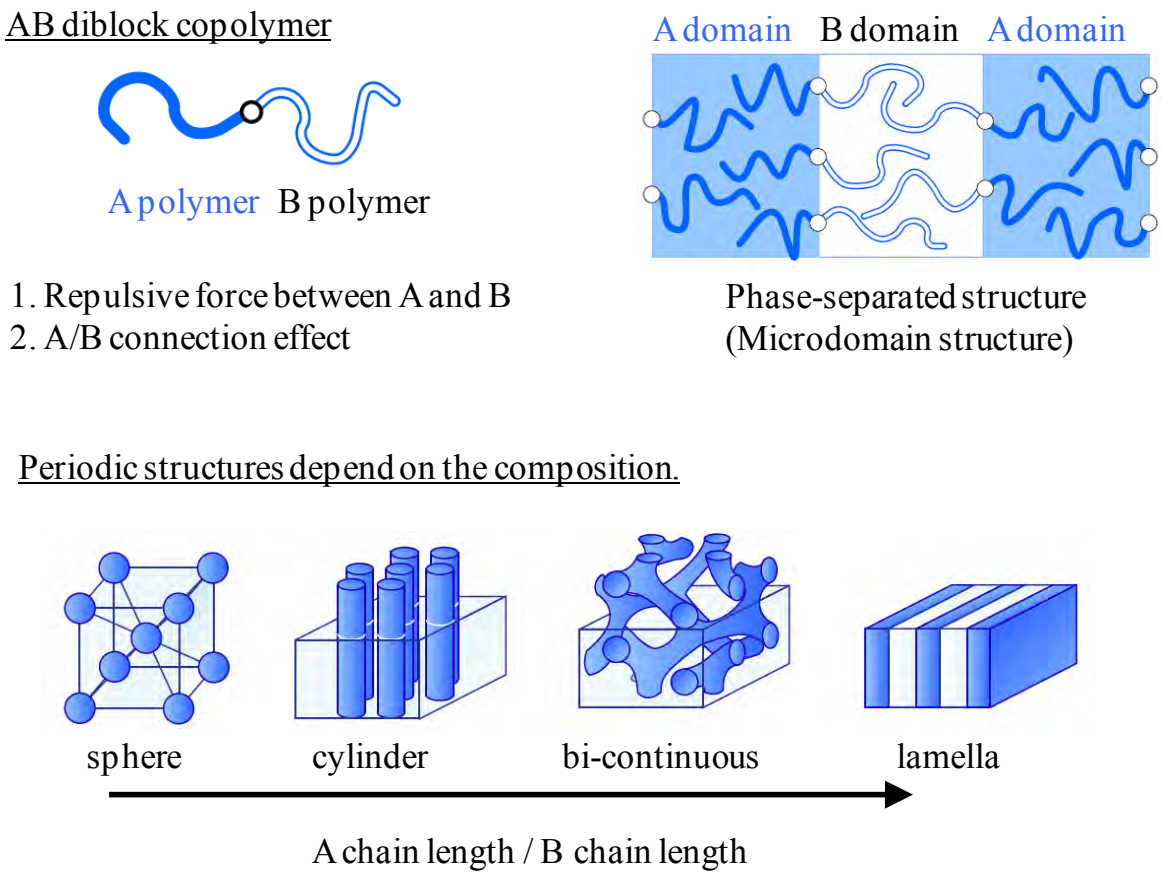

Figure 1-1. Schematic representation of the phases of AB diblock copolymer: spheres, cylinders, double gyroid, and lamellae.

Phase separation occurs when χN exceeds the critical value, $(\chi N)_c$. Most mixtures of homopolymers separate into macroscopic different phases in the thermodynamically equilibrium state. However, diBCPs can form microdomain structures because the covalent bond linking the blocks prevents the macroscopic phase separation. At the thermodynamically equilibrium state, this microphase separation is established by a delicate energy balance between the stretching energy for the polymer chains and the energy of interactions at the interface between A and B microdomains.

Matsen and Bates describe the phase diagram of thermal equilibrium morphologies of AB diBCPs by using self-consistent field theory (SCFT) with a mean field model.[44] Furthermore, Khandpur et al. experimentally investigated the morphology and obtained the phase diagram for the polystyrene-*block*-polyisoprene (PS-*b*-PI) diBCP system.[45] Figure 1-2 presents a theoretical and an experimental phase diagram of PS-*b*-PI. The phase diagrams show the dependence of morphology on the volume fraction, f. An order-disorder transition will occur when χN falls below a critical value, $(\chi N)_c$. For example, this transition occurs when the molecular weight of diBCP is very low, where N is very small, or temperature is very high, where χ is very small. In the case of symmetric diBCPs, the theoretical critical value in Figure 1-2 is 10.5. Recently, *Fddd* has been found as an equilibrium phase between lamellae and gyroid phases.[46]

Typical periodicity of microdomain structures formed by diBCPs ranges 5—100 nm. The upper limit of the periodicity depends on chain mobility because the formation of microdomain structure is limited by the high degree of entanglement and high χN in very large molecular weights of diBCPs. In the case of diBCPs with large molecular weight, it is difficult for the diBCPs to self-assemble to form microdomain structures on a practical time scale. Furthermore, the lower limit of the periodicity depends on the repulsive force, χN, between the two blocks. When the molecular weight of diBCP is very small, the repulsive force is too small to self-assemble to form microdomain structure.

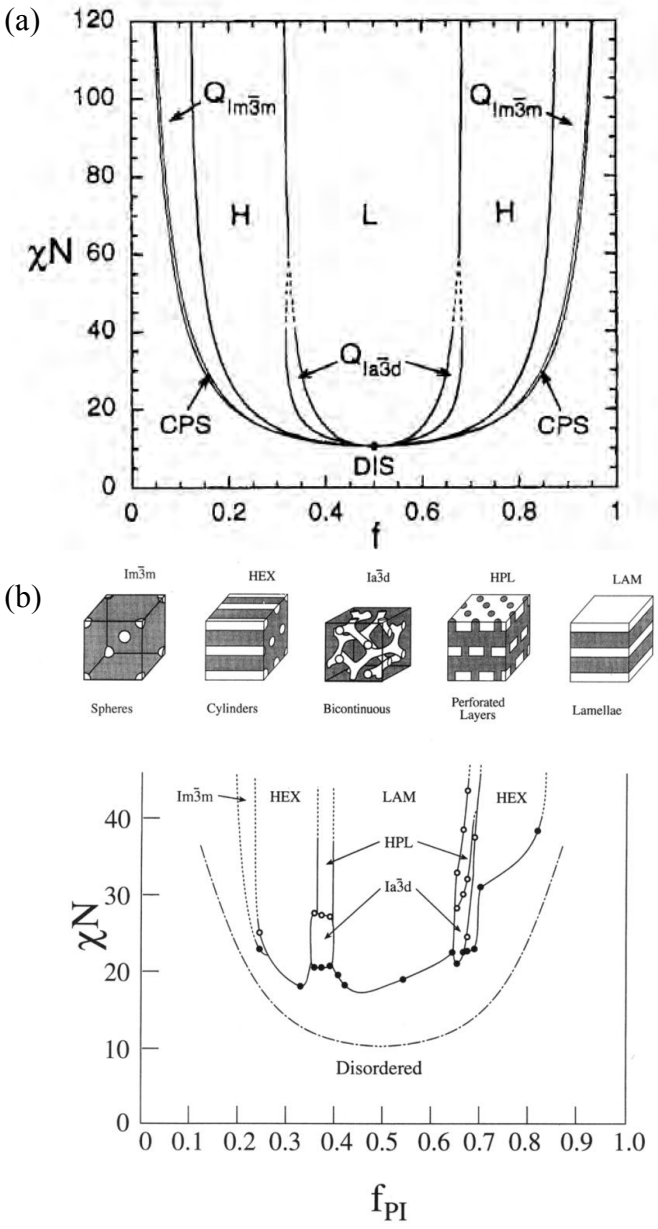

Figure 1-2. Phase diagram for diBCP. (a) Equilibrium morphologies predicted by using SCFT. Phase are labeled L (lamellae), H (hexagonal cylinders), $Q_{Ia\bar{3}d}$ (doubled gyroid), $Q_{Im\bar{3}m}$ (bcc sphere), CPS (close packed spheres), and DIS (disordered). Reprinted with permission from ref. 44, copyright 1996 American Chemical Society. (b) Experimental phase diagram of PS-*b*-PI diBCP. Phase are labeled LAM (lamellae), HPL (perforated layers), HEX (hexagonal cylinders), Ia3d (doubled gyroid), $Im\bar{3}m$ (bcc sphere). Reprinted with permission from ref. 45, copyright 1996, American Chemical Society.

The periodicity of microdomain structures depends on the molecular weight of the BCPs. The scaling law describes how the scale of microdomain structures depends on the segregation power, which is the strength of the repulsive force, χN, between two blocks. Although several groups have studied the scaling law by different theoretical approaches, all the theoretical predictions describe the molecular weight dependence of the natural period L_0, which is the domain spacing of microdomain structures, as the power law $L_0 \propto N^{\alpha}$.[38,41,47–49], The exponent α varies with the degree of phase separation. Hashimoto et al. experimentally demonstrated that in the strong segregation limit, where χN is large, for lamellar, cylindrical, and spherical morphologies, mean-field theory suggests that L_0 scales with $N^{2/3}$.[41] The interfacial width is significantly smaller than the domain spacing.

On the other hand, in the weak segregation limit, where χN is reduced to a value near the order-disorder transition point, L_0 scales as $N^{1/2}$, because spacing is closely related to the radius of gyration of the polymer chain. The region between the strong segregation limit and the weak segregation limit is denoted as intermediate segregation region. In the intermediate segregation region, the value of α theoretically varies from 0.72 to 1.017 and experimentally from 0.7 to 0.83.[50–52] Recently, Sivaniah et al. showed that on pure and blended symmetric poly(styrene-*b*-methacrylate) (PS-*b*-PMMA) thin films showed an exponent of 0.85 for BCPs in the ranges $40 < \chi N < 100$, which corresponds to the intermediate segregation region.[47]

1.3 Self-assembly in Thin Films

Many applications using BCPs as template require pattern transfer of the microdomain structures in the BCP thin films to substrates. Microdomain structures of BCPs in thin film are significantly different from that in bulk because the microdomain structures are quite influenced by both the film thickness and the interfacial interactions at the air/polymer and polymer/substrate interfaces. In this section, I focus on the microdomain structures of BCPs in the thin film with the thickness, t, equal to or larger than the bulk spacing.

1.3.1 General Process to Form Microdomain Structures

Spin coating is generally used as the most popular method to prepare thin films of BCPs on substrates. Typically, an excess amount of a solution of BCPs in a solvent, which is good solvent for BCPs and easily vaporized at room temperature, is placed on the substrates. Then, the substrates are rotated at 500 – 7,000 rpm to spread the solution by centrifugal force until the solvent in the solution is vaporized from the film. The film thickness, *t*, is easily controlled by the spin speed and the concentration of the solution. Then, the film is annealed to self-assemble to form microdomain structure. This annealing process increases the mobility of the BCP molecules for self-assembly. Therefore, the BCP molecules reach the final structure in the thermally equilibrium state. There are typical two methods in annealing process. One is thermal annealing and the other is solvent annealing, described in Section 1.4 for details.

1.3.2 Morphology of Thin Films

1.3.2.1 Interfacial Interaction

Generally, the interfacial interaction depends on blocks of different chemical composition. This leads to preferential wetting of each interface by selective blocks of the BCP. For example, in the case of PS-*b*-PMMA thin film on the native oxide surface of a Si substrate, the PMMA block wets the substrate surface, while the PS block wets the air interface because of the affinity of the polar PMMA block for the hydrophilic oxide surface and the lower surface energy of the nonpolar PS block. Russell and co-workers reported that the lamellae structures of the symmetric PS-*b*-PMMA on the native oxide surface of a Si substrate were oriented parallel to the surface.[53,54] Parallel orientation also occurs because of selective interactions in the case of the thin film of cylinder-forming PS-*b*-PMMA on a Si substrate with the native oxide. Therefore, selective interaction is quite important.

Turner first studied theoretically the equilibrium behavior of the lamella-forming symmetric BCP melt.[55] The lamellae structures are confined between two identical parallel plates with preferential attraction of the plates to one block of the polymer. For the symmetric system, he found that the configurations with a half-odd-integer number of layers occur only when the difference between the two polymer-plate surface tensions is small, and then only below some critical plate separation.

Walton et al. studied the orientation of BCPs as a function of interfacial interaction with blocks.[56] When walls are preferential for one of the blocks, BCPs form parallel oriented micorodomains. When both walls prefer same block, unfrustrated spacing occurs for wall spacing D, $D = nL_0$, which is the bulk spatial period L_0 multiplied by the number of layers n. Alternatively, when the walls attract opposite blocks, the unfrustrated system forms for wall spacing corresponding with $D = (n+1/2)L_0$. This behavior was confirmed experimentally with PS-*b*-PMMA sandwiched between two walls treated with random copolymers of polystyrene-*ran*-poly(methyl methacrylate) (PS-*r*-PMMA), with varying composition and thus varying block interaction.[57,58]

In thick film, competing effects can lead to mixed orientations of the morphologies. Konrad et al. studied the morphology of polystyrene-*block*-polybutadiene-*block*-polystyrene (PS-*b*-PB-*b*-PS) films on a Si surface, and found that the lamella structure of PS-*b*-PB-*b*-PI near the Si surface is oriented parallel to the substrate, but that mixed perpendicular and parallel orientation occurs near the air interface.[59] Xu et al. studied the structure of lamella-forming PS-*b*-PMMA in thick films confined between two walls modified by PS-*r*-PMMA random copolymers of varying composition.[60] Parallel oriented lamellae to the substrate was observed near the walls, and proceeds throughout the film thickness for thinner films. However, a mixed morphology is found for thicker films, with parallel orientation near the walls and perpendicular orientation far from the wetting influence of selective wall.

On the other hand, if the interaction between the substrate surface and blocks is less specific, perpendicular lamellae may be formed to eliminate the strain energy due to extended or compressed copolymer domains. Walton et al. predicted that neutral walls, lamella-forming block copolymers are expected to form perpendicular orientations for any plate spacing.[56] Pickett and Balasz found that for neutral walls, perpendicular morphology forms for all film thickness, and Monte Carlo simulations by Sommer et al. agree with this finding.[61,62] Kellogg et al. confirmed this behavior experimentally with PS-*b*-PMMA sandwiched between two walls modified with random copolymer brushes: nearly neutral walls formed perpendicular morphology.[58]

Surface neutralizing techniques have been used extensively to gain perpendicular orientation of both cylindrical and lamellar morphologies by eliminating preferential attraction of one block. In the case of substrate-supported films the polymer-air interface cannot be controlled, while the polymer-substrate interface can be done. In some cases, however, the energy effect from the substrate neutralization is enough to induce perpendicular orientation, though this effect largely breaks down for $D>L_0$.

1.3.2.1 Thickness dependence

In the case of lamella-forming PS-*b*-PMMA on the native oxide surface of a Si substrate, when the film thickness matches the repeat distance of the natural period of the microdomain structures of the BCP, L_0, the lamellar structures of alternating composition join the two interfaces. When the film thickness does not match the repeat distance of L_0, the mismatch causes the formation of the steps in the thin film. The steps are well-known as island and a hole formation, or terracing, which are formed to minimize the total energy by quantizing the

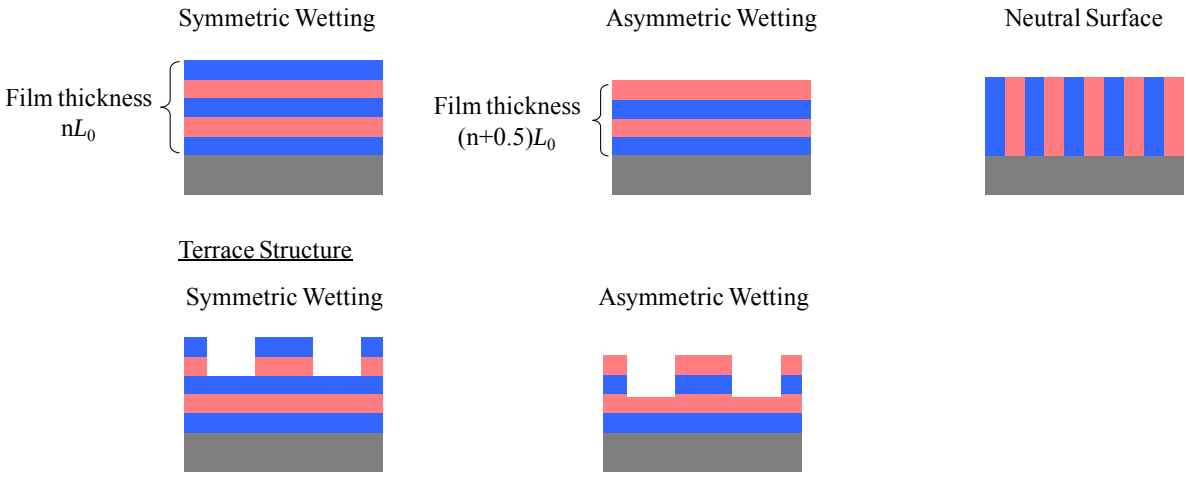

Figure 1-3. Orientation of lamellar domain in BCP thin film on various surface and dependence of orientation and structure on film thickness.

local film thickness. Figure 1-3 shows an island or a hole formation in lamella-forming PS-*b*-PMMA on a Si substrate with native oxide. On the other hand, for neutral conditions, lamellae structures oriented perpendicularly to the surface regardless of the film thickness.

Similar to the case of lamella-forming PS-*b*-PMMA, the orientation to the surface is induced if one component in diBCPs has a preferential affinity to substrate or air surfaces. However, because the composition of cylinder-forming diBCP is asymmetric, the affinity at surface area induces the interesting morphologies. If a surface has a preferential affinity to the minor component of the BCPs, the minor component covers the surface entirely and a brush layer along the surface is formed.[63] If there is no preferential affinity in the diBCP for air surface, the half cylinder is formed at $t = (n+1/2)d_0$, where d_0 is lattice spacing of cylinder microdomains).[64] If the terrace structures in thin films are formed, there are perpendicularly oriented cylinders and perforated lamellar structures at the edge of terrace structures.[64,65]

1.4 Annealing

BCPs are usually annealed to self-assemble to form microdoain structures. There are two annealing methods generally used. One is thermal annealing that is a simple process for self-assembly. The other is solvent annealing which has several parameters to form microdomain structure and tune the morphology of BCP.

1.4.1 Thermal Annealing

Self-assembly of BCPs occurs at an appreciable speed when the polymer chains gain sufficient mobility for self-assembly. In the case of thermal annealing, heating the BCP to temperatures above the glass transition temperature, T_g, for both blocks increases mobility of polymer chain for self-assembly. However, this annealing process cannot be applied when a BCP possesses either a high T_g or a low thermal degradation temperature.

Basically, the microdomain structure formed by thermal annealing is determined by the volume fraction, f, and the strength of the repulsive interaction, χN. In a weak segregation limit, however, the morphologies of BCPs with a single molecular weight could be controlled by heating the BCP because the Flory-Huggins interaction parameter, χ, decreases inversely with temperature ($\chi = A/T+B$). Therefore, the decrease of χ allows downward vertical movement in the phase diagram with increased temperature. This change of χ is reversible by lowering temperature. Leibler first predicted the thermoreversible order-order transition (OOT) between different kinds of the microdomain structures of a BCP in a weak segregation limit.[37]

In symmetric BCPs, the lamellar morphology shifts directly to a disordered state. In asymmetric polymers, such as cylinder forming BCPs, transitions from cylindrical to spherical morphology occur before the morphology becomes disordered. Sakurai et al. reported that the morphology of PS-*b*-PI with total number-average molecular weight (M_n) 82 kg/mol and 16% polystyrene changed from cylinders at 150°C to spheres at 200°C.[66]

Kimishima et al. also reported that the morphology of PS-*b*-PI with M_n 44 kg/mol and 20% PS underwent a transition from cylinders to spheres at 115-16.7°C.[67] Hajduk et al. observed a reversible transition between the lamellar an cylindrical morphologies in a polystyrene-poly(ethene-*co*-butene) diBCP.[68] Thermoreversible OOTs are only possible for a narrow range of polymer compositions. In that case, a polymer with low molecular weight or small segmental interaction, χ, was used to accelerate the kinetics of the transition and the temperature was limited between the T_g and the thermal degradation temperature for a polymer.

In the strong segregation limit, however, the interfaces between morphologies are nearly vertical in the phase diagram. Therefore, thermal annealing process cannot induce OOT. OOT require horizontal movement in the phase diagram, which is derived from a change in the relative volume fraction of the blocks. The change can be achieved by blending with homopolymers or other materials. It can also be achieved by annealing under a selective solvent. Solvent annealing is attractive due to the tunability after bulk or film casting. Solvent annealing is described in more detail next subsection 1.4.2.

1.4.2 Solvent Annealing

1.4.2.1 Polymer Mobility by Solvent Annealing

As mentioned above, self-assembly of BCPs requires sufficient mobility of polymer chain. Another method of increasing the mobility is to swell the polymer with a plasticizer (solvent), which lowers the T_g of the polymer to below room temperature or to easily achievable temperatures.[69] This process is called as solvent annealing. In particular, solvent annealing is useful for diBCPs which possess both high T_g and low degradation temperatures.

As described above in section 1.4.1, solvent annealing can induce the shifts in the phase behavior and periodicity of a BCP. Solvent annealing has more complications than thermal

annealing. However, it is also a useful tool for controlling the morphology and the periodicity. Furthermore, it can also form difficult-to-achieve morphologies.

When a polymer is swollen with a solvent to lower the T_g to below room temperature, the chain mobility is increased, and the BCP can self-assemble to form microdomain structure. Bueche gave the following equation for the T_g of a plasticized polymer

$$T_g = \frac{T_{gP} + (KT_{gS} - T_{gP})\phi_s}{1 + (K-1)\phi_s}$$

where T_{gP} is the glass transition temperature of the polymer, T_{gS} is the glass transition temperature of the solvent, ϕ_s is the volume fraction of solvent (plasticizer), and the constant K has values between 1 and 3 governed by

$$K \approx \frac{\alpha_{1S} - \alpha_{gS}}{\alpha_{1P} - \alpha_{gP}}$$

where α_l is the volume coefficient of expansion above T_g, while α_g is the volume coefficient of expansion below T_g. Reorganization of the equation for T_g of the plasticized polymer for the depression of T_g in the swollen film gives

$$\frac{T_{gP} - T_g}{T_{gP} - T_{gS}} = \frac{1 - \phi_P}{1 - \phi_P(1 - \frac{1}{K})}$$

where ϕ_p is the volume fraction of the polymer. Solvent T_{gS} values should be known. Actually this is the case for a few solvents only. However, the relationship between the T_g and the melting temperature, T_m, found for polymers can also be used to predict the T_{gS} form the freezing point of the solvent, T_{mS}:

$$\frac{T_g}{T_m} \approx \frac{2}{3}$$

appears to be valid. So if T_{gS} is unknown, $2/3T_{mS}$ may be used as a good approximation.

Zielinksi and Dula used a free-volume diffusion model to predict diffusion constants for mixtures of common solvents and polymers,[70] while Rauch and Köhler carefully investigated mass and thermal diffusion in PS/toluene solutions in the whole concentration range from

dilute to concentrated.[71] Both researches demonstrated that polymer diffusion increases as the T_g decreases upon addition of solvent. In other words, polymer chains can gain sufficient mobility for self-assembly at room temperature when the polymer chains are swollen with sufficient quantities of solvent. Mori et al. demonstrated that addition of nonselective solvent toluene to PS-*b*-PI led to depression of the PS block's T_g to below room temperature with 25% or more nonselective good solvent.[72]

Elbs et al. studied the thin film morphologies of BCPs after solvent annealing with variable solvents.[73] They applied the concept of the vitrification concentration to BCPs and found that the morphologies depends on the concentration. This dependence are explained qualitatively on the basis of concentration-dependent Flory-Huggins interaction parameters, χ, of the different components. Kim and Libera showed that cylinder-forming PS-*b*-PB-*b*-PS (PS cylinders form by thermal annealing) forms parallel hexagonal cylinders when the film was casted from solution by evaporating it slowly.[74] Compression in the direction of film thickness indicates that the film further shrinks after the polymer film reaches the vitrification concentration.

One of the key factors to consider is the effectiveness of solvent annealing with selective solvents. When a BCP film is swollen with a nonselective good solvent, the T_g of both blocks are suppressed and the BCP can gain the sufficient mobility for self-assembly by controlling the concentration. However, if a BCP film is swollen with a completely selective solvent, only the soluble block can be suppressed T_g, and the BCP cannot gain the sufficient mobility for self-assembly at room temperature. In the case of a solvent which dissolves both blocks but displays preferential swelling of one block, sufficient mobility for self-assembly cannot occur until the less soluble block swells enough for its T_g to lower below room temperature. In principle, the combination of thermal and solvent annealing techniques could lead to polymer mobility at moderate annealing temperatures. This is not very useful in practice because solvents are usually flammable.

As described above, solvent annealing with either nonselective or selective solvents can change the phase behavior of BCPs. In other words, the thermodynamically equilibrium state of a BCP under solvent vapor is different from that of a neat BCP. In the case of solvent annealing, the swollen state may be maintained upon evaporation of the solvent. After solvent evaporation, the BCP is no longer in a thermodynamically equilibrium state. When the T_g of the two blocks is higher than the temperature at which the film is treated, the polymer lose the sufficient mobility for self-assembly and the morphology is kinetically trapped. As discussed above, the T_g of polymer thin films is different from the bulk state strong interactions (attractive or un attractive) with the substrate.[75–78] However, if the T_g is sufficiently above room temperature, little mobility would be expected even in the case of very thin films.

One case in the literature described mobility of a polymer after solvent annealing. Niu and Saraf described surface reconstruction of PS-*b*-PI after solvent annealing in toluene, and this reconstruction is found to occur over a period of days after solvent annealing.[79] They neglect, however, to discuss the T_g of the two block components. While the T_g of PS synthesized by anionic polymerization is known to be approximately 100°C,[80] the T_g of PI is well below room temperature. The T_g varies somewhat depending on synthesis conditions, but is -60°C for high 1,4 content[81] and well below room temperature for other PI compositions as well. The 1,4-PI content is not specified by Niu and Saraf,[79] but the surface reconstruction can be attributed to the mobility of the PI block at room temperature.

1.4.2.2 Nonselective Solvent Annealing

In general, nonselective solvents are described as good solvents for each block in a diBCP. When diBCPs thin films are swollen under nonselective solvent vapor, there are little effect of solvent annealing on the morphology of the phase diagram, as long as the effect of the dilution is factored into the χN, which is y-axis of the phase diagram. A trick to

transverse the χN axis of the phase diagram, known as the dilution approximation, was first proposed by Helfand and Tagami.[82] This method involves diluting the concentration of diBCP with a solvent. In unblended symmetric BCPs, the ODT occurs at the condition

$$\chi_{AB}N = 10.5.$$

for a diBCP with Flory-Huggins interaction parameter χ_{AB} and degree of polymerization N. In the case of solvent annealing, the Flory-Huggins interaction parameter, χ_{AB}, is described as the effective interaction parameter, χ_{eff}, between two blocks in the presence of the solvent. For neutral solvents and at high polymer concentrations, χ_{eff} may be approximated, as in the treatment of Helfand and Tagami, by

$$\chi_{eff} = \chi_{AB}\phi_p$$

where ϕ_p is the volume fraction of polymer. This effective interaction parameter reflects a dilution of the interaction between two blocks. Therefore, the dilution approximation describes the modification of the phase behavior in a nonselective solvent with an additional factor, by

$$\chi_{AB}N\phi_p = 10.5.$$

The inverse temperature component of χ_{AB} means that the ODT of a swollen BCP occurs at a lower temperature than that of a neat polymer, because the solvent segregates at the interface between the two blocks, moderating the strength of their interaction.

Noolandi and Hong studied the bulk behavior of symmetric BCPs swollen with solvents, both by using SCFT and by comparison to experimental results with PS-*b*-PI plus neutral solvent toluene, confirming the dilution approximation for concentration solutions of lamellar morphology.[83] Whitmore and Vavasour calculated a phase diagram of diBCP and nonselective solvent blends via numerical solution of the equations of SCFT of polymer blends.[84] For the y-axis of the phase diagram, the χN component has been replaced with $\chi N\phi_p$. However, they found that the phase diagram of the blends can be mapped nearly onto a common diagram, with microphase boundaries which depend primarily on the relative

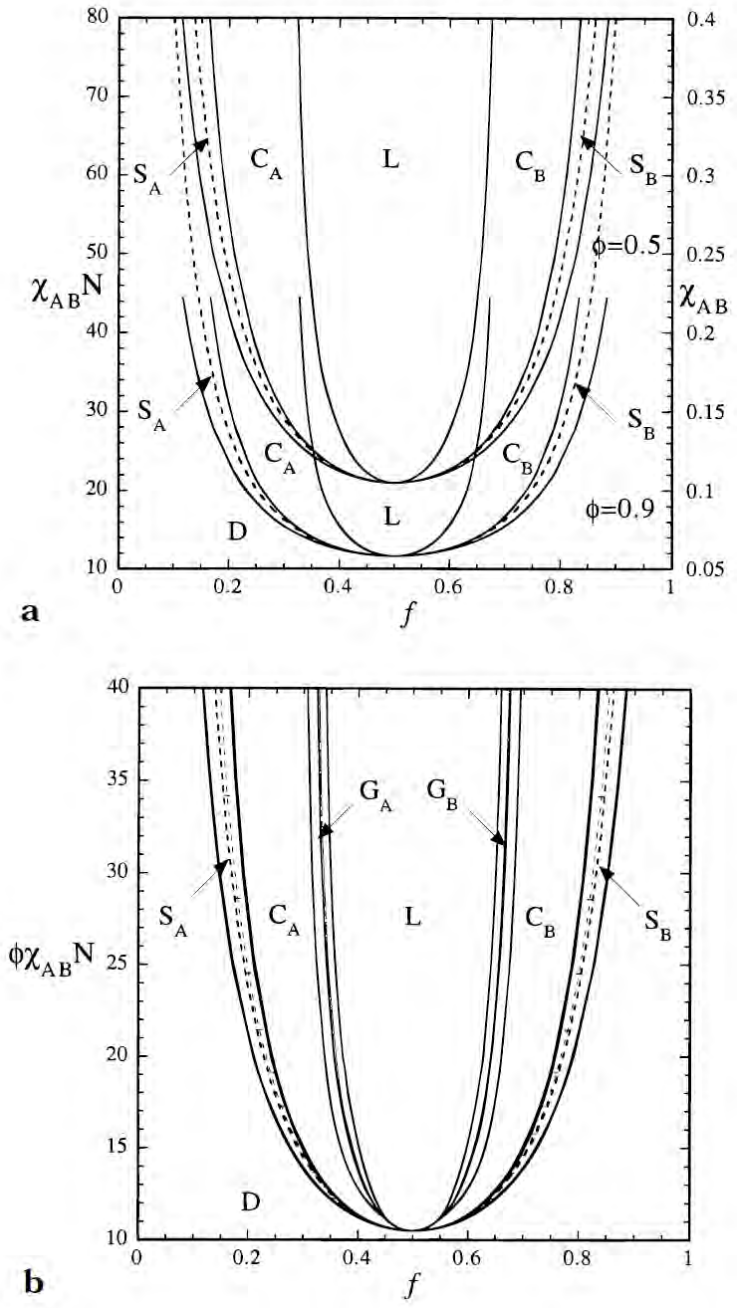

Figure 1-4. (a) Phase diagram for a diBCP swollen in a neutral good solvent with two different polymer volume fractions. (b) Rescaled phase diagram from (a) in compared with the melt when the dilution approximation holds for both order-order and order-disorder transitions Phase are labeled L (lamellae), C (cylinders), G (gyroid), S (spheres). The dashed curves correspond to the spinodal instability of the disordered state. Reprinted with permission from ref. 85, copyright 1998, American Chemical Society.

degrees of polymerization of the two blocks in the strong segregation regime. Huang and Lodge presented a theoretical study of the influence of solvent on ordered BCP solutions. Figure 1-4 shows the phase behavior of BCPs in the presence of a neutral solvent.[85]

Huang and Lodge also noted that a transition of ordered microdomains can be induced, like thermoreversible phase transitions by increasing the concentration of a solvent blended with a BCP. In a simplification of the dilution approximation, this transition can be visualized as a downward vertical shift in the phase diagram for a neat polymer upon blending with a solvent. In the case of an asymmetric BCP, this can lead to transitions between morphologies.

However, the dilution approximation is expected to fail in two cases. In the first, the use of a neutral poor solvent demixes the solution of a BCP and a neutral poor solvent with an almost pure solvent phase and a homogeneous polymer solution.[86] In the second, Frecrickson and Liebler considered that the dilution approximation requires modification in semidilute solutions as well as Olvera de la Cruz because chain swelling cannot be ignored.[87,88] Inhomogeneous solvent concentrations develop at interfaces between the blocks, and the solvent at the interfaces acts to screen unfavorable AB interactions.[87] In the weak segregation limit, the concentration of BCP at the microphase separation transition is found to scale $\phi_p \sim N^{-0.62}$ in good solvents and $\phi_p = N^{-0.5}$ in θ solvents. In the asymptotic semidilute regime in good solvents, the transition is found to scale as

$$\chi_{AB} N \phi_p^{1.59} = 10.5.$$

Lodge et al. found that ϕ_p scaling factor disagreed somewhat with experimental results of lamella-forming PS-*b*-PI swollen with neutral solvent dioctylphalate (DOP), regardless of dilution, and that the dilution approximation requires the addition of an exponent to properly describe the phase behavior.[89-91] The experimentally-measured dilution factor for the ODT scales with $\phi_p^{1.6}$ for PS-*b*-PI swollen with toluene and DOP, but with $\phi_p^{1.2}$ for poly(ethylene propylene)-*block*-poly(ethylethylene) swollen with squalane.[89] They later reported the

distribution of solvent in BCP solutions near their ODTs experimentally, by small-angle neutron scattering, and theoretically by the SCFT with a mean field model. Lamellar-forming PS-*b*-PI diblocks were applied in toluene, a nearly neutral good solvent. The factor for the ODT scales with $\phi_p^{1.6}$.[90] Lodge et al. reported the phase behavior of PS-*b*-PI diBCPs in the neutral solvent DOP experimentally with variety of concentration range and from room temperature up to 250°C. It was found that the dilution factor for ODT actually scales with ϕ_p^{α}, where α varies from 1.3 to 1.6. Thus, it was demonstrated that the dilution approximation fails for a variety of morphologies.[91]

They also studied the dilution fluctuation with OOTs between cylinder to sphere, gyroid to cylinder and lamella to gyroid, and found that the χ_{eff} of the OOT scales with $\phi_p^{1.0}$ in agreement with the dilution approximation, as predicted by theoretically.[91] Thus, the OOT decreases less quickly than the ODT, indicating that experimental phase diagrams for swollen polymers would possess a shape that does not exactly map to the neat BCP phase diagram in the weak regime. Certain ordered phases expected near the ODT are not present in the swollen state due to the differences in OOT and ODT shift with solvent. In plotting the value of the exponent α with the degree of polymerization, they observe and increase in α with increasing *N*, which is opposite to the expectation that α should decrease to 1.0 as the separation increases.

A summary of the phase behavior of a BCP swollen with a nonselective solvent follows: the dilution approximation says that interaction parameter in a polymer scales with the volume fraction of the polymer in the solvent-polymer blend. This is attributed to the alteration of the interaction of the two blocks due to selective segregation of the solvent to the interface between the blocks. Comparison of this theory with experimental results for the shift in ODT has found that an exponent must be added to adjust for non-ideal behavior, such that $\chi_{eff} = \chi_{AB} \phi_p^{\alpha}$ where α can be 1.2 to 1.6. The value of the exponent cannot be predicted,

but depends on the solvent and BCP system. This non-ideal behavior is only observed for ODT; OOT follows the dilution approximation with α equal to 1.

1.4.2.3 Selective Solvent Annealing

Solvent selectivity also plays a very strong role in the morphology formed by solvent-swollen BCPs. For each block of a polymer, solvents may be good solvents, poor solvents (near θ conditions), or non-solvents. Of course, if it is a non-solvent for both blocks, the solvent cannot swell the film at all.

When both blocks are soluble in a solvent, which is slightly selective, shift of the phase diagram occurs due to the difference of the swollen state between two blocks. As such, the phase behavior not only depends on the χ_{AB}, N and ϕ_p, but it also depends on the interaction parameter between each of the blocks and the solvent, defined as χ_{AS} and χ_{BS}.[85,92] Lai et al. suggested a clever way to evaluate the solvent selectivity. It is to measure T_g of the domains formed by the insoluble block with a differential scanning calorimetry. The solvent behaves as a plasticizer lowering the T_g. The depression of the T_g in each block indicates the degree of swelling in each block. Lodge et al. showed theoretically a strong and highly temperature-dependent preferential swelling of the PI microdomains for lamellar-forming PS-*b*-PI swollen in PI selective cyclohexane.[93]

This selective partitioning can be expected to affect the volume fraction of the BCP, f. Huang and Lodge studied the effect of solvent selectivity on phase morphology by using the SCFT.[85] A two-dimensional phase diagram of a diBCP in the presence of a selective solvent at $\phi_p = 0.5$ is shown in Figure 1-5. The interaction parameters χ_{AS} and χ_{BS} are set equal to 0.6 and 0.4, respectively, indicating a slightly affinity for the B block. Therefore, the phase diagram of the BCP swollen in a selective solvent shifts to the right. The shape of the phase diagram is also asymmetric, such that the location of the transitions does not map on top of a phase diagram of a neat BCP.

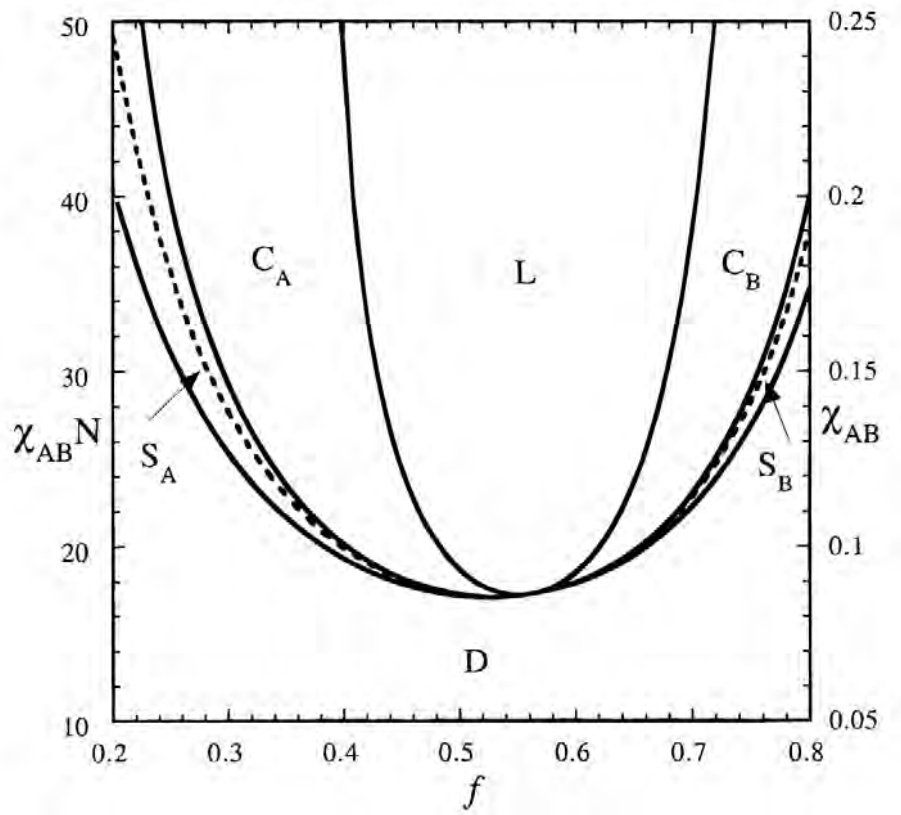

Figure 1-5. Phase diagram for a diBCP swollen in a selective solvent. This diagram indicate the shift of the critical point and change to asymmetric shape. Reprinted with permission from ref. 85, copyright 1998, American Chemical Society.

Huang and Lodge also reported a change in the degree of stabilization of BCP morphology.[85] In their SCFT, they set χ_{BS} equal to a constant value and varied χ_{AS}. There exists a crossover value of χ^*_{AS} determined from the intersection of the two dimentional spinodal curves as a function of $\chi_{AB}N$, χ_{AS}, and ϕ_p. When the solvent is only slightly selective, $\chi_{AS} < \chi^*_{AS}$, decreasing ϕ_p stabilizes the homogeneous solution. In contrast, when the solvent is more strongly selective, $\chi_{AS} > \chi^*_{AS}$, decreasing ϕ_p enlarges the regions of stable ordered microstructures and/or macrophase separation.

They further indicated the morphology tunability, which is to form multiple structures by high solvent selectivity.[85] For a symmetric diBCP swollen in a selective solvent, which is good for B but poor for A, a morphology is expected that with increasing solvent volume in

the B microdomain, the morphology changes from lamellae (L) to cylinders of block A (C_A), to spheres (S_A), and finally to disordered state, corresponding to a shift in *f*. This may be envisioned as a horizontal walk across the phase diagram. Also, for an asymmetric diBCP, forming cylinders of block B (C_B) in the melt, a sequence of transitions as in melts is expected.

This morphology-shifting behavior has been demonstrated experimentally in many cases.[93–99] Hanley and Lodge reported swelling of symmetric PS-*b*-PI in di-*n*-butyl phthalate (DBP), which is styrene-selective solvent.[94] DBP is good solvent for PS, but is near a θ solvent for PI at approximately 90°C, and so it is selective below that temperature but negligibly selective above 100 °C. Varying both the selective solvent concentration and the temperature, they observed shifts that can be visualized a diagonal shift of position in the phase diagram, where the x-axis volume component is caused by the solvent selectivity and the y-axis shift is due to the inverse-temperature component of χ. For example, for $\phi_p = 0.9$, they observe shifts from lamellae (75 °C), perforated lamellae (100 °C, metastable state), gyroid (150 °C) and cylinders (180 °C). They suggest that addition of a selective solvent amounts to a horizontal trajectory across the phase diagram. Also, when the solvent selectivity depends on temperature, as it does for the PS-*b*-PI/DBP solution, increasing temperature corresponds to a diagonal trajectory.

Hanely et al. indicated that asymmetric PS-*b*-PI swollen with DBP forms inverse versions of their morphology: L → G_{inv} (inverted gyroid)→ C_{inv} (inverted hexagonal-packed cylinders)→ S_{inv} (inverted body-centered-cubic spheres), moving in the opposite direction as the thermoreversible morphology shift G → C → D shift.[96] Addition of isoprene-selective tetradecane allows access to the G → C → D shift. Lai et al. showed as many as five ordered phases for a single BCP by swelling PS-*b*-PI with tetradecane.[93]

1.4.2.4 Periodicity of Microdomain Structure in Swollen BCP Film

Even when bulk mixture of BCP and solvent does not change phase behavior from the neat block copolymer, swelling with a solvent also change the equilibrium spacing of the microdomain structures of BCPs. The change of the periodicity depends on solvent selectivity. Swelling with a solvent decreases the periodicity of the BCP. The value of the decrease varies with the solvent selectivity for the different blocks.

Hashimoto et al. demonstrated this behavior experimentally with PS-*b*-PI swollen with nonselective solvent, DOP.[100] They found that the periodicity D scales as

$$D/b \sim N^{2/3}[\phi_p/T]^{1/3}$$

where b is the statistical Kuhn length.

Shibayama et al. also observed a critical value of ϕ_p/T with different swelling behavior of PS-*b*-PI swollen with neutral solvents toluene and DOP. This value, approximately ϕ_p = 70, separates two regimes of spacing.[101,102] In the low-concentration regime (less than 70 wt% polymer), D increases with increasing ϕ_p. In the high-concentration regime (greater than 70 wt% polymer), D tends to decreases with increasing ϕ_p, consistent with earlier results reported by Skoulios et al.[103–105] and Gallot et al.[106] They also reported that D in low-concentration regime is thermodynamically controlled, while D in the high-concentration regime is kinetically controlled but not thermodynamically controlled. This difference points out that the solvent lowers the T_g of the blocks to below room temperature, give polymer mobility below room temperature at high solvent concentration. Thus sufficient mobility for self-assembly is observed at higher swelling.

Whitmore and Noolandi modeled the behavior of lamella-forming diBCPs swollen in a neutral good solvent by using SCFT.[107] They found that the dependence of D on χ_{AB} for various N and ϕ_p scales as

$$D/b \propto [\chi_{AB}]^p N^q [\phi_p]^r$$

where the exponents p, q, and r depends on the segregation strength. They also found that the strongest dependence occurs in the weak segregation limit, with

$p \approx 1/3$, $q \approx 0.8$, and $r \approx 0.4$.

By contrast, that occurs in the strong segregation limit, with

$p \approx 0.2$, $q \approx 2/3$, $r \approx 0.22$.

Between weak-field and strong field extremes, the exponent r smoothly evolves between $r = 0.22$ in the weak segregation limit (up to $\chi_{AB}N\phi_p \leq 15$) and $r = 0.4$ in the strong segregation limit.

This behavior of different scaling of D with strong and weak segregation limits has been observed experimentally with solvent-swollen melts.[92,108] Whitmore and Noolandi suggested that as ϕ_p approaches 1 – that is, neat polymer without solvent – the equation collapses to an expression very similar to that by Helfand and Wasserman for unblended block copolymer self-assembly.[109]

$$D/b \approx \gamma^{2/3}N^{9/14}$$

where γ is the interfacial tension, and $\gamma \approx [\chi_{AB}]^{0.5}$

$$D/b \approx [\chi_{AB}]^{0.14}N^{0.64}$$

Whitmore and Noolandi's results are in agreement with those by Shibayama and Hashimoto, as long as the polymers are self-assembling in the thermodynamically-directed ranges (that is, sufficient swelling for mobility at the experimental temperature). Lodge et al. also observed agreement of experimental results of PS-*b*-PI swollen with DOP, in which D scales with $\phi_p^{0.33}$ independent of morphology.[91]

Swelling with a nonselective solvent causes modification of D as well. Banaszak and Whitmore extended earlier self-consistent field theory studies to selective solvent swelling of symmetric block copolymers, assuming $\chi_{AB} = \chi_{SB}$ and $\chi_{SA} = 0$(non-interacting). They found the same basic relationships as for swelling with selective solvent,

$$D/b \propto [\chi_{AB}]^p N^q [\phi_p]^r$$

where in strong segregation limit $p \approx 0.2$, $q \approx 0.7$, and $r \approx 0.2$ (the almost identical to values for a nonselective solvent), and in weak segregation limit, $p \approx 0.5$, $q \approx 0.9$, and $r \approx 0.5$.

The weak field phase behavior was confirmed experimentally $-D$ was found to scale with $\phi_p^{0.5}$ in PS-*b*-PI swollen with di-*n*-butyl phthalate (DPB), slightly selective for PS.

Lai et al .experimentally studied the effect of solvent selectivity on the r exponent of $D \sim \phi^r$, and found that the value decreases with increasing solvent selectivity, even into negative values. Negative value of r indicates that the spacing increases with selective solvent blending, rather than decreasing as with a nonselective solvent. They conclude that r also varies with the block composition, f, and the mesophase formed upon swelling, and that it is not possible to make simple sum of the contributions from these three related variables.

1.5 Directed Self-assembly

As described in section 1.1, microdomain structures of BCPs thin films are applied as a etch mask for lithography. More than a decade ago, Mansky et al. first demonstrated that periodic microdomain structure of diBCP thin film can be put to apply as a etch mask by using sphere- and cylinder-forming poly(styrene-*b*-butadiene) diBCP.[110,111] This method uses BCPs as photoresist patterns employed in traditional lithographic applications. Park et al. demonstrated that periodic pattern of holes and dots can be fabricated on a silicon nitride coated silicon wafer by applying sphere- and cylinder-forming poly(styrene-*b*-butadiene) thin films as etch mask.[112,113]

Figure 1-6 schematically depicts typical process of their approach. As described in Section 1.3, BCP thin film is prepared on the substrate by spin-coating with the solution of the BCP. The thin film is annealed to self-assemble to form microdomain structure. Then, one of the domains in the thin film is removed by etch process, such as reactive ion etch, wet process, and so on. The porous film can be used as a mask to transfer pattern to the

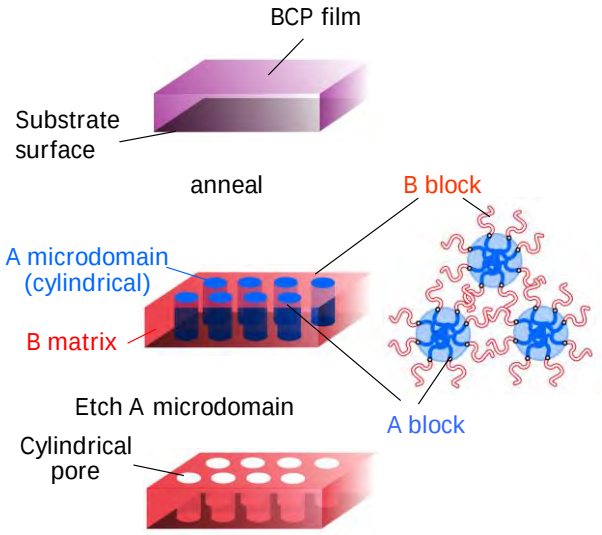

Figure 1-6. Schematic illustration of block copolymer lithography using perpendicularly oriented microdomain of BCP.

substrate. This process opens possibilities for fabricating nano structures that is difficult for current lithography to achieve. Black et al. reviewed this topic in detail.[114]

One of the key points to apply BCP as etch mask is to have etch contrast between two blocks. A vast majority of research has been devoted to PS-*b*-PMMA as a model material, because of its PMMA content, may be used as a lithographic photoresist.[20,22,115–116] Actually, PS have higher etch resistivity against oxygen plasma or UV irradiation than PMMA. Also, there are several BCPs with higher etch contrast than PS-*b*-PMMA.[117–123] For example, BCPs with siloxane contents have attracted much attention for much higher etch contrast against oxygen plasma than organic blocks due to the resistivity of siloxane contents, such as polydimethylsiloxane containing BCP,[117–120] polyhedral oligomeric silsesquioxane (POSS) containing BCP,[121-123] and so on.

Another key point is to control microdomain structures and their orientation. There are two types of etch mask, which use perpendicularly oriented microdomains and parallel oriented microdomains. When line and space pattern is fabricated by using BCPs, perpendicularly oriented lamellae or parallel oriented cylinders on the substrate is applied as a

mask. Also, when hole or dot pattern is fabricated by using BCPs, perpendicularly oriented cylinders or spheres on the substrate is used as a mask. As described in Section 1.3, the perpendicularly oriented microdomains are influenced by both the film thickness and the interfacial interactions at the air/polymer and polymer/substrate interfaces. On the other hand, spheres and parallel oriented cylinders tend to form step unless the thickness of BCPs film matches the repeat distance of the domain spacing. Therefore, parallel oriented microdomains applied as etch mask requires the film thickness to form homogeneous layer composed of single domain.

To attain perpendicularly oriented microdomains, it is necessary to form neutral condition to two block chains on both air and substrate surface. To form neutral condition on substrate surface, random copolymers tuned the composition are typically grafted on the substrate, as described in Section 1.3.[60,124–131] On the other hand, it is generally more difficult to form neutral condition on air surface than to form it on substrate surface. Especially, the parameter to control the interfacial interaction at the air/polymer is limited in the case of thermal annealing. PS-*b*-PMMA is one of the very few combinations of polymers, which can form neutral condition at the air/polymer with thermal annealing process. PS and PMMA block exhibit almost identical interfacial interaction against air or vacuum at the temperature applicable for annealing process.[110] As described above, PS-*b*-PMMA also has etch contrast against oxygen plasma. These characteristics make PS-*b*-PMMA one of the most appropriate materials for etch mask.

Alternative method to form neutral condition at the air/polymer is to anneal under solvent vapor. Several studies reported that neutral conditions can be achieved by choosing appropriate solvent and controlling solvent evaporation rate.[132–135]

As described above, the microdomain structures of BCP thin film thoroughly have possibilities to apply to lithography technique. However, some applications of BCP thin films are tolerant of disorder and defects, while the applications to semiconductor devices or

magnetic storage devices require the abilities to precisely control the placement and remove the defects of microdomain structures on substrates. Numerous routes to control lateral order have been studied in depth experimentally by utilizing external fields such as share flow,[136,137] electrical field,[138,139] and lithographically prepatterned templates. These approaches are usually called directed self-assembly (DSA). In particular, a route to utilize lithographically prepatterned templates promise to achieve desired patterns, combining top-down (lithography) and bottom-up (self-assembly) techniques. Typically, either topographic relief structure[20,22,115,140–147] or chemically patterned surface regions[28–31,116,148–152,] is used as lithographically prepatterned templates to control the placement. In this section, I review several general DSA methods.

1.5.1 Graphoepitaxy: Topographic Guiding Patterns

Topographic relief structures can facilitate the crystal growth of microdomain structures of BCP thin films.[20,22,115,140–147] Such topographic guiding patterns are commonly fashioned by plasma etching of solid substrates using a patterned photoresist layer as an etch mask or by directly utilizing the photoresist image in those instances where it is not soluble in the BCP's casting solvent. Figure 1-7 shows the typical graphoepitaxy image with trench patterns. Segalman et al. first reported that this graphoepitaxial strategy is applied to generate arrays of spherical domains of PS-*b*-P2VP over large areas and with a high degree of perfection.[141] They found that there is polycrystalline structure in PS-*b*-P2VP thin films on a flat substrate after thermal annealing, but the thin film deposited on the topographic relief structure shows the formation of a single-crystal grain with over large areas.

Cheng et al. systematically investigated the ordering of spherical microdomain structures confined in lithographically defined grooves by using a poly(styrene-*b*-ferrocenyldimethylsilane).[142–144] Using grooves with uniform and modulated

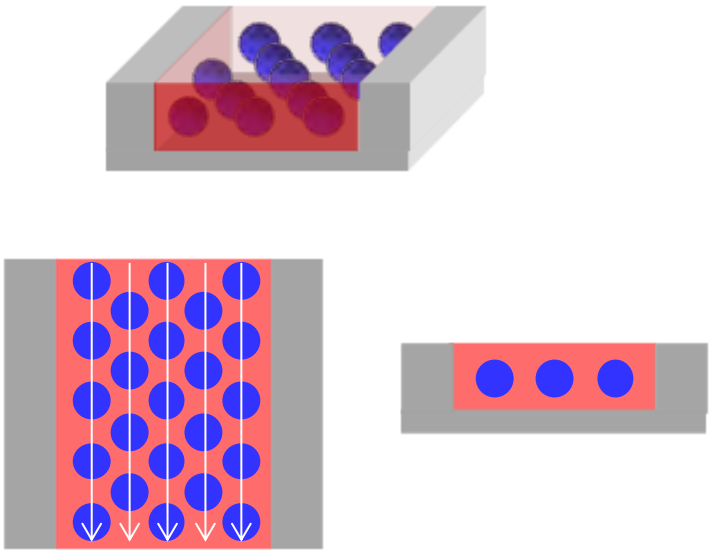

Figure 1-7. Schematic illustration of graphoepitaxy using sphere-forming BCP with trench pattern. Trench pattern guide orientation of sphere microdomain of BCP.

widths, they were able to understand how elastic strain in the array of domains governs their local arrangement within the grooves.

Recently Bita et al. reported the use of sparse arrays of posts, which are topographic relief structures, to graphoepitaxially induce long-range order on spherical microdomains of poly(styrene-*block*-dimethyl siloxane).[140] In their work, the BCP film was deposited on a topographic relief substrate with a regular array of so discrete posts. The posts interact both locally and globally with the spherical domains, providing periodic constraints that drive the formation of a two – dimensional periodic nanostructure array with precisely determined orientation and long-range order. Figure 1-8 shows a schematic presentation of this technique and SEM images of ordered block copolymer domains that result from its application. With this sparse template approach, the commensurability between the period of microdomain structures of BCPs and the template period governs the orientation and

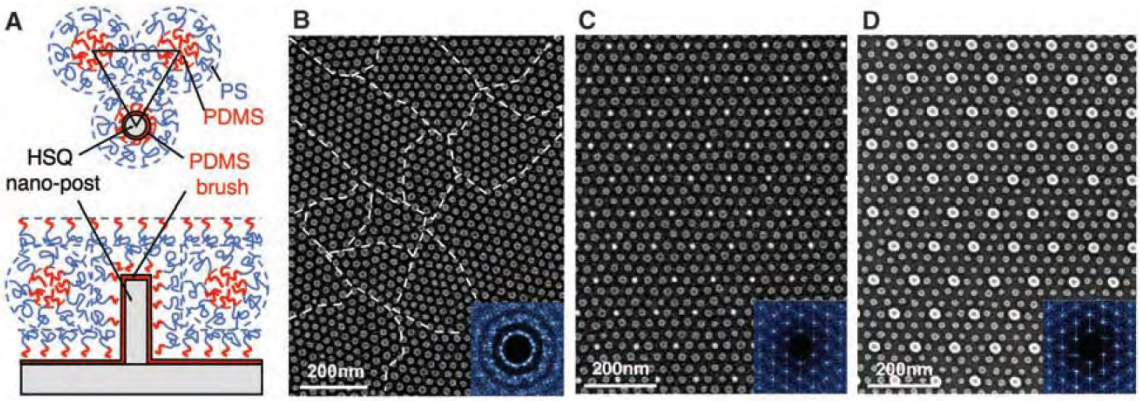

Figure 1-8. Schematic illustration and SEM images of graphoepitaxy with sparse post array. (A) Top-down and Cross-sectional image of graphoepitaxy of polystyrene-*b*-polydimethylsiloxane with sparse post array. Post array was composed of hydrogen silsesquioxane resist. Posts and substrate were grafted by polydimethylsiloxane to tune the surface energy. (B) SEM image of microdomain structure of polystyrene-*b*-polydimethyl siloxane thin film on the substrate without the template. There were several grains and the dashed line represents the boundary between deferent grains. (C), (D) SEM images of the micorodomain in thin films with the different post arrays. In both cases, the post array succeeded the graphoepitaxy. Reprinted with permission from ref. 140, copyright 2008, American Association for the Advancement of Science.

periodicity of the resulting array of spherical domains and is accurately described by a free energy model.

These results show ordering spherical microdomain structures of BCPs by DSA with graphoepitaxy. Several works have reported graphoepitaxy with cylindrical or lamellar microdomain structures.[20,145–147]

The interaction between block chains of diBCPs and walls is important to control ordering and orientation of microdomain structures which are especially oriented cylinders or

perpendicularly oriented lamellae. When the surface on the wall is preferential for one block of diBCP, the cylinders or lamellae are aligned parallel to the surface on the wall. On the other hand, when the surface on the wall is neutral condition to both two blocks, the cylinders or lamellae orient perpendicularly to the wall surface.[20,145,146]

1.5.2 Chemical Hetero Epitaxy: Chemical Guiding Patterns

Chemical hetero epitaxy refers to the use of chemically patterned template, which is composed of different interfacial energy surface (chemical contrast) against two blocks of diBCP on a substrate to order microdomain structures of diBCP thin film.[30,116,148–152] Figure 1-9 shows the concept of the chemical hetero epitaxy with cylinder-forming diBCP for an example. The templates are usually prepared by using conventional lithography technique, such as photolithography, electron-beam lithography, and so on. In this case, the template forms circular regions with hexagonal closed pack arrangement. The surface of these circular regions are designed to have higher affinity to A block, which form cylindrical domain, while surrounding matrix are prepared to prefer B block. Typically, the length scale of the template must be set close to that of the periodicity of the microdomain structure. When diBCP is deposited on the template and self-assembles to form micordomain structure, cylinders are registered on the circular regions. The registration is facilitated by minimizing the free energy by placing the cylinders on the circular regions and matrix on the surrounding area.

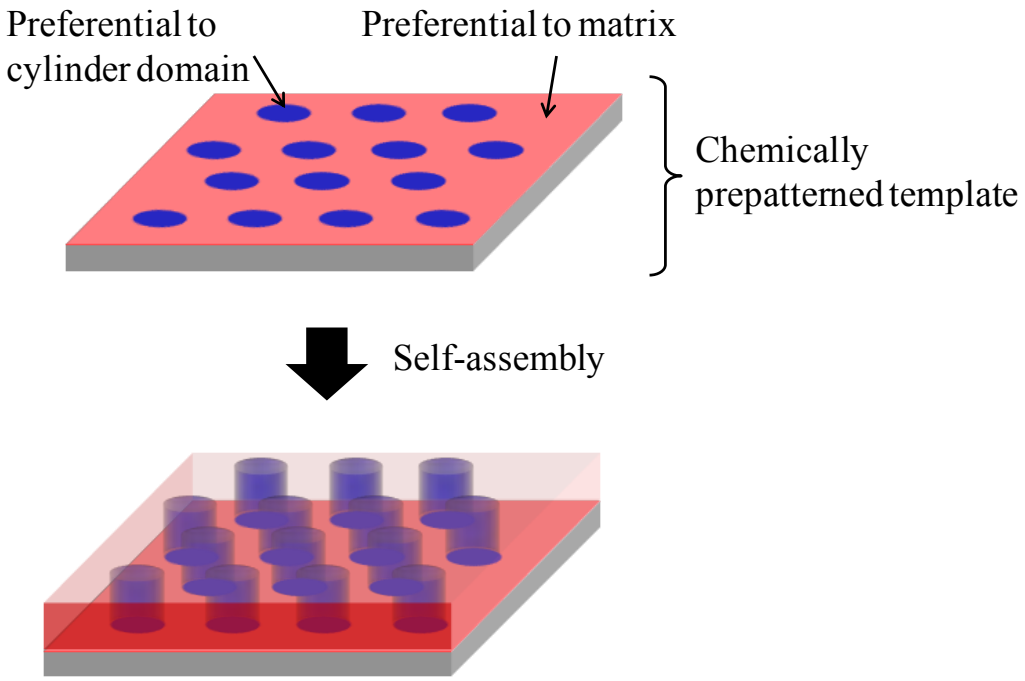

Figure 1-9. Schematic illustration of chemical hetero epitaxy using cylinder-forming BCP with chemically prepatterned template. The template are composed of two kind of surfaces, which are preferential to cylinder domain or matrix domain. Self-assembly with the template can register the cylindrical micorodomain structure and results in improving the long-range order.

Rockford et al. first reported a relationship between controlled nano-scale surface interactions and subsequent macromolecular ordering.[116] They used a surface striped with oxide (silicon oxide) and metal (gold), where the stripe width is a lateral period of tens of nanometers and height amplitude of several nanometers were prepared from single-crystal silicon wafers intentionally miscut at an angle from the crystal orientation. The lamellar microdomain structure of PS-*b*-PMMA is oriented perpendicular to the substrate surface and directed by the underlying strips on the heterogeneous surface.

Nealey et al. demonstrated the DSA of lamella- and cylinder forming PS-*b*-PMMA by chemically patterned template.[148–151] Figure 1-10 shows a schematic of their process, along with experimental images that depict alignment of the cylindrical domain of PS-*b*-PMMA,

Chemically patterned templates are formed on the substrate by preparing a thin film of polymer brush on the substrate and patterning the polymer brush with lithographic technique, such as extreme ultraviolet interferometric lithography or electron-beam lithography. The template has circular regions with oxidized silicon or oxidized PS-brush surface. The former have lower surface energy to PMMA, while PS-brush surface has high affinity to PS. Defect-free long-range order of perpendicularly oriented cylindrical microdomains over the template areas was achieved by using this approach when the periodicity of the template patterns matches that of the cylindrical microdomains of the PS-*b*-PMMA. Recently, reports in which chemical heteroepitaxy was combined with nanofabrication techniques have shown much more complex patterns such as jogs, bends, junctions, chevrons, dashes, rectangular features and even three-dimensional structures.[28-31]

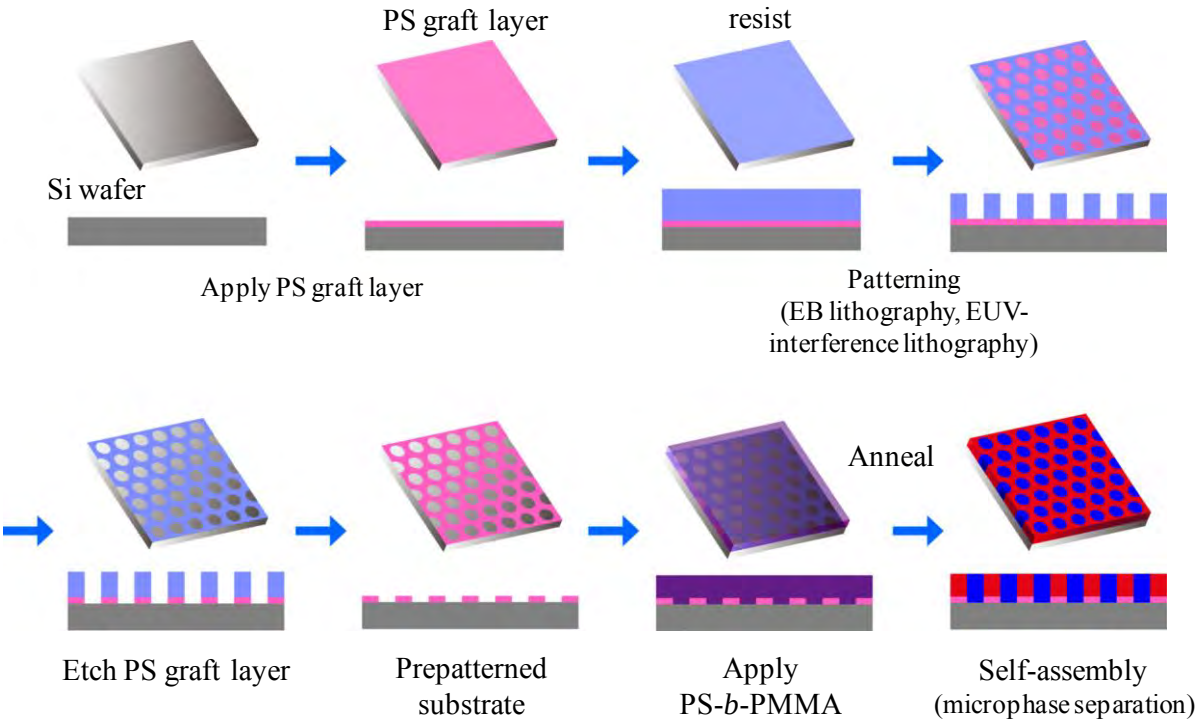

Figure 1-9. Schematic illustration of the directed self-assembly process with a chemically prepataterned template by using cylinder-forming PS-*b*-PMMA.

Several studies reported the rectification and feature density multiplication of the sparse template by using DSA of BCPs. The rectification of the template pattern have been reported to be effective to reduce line-edge roughness in the resist pattern[153,154] and correct variation in width of line and space pattern.[155] Furthermore, DSA is effective to reduce defects because of good short-range order. When this effect is applied to interpolate sparse template patterns in much positive way, namely this effect is called as feature density multiplication. The basic concept is depicted in Figure 1-11. Ruiz et al. demonstrated DSA of perpendicularly oriented cylinders of PS-*b*-PMMA with 4× density multiplication.[151] Cheng et al. also reported DSA of perpendicularly oriented lamellae of PS-*b*-PMMA with density multiplication. They applied double, triple, and quadruple sparse template patterns. They also demonstrated the rectification of poorly defined template patterns by the BCPs, illustrating the beneficial rectifying effect of BCP self-assembly. This approach offers the potential to save significant time and effort when creating regular patterns over large areas.

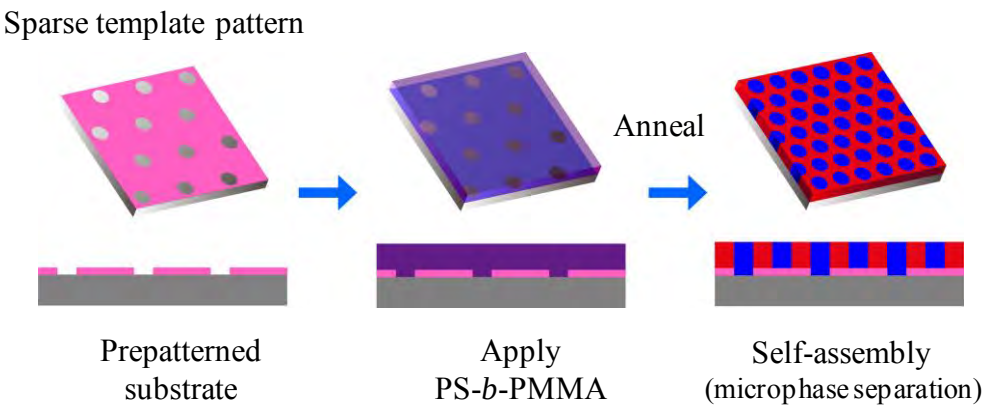

Figure 1-9. Schematic illustration of the directed self-assembly process with the density multiplication by using cylinder-forming PS-*b*-PMMA.

In this thesis, I apply DSA of BCP with density multiplication as the next generation lithography technique and control the placement and morphology of micrdomain structures of diBCP thin film to form ultra-high density pattern. I employ chemical hetero epitaxy as DSA of BCPs and clarify the effects of the interfacial interaction between the template surface and polymer chain, the conformational energy of polymer chain, and the mobility of polymer on the pattern obtained by DSA in detail.

1.6 Outlook of This Thesis

The objective of this thesis is to form ultra high density pattern by applying DSA of BCP, which is chemical hetero epitaxy. In this process, it is quite important to control the morphology and placement of micrdomain structures of diBCP thin film because the high density pattern requires the sufficient uniformity and placement accuracy for lithographic application, or patterned media. Therefore, I clarified the effect of the interfacial energy between polymer chain and the substrate surface, the conformational energy of polymer chain, and the long-range order of microdmain structure on the pattern fidelity. In Chapters 2 and 3, I focus on the directed self-assembly with feature density multiplication by using perpendicularly oriented cylindrical PMMA domains of PS-*b*-PMMA. I demonstrated 4× and 9× feature density multiplication with high fidelity and revealed that the key factor to rectify and interpolate the template pattern is the control of the surface energy on the template and the conformational energy of the polymer chain. In Chapter 4, I applied strongly segregating polyhedral oligomeric silsesquioxane (POSS) containing BCP to form higher density pattern than that of PS-*b*-PMMA. I demonstrated the directed self-assembly of POSS containing BCP with density multiplication by optimized solvent annealing, thereby achieving the dot density of ca. 4 tera dots/inch^2.

In Chapter 2, I found that directed self-assembly combining top-down (EB lithography) and bottom-up (self-assembly) technologies can overcome the limitation of current lithography technique by applying cylinder-forming PS-*b*-PMMA to chemical hetero epitaxy. Actually, cylinder-forming PS-*b*-PMMA self-assembled to form perpendicularly oriented cylinders with a well-align and long-range order over arbitrarily large areas on the chemically patterned templates prepared by EB lithography. I also found that the short-range order of microdomain structure can rectify defects on the templates and interpolate the points between sparse template patterns. Furthermore, I demonstrated the hexagonally closed packed

pattern with the lattice spacing of 24 nm, corresponding to ca. 1 tera dot/ inch^2, by using the pattern interpolation positively, which are described as feature density multiplication.

In Chapter 3, I demonstrated 9× feature density multiplication by PS-*b*-PMMA with the lattice spacing of 24 nm as well as Chapter 2. I found that the film thickness is limited to a narrow range to attain perpendicularly oriented cylinder of PS-*b*-PMMA on the interpolation points and the tolerance of the lattice mismatch between the template pattern and domain spacing for 9× feature density multiplication is smaller than that for 4× feature density multiplication. Furthermore, I revealed that the critical dimension formed by the block copolymer domains is independent of that defined by the EB pre-patterned features.

In Chapter 4, I demonstrated the hexagonally closed packed dot pattern with the lattice spacing of 12 nm, corresponding to ca. 4 tera dot/inch^2, by applying POSS containing BCP to fabricate ultra high density pattern that is difficult for current lithography to achieve. Solvent annealing was applied to form microdomain structure of POSS containing BCP. I found that the microdmain structure with long-range order requires sufficient mobility of polymer chain under solvent annealing and control of the swollen state of the BCP thin film due to dependence of the lattice spacing of the micorodomain structure on the degree of swelling. I also showed that the microdomain structures formed by solvent annealing the BCP on the chemically patterned template could tolerate several percent of the lattice mismatch between the domain spacing of the BCP and that of the template. Finally, I expect these results to support the potential application of the technique to form 10 nm scale features.

1.7 References

1. International Technology Roadmap for Semiconductors, 2009 Edition. http://www.itrs.net (accessed Dec. 2011).
2. Galatsis, K.; Wang, K. L.; Ozkan, M.; Ozkan, C. S.; Huang, Y.; Chang, J. P.; Monbouquette, H. G.; Chen, Y.; Nealey, P. F.; Botros, Y. *Adv. Mater.* **2010**, *22*, 769.
3. Kim, H.-C.; Park, S.-M.; Hinsberg, W. D.; *Chem. Rev.* **2010**, *110*, 146.
4. Segalman, R. A. *Mater. Sci. Eng., R* **2005**, *48*, 191.
5. Stoykovich, M. P.; Nealey, P. F. *Mater. Today* **2006**, *9*, 20.
6. Grzelczak, M.; Vermant, J.; Furst, E. M; Liz-Marzán, L. M. *ACS Nano* **2010**, *4*, 3591.
7. Westerlund, F.; Bjørnholm, T. *Curr. Op. Colloid Interface Sci.* **2009**, *14*, 126.
8. Pasquino, R.; Snijkers, F.; Grizzuti, N.; Vermant, J. *Langmuir* **2010**, *26*, 3016.
9. Sun, Z.; Kim, H. K. *Appl. Phys. Lett.* **2002**, 81. 3458.
10. Kustandi, T. S.; Loh, W. W.; Gao, H.; Low, H. Y. *ACS Nano* **2010**, *4*, 2561.
11. Maria Chong, A. S.; Tan, L. K.; Deng, J.; Gao, H. *Adv. Funct. Mater.* **2007**, 17, 1629.
12. Oshima, H.; Kikuchi, H.; Nakao, H.; Itoh, K.; Kamimura, T.; Morikawa, T.; Umada, T.; Tamura, H.; Nishio, K.; Masuda, H. *Appl. Phys. Lett.* **2007**, *91*, 22508.
13. Rothemund, P. W. K. *Nature* **2006**, *440*, 297.
14. Park, S. Y.; Lytton-Jean, A. K. R.; Lee, B.; Weigand, S.; Schatz, G. C.; Mirkin, C. A. *Nature* **2008**, *451*, 553.
15. Pal, S.; Deng, Z.; Ding, B.; Yan, H. *Angew. Chem. Int. Ed.* **2010**, *49*, 2700.
16. Resnick, D.; Brooks, C.; Schmid, G.; Miller, M. SPIE DOI: 10.1117/2.1200902.1514.
17. Service, R. F. *Science* **2006**, *314*, 1868.
18. Cheng, J. Y.; Ross, C. A.; Chan, V. Z.-H.; Thomas, E. L.; Lammertink, R. G. H.; Vancso, G. J. *Adv. Mater.* **2001**, *13*, 1174.
19. Naito, K.; Hieda, H.; Sakurai, M.; Kamata, Y.; Asakawa, K. *IEEE Trans. Magn.* **2002**, *38*, 1949.

20. Xiao, S. G.; Yang, X.M.; Edwards, E. W; La, Y.-H.; Nealey, P. F, *Nanotechnology* **2005**, *16*, S324.

21. Guarini, K. W.; Black, C.T.; Zhang, Y.; Babich, I.V.; Sikorski, E.M.; Gignac, L.M. *IEEE Tech. Dig. IEDM* **2003**, 541.

22. Black, C. T.; Guarini, K. W.; Milkove, K. R.; Baker, S. M.; Russell, T. P.; Tuominen, M. T. *Appl. Phys. Lett.* **2001**, *79*, 409.

23. Black, C. T.; Guarini, K. W.; Ying Z.; Hyungjun K.; Benedict, J.; Sikorski, E.; Babich, I. V.; Milkove, K. R. *IEEE Electron Device Lett.* **2004**, *25*, 622.

24. Gido, S. P.; Thomas, E. L. *Macromolecules* **1994**, *27*, 6137.

25. Burgaz, E.; Gido, S. P. *Macromolecules* **2000**, *33*, 8739.

26. Duque, D.; Katsov, K.; Schick, M. *J. Chem. Phys.* **2002**, *117*, 10315.

27. Stoykovich, M. P.; Kang, H.; Daoulas, K. C.; Liu, G.; Liu. C.-C.; Pablo, J. J.; Muller, M.; Nealey, P. F. *ACS Nano* **2007**, *1*, 168.

28. Kang, H.; Crag, G. S. W.; Nealey, P. F. *J. Vac. Sci. Technol., B* **2008**, *26*, 2495.

29. Liu, G.; Thomas, C. S.; Craig, G. S. W.; Nealey, P. F. *Adv. Funct. Mater.* **2010**, *20*, 1251.

30. Ruiz, R.; Dobisz, E.; Albrecht, T. R. *ACS Nano* **2011**, *5*, 79.

31. Shin, K.; Leach, K. A.; Goldbach, J. T.; Kim, D. H.; Jho, J. Y.; Tuominen, M.; Hawker, C. J.; Russell, T. P. *Nano Lett.* **2002**, *2*, 933.

32. Hamley, I. W. *The Physics of Block Copolymers*; Oxford University Press: Oxford, 1998.

33. Khandpur, A. K.; Forster, S.; Bates, F. S.; Hamely, I. W.; Ryan, A. J.; Bras, W.; Almdal, K.; Mortensen, K. *Macromolecules* **1995**, *28*, 8796.

34. Bate, F. S.; Fredrickson, G. H. *Annu. Rev. Phys. Chem.* **1990**, *41*, 525.

35. Hashimoto, T., In *Thermoplastic Elastmers*; Legge, N. R., Holden, G., Schroeder, H. E., Eds.; Hanser: Vienna, 1996.

36. Matsen, M. W.; Schick, M. *Phys. Rev. Lett.* **1994**, *72*, 2660.

37. Leibler, L. *Macromolecules* **1980**, *13*, 1602.

38. Smenov, A. N. *Macromolecules* **1986**, *25*, 4967.

39. Ohta, T.; Kawasaki, K. *Macromolecules* **1986**, *19*, 2621.

40. Helfand, E. *Macromolecules* **1975**, *8*, 552.

41. Hashimoto, T.; Shibayama, M.; Kawai, H. *Macromolecules* **1980**, *13*, 1237.

42. Fried, J. *Polymer Science and Technology*, 2nd ed.; Prentice Hall: Upper Saddle River, NJ, 2003.

43. Flory, P. J. *Principles of Polymer Chemistry*; Cornell University Press: Ithaca, NY, 1953.

44. Matsen, M. W.; Bates, F. S. *Macromolecules* **1996**, *29*, 1091.

45. Khandpur, A. K.; Forster, S.; Bates, F. S.; Hamley, I. W.; Ryan, A. J.; Bras, W.; Almdal, K.; Mortense, K. *Macromolecules* **1995**, *28*, 8796.

46. Takenaka, M.; Wakada, T.; Akasaka, S.; Nishitsuji, S.; Saijo, K.; Shimizu, H.; Kim, M. I.; Hasegawa, H. *Macromolecules* **2007**, *40*, 4399.

47. Sivaniah, E.; Matsubara, S.; Zhao, Y.; Hashimoto, T.; Fukunaga, K.; Kramer, E. J.; Mates, T. E. *Macromolecules* **2008**, *41*, 2584.

48. Matsushita, E.; Mori, K.; Saguchi, R.; Nakao, Y.; Noda, I.; Nagasawa, M. *Macromolecules* **1990**, *23*, 4313.

49. Coulon, G.; Russell, T. P.; Deline, V. R.; Green, P. F. Macromolecules 1989, 22, 2581.

50. Rebei, A.; De Pablo,J. *Phys Rev. E* 2001, *63*, 041802.

51. Melenkeviz, J.; Muthukumar, M. *Macromolecules* **1991**, *24*, 4199.

52. Whitemore, M. D.; Noolandi, J. *J. Chem. Phys.* **1990**, *93*, 2946.

53. Anastasiadis, S. H.; Russell, T. P.; Satija, S. K.; Majkrzak, C. F. *Phys. Rev. Lett.* **1989**, *62*, 1852.

54. Coulon, G.; Russell, T. P.; Deline, V. R.; Green, P. F. *Macromolecules* **1989**, *22*, 2581.

55. Turner, M. S. *Phys. Rev. Lett.* **1992**, *69*, 1788.

56. Walton, D. G.; Kellogg, G. J.; Mayes, A. M.; Lambooy, P.; Russell, T. P. Macromolecules **1994**, *27*, 6225.

57. Lambooy, P.; Russell, T. P.; Kellogg, G. J.; Mayes, A. M.; Gallagher, P. D.; Satija, S. K. *Phys. Rev. Lett.* **1994**, *72*, 2899.

58. Kellogg, G. J.; Walton, D. G.; Mayes, A. M.; Lambooy, P.; Russell, T. P.; Gallagher, P. D.; Satija, S. K. *Phys. Rev. Lett.* **1996**, *76*, 2503.

59. Konrad, M.; Knoll, A.; Krausch, G.; Magerle, R. *Macromolecules* **2000**, *33*, 5518.

60. Xu, T.; Hawker, C. J.; Russell, T. P. *Macromolecules* **2005**, *38*, 2802.

61. Pickett, G. T.; Balazs, A. C. *Macromolecules* **1997**, *30*, 3097.

62. Sommer, J.-U.; Hoffmann, A.; Blumen, A. *J. Chem. Phys.* **1999**, *111*, 3728.

63. Harrison, C.; Chaikin, P. M.; Huse, D. a.; Register, R. A.; Adamson, D. H. *Macromolecules* **1998**, *33*, 857.

64. Zhang, X.; Berry, B. C.; Yager, K. G.; Kim, S.; Jones, R. L. *ACS Nano* **2008**, *2*, 2331.

65. Harrrison, C.; Park, M.; Chaikin, P.; Register, R. A.; Adamson, D. H.; yao, N.; *Macromolecules* **1998**, *31*, 2185.

66. Sakurai, S.; Kawada, H.; Hashimoto, T.; Fetters, L. J. *Macromolecules* **1993**, *26*, 5796.

67. Kimishima, K.; Koga, T.; Hashimoto, T. *Macromolecules* **2000**, *33*, 968.

68. Hajduk, D. A.; Gruner, S. M.; Rangarajan, P.; Register, R. A.; Fetters, L. J.; Honeker, C.; Albalak, R. J.; Thomas, E. L. *Macromolecules* **1994**, *27*, 490.

69. van Krevelen, D. W.; Hoftyzer, P. J. *Properties of Polymers: Their Estimation and Correlation Length With Chemical Structure*; 2nd ed. ed.; Elsevier Scientific Publishing Company: New York, NY, 1976.

70. Zielinski, J. M.; Duda, J. L. *AIChE Journal* **1992**, *38*, 405.

71. Rauch, J.; Köehler, W. *J. Chem. Phys.* **2003**, *119*, 11977.

72. Mori, K.; Hasegawa, H.; Hashimoto, T. *Polymer* **1990**, *31*, 2368.

73. Elbs, H.; Drummer, C.; Abetz, V.; Krausch, G. *Macromolecules* **2002**, *35*, 5570.

74. Kim, G.; Libera, M. *Macromolecules* **1998**, *31*, 2569.

75. Keddie, J. L.; Jones, R. A. L.; Cory, R. A. *Faraday Discuss*. **1994**, *98*, 219.

76. Grohens, Y.; Brogly, M.; Labbe, C.; David, M.-O.; Schulta, J. *Langmuir* **1998**, *14*, 2929.

77. Wallace, W. E.; van Zanten, J. H.; Wu, W. L. *Phys. Rev. E* **1995**, *52*, R3329.

78. van Zanten, J. H.; Wallace, W. E.; Wu, W.-L. *Phys. Rev. E* **1996**, *53*, R2053.

79. Niu, S.; Saraf, R. F. *Macromolecules* **2003**, *36*, 2428.

80. Kim, J. K.; Han, C. D. *Macromolecules* **1992**, *25*, 271.

81. Schmidt, S. C.; Hillmyer, M. A. *Macromolecules* **1999**, *32*, 4794.

82. Helfand, E.; Tagami, Y. *J. Chem. Phys.* **1972**, *56*, 3592.

83. Noolandi, J.; Hong, K. M. *Ferroelectrics* **1980**, *30*, 117.

84. Whitmore, M. D.; Vavasour, J. D. *Macromolecules* **1992**, *25*, 2041.

85. Huang, C.-I.; Lodge, T. P. *Macromolecules* **1998**, *31*, 3556.

86. Hong, K. M.; Noolandi, J. *Macromolecules* **1983**, *16*, 1083.

87. Olvera de la Cruz, M. *J. Chem. Phys.* **1989**, *90*, 1995.

88. Fredrickson, G. H.; Leibler, L. *Macromolecules* **1989**, *22*, 1238.

89. Lodge, T. P.; Pan, C.; Jin, X.; Liu, Z.; Zhao, D.; Maurer, W. W.; Bates, F. S. *J. Poly. Sci. B* **1995**, *33*, 2289

90. Lodge, T. P.; Hamersky, M. W.; Hanley, K. J.; Huang, C.-I. *Macromolecules* **1997**, *30*, 6139.

91. Lodge, T. P.; Hanley, K. J.; Pudil, B.; Alahapperuma, V. *Macromolecules* **2003**, *36*, 816.

92. Banaszak, M.; Whitmore, M. D. *Macromolecules* **1992**, *25*, 3406.

93. Lai, C.; Russel, W. B.; Register, R. A. *Macromolecules* **2002**, *35*, 841.

94. Hanley, K. J.; Lodge, T. B. J. Poly. Sci. B 1998, 36, 3101.

95. Hamley, I. W.; Fairclough, J. P. A.; Ryan, A. J.; Ryu, C. Y.; Lodge, T. B.; Gleeson, A. J.; Pederson, J. S. *Macromolecules* **1998**, *31*, 1188.

96. Hanley, K. J.; Lodge, T. P.; Huang, C.-I. *Macromolecules* **2000**, *33*, 5918.

97. Liu, Y.; Li, M.; Bansil, R.; Steinhart, M. *Macromolecules* **2007**, *40*, 9482.

98. Li, M.; Liu, Y.; Nie, H.; Bansil, R.; Steinhart, M. *Macromolecules* **2007**, *40*, 9491.

99. Holmqvist, P.; Fytas, G.; Pispas, S.; Hadjichristidis, N.; Saijo, K.; Tanaka, H.; Hashimoto, T. *Macromolecules* **2004**, *37*, 4909.

100. Hashimoto, T.; Shibayama, M.; Kawai, H. *Macromolecules* **1983**, *16*, 1093.

101. Shibayama, M.; Hashimoto, T.; Hasegawa, H.; Kawai, H. *Macromolecules* **1983**, *16*, 1427.

102. Shibayama, M.; Hashimoto, T.; Kawai, H. *Macromolecules* **1983**, *16*, 1434.

103. Skoulios, A.; Finaz, G.; Parrod, J. C. R. *Hebd. Seances Sci.* **1960**, *251*, 739.

104. Skoulios, A,; Finaz, G. C. R. *Hebd. Seances Acad. Sci.* **1961**, *252*. 3467.

105. Fink, G.; Skoulios, A.; Sadron, C. C. R. *Hebd. Seances Acad. Sci.* **1961**, *253*, 265.

106. Vanzo, E. *J. Polym. Sci., Part A-I* **1966**, *4*, 1727.

107. Whitmore, M. D.; Noolandi, J. *J. Chem. Phys.* **1990**, *93*, 2946.

108. Almdal, K.; J.H., R.; Bates, F. S.; Wignall, G. D.; Fredrickson, G. H. *Phys. Rev. Lett.* **1990**, *65*, 1112.

109. Helfand, E.; Wasserman, Z. R. *Macromolecules* **1976**, *9*, 879.

110. Mansky, P.; Russell, T. P.; Hawker, C. J.; Mays, J.; Cook, D. C.; Satija, S. K. *Phys. Rev. Lett.* **1997**, *79*, 237.

111. Mansky, P.; Liu, Y.; Huang, E.; Russell, T. P.; Hawker, C. J. *Science* **1997**, *275*, 1458.

112. Park, M.; Harrison, C.; Chaikin, P. M.; Register, R. A.; Adamson, D. H. *Science* **1997**, *276*, 1401.

113. Park, M.; Chaikin, P. M.; Register, R. A.; Adamson, D. H. *Appl. Phys. Lett.* **2001**, *79*, 257.

114. Black, C. T.; Ruiz, R.; Breyta, G.; Cheng, J. Y.; Colburn, M. E.; Guarini, K. W.; Kim, H.-C.; Zhang, Y. *IBM J. Res. Dev.* **2007**, *51*, 605.

115. Sundrani, D.; Sibener, S. J. *Macromolecules* **2002**, *35*, 8531.

116. Rockford, L.; Liu, Y.; Mansky, P.; Russell, T. P.; Yoon, M.; Mochrie, S. G. J. *Phys. Rev. Lett.* **1999**, *82*, 2602.

117. Jung, Y. S.; Ross, C. A. *Adv. Mater.* **2009**, *21*, 2540.

118. Jung, Y. S.; Ross, C. A. *Nano. Lett.* **2007**, *7*, 2046.

119. Jung, Y. S.; Chang, J. B.; Verploegen, E.; Berggren, K. K.; Ross, C. A. *Nano. Lett.* **2010**, *10*, 1000.

120. Wan., L.; Yang, X. M. *Langmuir* **2009**, *25*, 12408.

121. Hirai, T.; Leolukman, M.; Hayakawa, T.; Kakimoto, M.; Gopalan, P. *Macromolecules* **2008**, *41*, 4558.

122. Hirai, T.; Leolukman, M.; Jin, S.; Goseki, R.; Ishida, Y.; Kakimoto, M.; Hayakawa, T.; Ree, M.; Gopalan, P. *Macromolecules* **2009**, *42*, 8835.

123. Hirai, T.; Leolukman, M.; Jin, S.; Liu, C. C.; Han, E.; Kim, Y. J.; Ishida, Y.; Hayakawa, T.; Kakimoto, M.; Nealey, P. F.; Gopalan, P. *Adv. Mater.* **2009**, *21*, 4334.

124. Mansky, P.; Russell, T. P.; Hawker, C. J.; Pitsikalis, M.; Mays, J. *Macromolecules* **1997**, *30*, 6810.

125. Huang, E.; Russell, T. P.; Harrison, C.; Chaikin, P. M.; Register, R. A.; Hawker, C. J.; Mays, J. *Macromolecules* **1998**, *31*, 7641.

126. Huang, E.; Pruzinsky, S.; Russell, T. P.; Mays, J.; Hawker, C. J. *Macromolecules* 1999, 32, 5299-5303.

127. Huang, E.; Mansky, P.; Russell, T. P.; Harrison, C.; Chaikin, P. M.; Register, R. A.; Hawker, C. J.; Mays, J. *Macromolecules* **2000**, *33*, 80.

128. Kim, H. C.; Jia, X. Q.; Stafford, C. M.; Kim, D. H.; McCarthy, T. J.; Tuominen, M.; Hawker, C. J.; Russell, T. P. *Adv. Mater.* **2001**, *13*, 795.

129. In, I.; La, Y. H.; Park, S. M.; Nealey, P. F.; Gopalan, P. *Langmuir* **2006**, 22, 7855.

130. Han, E.; In, I.; Park, S. M.; La, Y. H.; Wang, Y.; Nealey, P. F.; Gopalan, P. *Adv. Mater.* **2007**, 19, 4448.

131. Han, E.; Stuen, K. O.; La, Y.-H.; Nealey, P. F.; Gopalan, P. *Macromolecules* **2008**, *41*, 9090.

132. Kim, G.; Libera, M. *Macromolecules* **1998**, *31*, 2670.

133. Sidorenko, A.; Tokarev, I.; Minko, S.; Stamm, M. *J. Am. Chem. Soc.* **2003**, 125, 12211.

134. Tokarev, I.; Krenek, R.; Burkov, Y.; Schmeisser, D.; Sidorenko, A.; Minko, S.; Stamm, M. *Macromolecules* **2005**, *38*, 507.

135. Albert, J. N. L.; Young, W.-S.; Lewis, R. L.; Bogart, T. D.; Smith, J. R.; Epps, T. H. *ACS Nano* **2011**, *ASAP*.

136. Angelescu, D. E.; Waller, J. H.; Adamson, D. H.; Deshpande, P.; Chou, S. Y.; Register, R. A.; Chaikin, P. M. *Adv. Mater.* **2004**, *16*, 1736.

137. Pelletier, V.; Adamson, D. H.; Register, R. A.; Chaikin, P. *App. Phys. Lett.* **2007**, 90, 163105.

138. Morkved, T. L.; Lu, M.; Urbas, A. M.; Ehrichs, E. E.; Jaeger, H. M.; Mansky, P.; Russell, T. P. *Science* **1996**, *273*, 931.

139. Thurn-Albrecht, T.; DeRouchey, J.; Russell, T. P.; Jaeger, H. M. *Macromolecules* **2000**, *33*, 3250.

140. Bita, I.; Yang, J. K. W.; Jung, Y. S.; Ross, C. A.; Thomas, E. L.; Berggren, K. K. *Science* **2008**, *321*, 939.

141. Segalman, R. A.; Yokoyama, H.; Kramer, E. J., *Adv. Mater.* **2001**, *13*, 1152.

142. Cheng, J. Y.; Ross, C. A.; Thomas, E. L.; Smith, H. I.; Vancso, G. J. *Appl. Phys. Lett.* **2002,** *81*, 3657.

143. Cheng, J. Y.; Mayes, A. M. *Nat. Mater.* **2004**, *3*, 823.

144. Cheng, J. Y.; Ross, C. A.; Thomas, E. L.; Smith, H. I.; Vancso, G. J. *Adv. Mater.* **2003**, *15*, 1599.

145. Park, S. M.; Stoykovich, M. P.; Ruiz, R.; Zhang, Y.; Black, C. T.; Nealey, P. E. *Adv. Mater.* **2007**, *19*, 607.

146. Ruiz, R.; Ruiz, N.; Zhang, Y.; Sandstrom, R. L.; Black, C. T. Adv. Mater., 2007, 19, 587-591.

147. Chen, F.; Akasaka, S.; Inoue, T.; Takenaka, M.; Hasegawa, H.; Yoshida, H. *Macromol. Rapid. Commun.* **2007**, *28*, 2137.

148. Kim, S. O.; Solak, H. H.; Stoykovich, M. P.; Ferrier, N. J.; de Pablo, J. J.; Nealey, P. F. *Nature* **2003**, *424*, 411.

149. Edwards, E. W.; Stoykovich, M. P.; Solak, H. H.; Nealey, P. F. *Macromolecules* **2006,** *39*, 3598.

150. Welander, A. M.; Kang, H.; Stuen, K. O.; Solak, H. H; Müller, M.; de Pablo, J. J.; Nealey, P. F. *Macromolecules* **2008,** *41*, 2759.

151. Ruiz, R.; Kang, H.; Detcheverry, F. A.; Dobisz, E.; Kercher, D. S.; Alberecht, T. R.; de Pablo, J. J.; Nealey, P. F. *Science* **2008**, *321*, 936.

152. Cheng, J. Y.; Rettner, C. T.; Snaders, D. P.; Kim, H. C.; Hinsberg, W. D. *Adv. Mater.* **2008**, *20*, 3155

153. Daoulas, K. C.; Müller, M.; Stoykovich, M. P.; Kang, H.; de Pablo, J. J.; Nealey, P. F. *Langmuir* **2008**, *24*, 1284.

154. Stoykovich, M. P.; Daoulas, K. C.; Müller, M.; Kang, H.; de Pablo, J. J.; Nealey, P. F. *Macromolecules* **2010**, *43*, 2334.

155. Edwards, E. W.; Muller, M.; Stoykovich, M. P.; Solak, H. H.; de Pablo, J. J.; Nealey, P. F. *Macromolecules* **2007**, *40*, 90.

CHAPTER2 DIRECTED SELF-ASSEMBLY OF DIBLOCK COPOLYMER THIN FILMS ON CHEMICALLY-PATTERNED SUBSTRATES FOR DEFECT-FREE NANO-PATTERNING

2.1 Introduction

Recently, much effort has been devoted to nanofabrication to enhance the performance of microelectronic devices. Smith et al. have demonstrated 35 nm lines and spaces with immersion 193 nm interferometric lithography.[1] Although photolithography is the industry standard high throughput lithography, the resolution requirements have reached beyond the wavelength of light and it is becoming increasingly complicated and expensive to continue further minimizing the resolution.[2] Electron beam (EB) lithography can routinely produce features of 15-25 nm. Under specialized conditions EB lithography can produce features of 2-5 nm.[3-5] However, the application of direct write EB lithography is very limited by its low throughput. To enhance the available lithographic capabilities, self-assembling processes have received much attention.[6-10] In particular, the self-assembly of block copolymers (BCP) is of interest for this approach.

Diblock copolymers (diBCP) consist of two chemically different immiscible polymers which are joined at the end of each polymer. The diBCPs exhibit a wide variety of morphologies ordered by microphase separation. In diBCP melts, separation of the phases can result in microdomain structures such as lamellar, gyroid, *Fddd*, hexagonally packed cylinder, and a body centered lattice of spheres in the equilibrium configuration.[11-15] The equilibrium morphologies depend on the relative volume fraction of diBCPs and temperature, while the size of the microdomain structures depend on the molecular weight of the diBCPs. The typical sizes of the microdomains are a few tens of nanometers.[12,13] To realize the full

potential of self-assembled structures of BCPs in thin films for lithographic application, I need to attain long-range order. If self-assembled on a surface without template guidance, the diBCP forms several crystal-like grains. The crystal type grains are rotated with respect to each other and are separated by a dislocation or grain boundary. To achieve long-range order, some type of guidance during the microdomain formation process is required. For this purpose, several methods such as graphoepitaxy,[16-21] shear flow,[22] electric fields,[23-27] and solvent evaporation[28,29] have been proposed. In this work, I focus on self-assembled diBCP domain structure on substrates chemically prepatterned with EB lithography.

The effect of a Chemically-Patterned surface on the orientation of microphase separated diBCP was first reported by Rockford et al.[30] The surface prepared by Rockford consisted of alternating stripes of silicon oxide and Au. The surface pattern directed the phase separated structure of Polystyrene-*block*-poly(methyl methacrylate) (PS-*b*-PMMA). Then, Nealey et al. have successfully directed lamellar-[31] and cylinder-forming[32,33] BCP self-assembled microdomains in registration with the lithographic pattern defined in the chemically modified surfaces with a one-to-one correspondence.

Recently, Ruiz et al. attained the interpolation of chemical pattern with a 1:2 correspondence by self-assembly of PS-*b*-PMMA. They patterned hexagonally polystyrene-grafted Si substrate by EB lithography and directed the self-assembling process of cylinder-forming PS-*b*-PMMA.[34] Cheng et al. also succeeded in similar interpolation for a stripe pattern.[35] They used a two-layer system consisting of hydrogen silsequioxane (HSQ) layer on the cross-linked film of poly(styrene-*r*-epoxydicyclopentadiene methacrylate). They etched HSQ to form chemically modified stripe patterns and the self-assembling of lamellar-forming PS-*b*-PMMA on the etched substrate succeeded in duplication of the size of the stripe pattern.

Here I investigate how the chemically prepatterned substrates can control the orientation of the microdomain structure of BCP thin films. In particular, I focus on the registration,

template dimension match, long-range order, and interpolation of the substrate chemical patterns. The combination of the chemically prepatterned substrate and the self-assembling of BCPs is a very promising path to defect-free nanofabrication to 10 nm or below.

The contents of this paper are as follows: In section 2.2, I describe the substrate and sample preparation, characterization of substrates and samples, and observation method of the self-assembled structure. In section 2.3, I show the results of the self-assembled diBCP structure. I first show the microdomain structure of the diBCPs without a template. It is then compared with the microdomain structure of the same diBCPs on chemically prepatterned substrates of systematically varied period. I demonstrate single crystal type microdomain structures on the substrates commensurate with the chemical pattern when the pattern period is almost equal to the equilibrium periodicity of the microdomain structures. The self-assembled patterns correct for defects in the lithographic pattern of the substrate. Subsequently, I show that PS-*b*-PMMA self-assembly can interpolate between features of the chemical template pattern on the substrate, in cases where the template periodicity is close to twice that of the microdomain structure. Finally I conclude our results in section 2.4.

2.2 Experimental Section

2.2.1 Materials.

PS-*b*-PMMA and hydroxy-terminated polystyrene (PS-OH) were purchased from Polymer Source Inc., Quebec, Canada. Characteristics of PS-*b*-PMMA and PS-OH and their code names are listed in Table 2-1.

2.2.2 Substrate Preparation.

Si substrate surfaces were chemically patterned in the following manner. First the Si substrate was cleaned in a piranha solution at 80°C for 15min and rinsed in deionized water.

Table 2-1 Characterization of Polymers Used in This Study[a]

Code	polymer	M_n of PS (g/mol)	M_n of PMMA (g/mol)	M_w/M_n
SMMA-1	PS-*b*-PMMA	4.61×10^4	2.10×10^4	1.09
SMMA-2	PS-*b*-PMMA	3.55×10^4	1.22×10^4	1.04
PS-1	PS-OH	9.0×10^2	-	1.13
PS-2	PS-OH	3.7×10^3	-	1.08
PS-3	PS-OH	1.0×10^4	-	1.07

[a] M_n: number-average molecular weight, M_w/M_n: heterogeneity index

Table 2-2 Characterization of Polystyrene Graft Layer

PS-OH	XPS C_{1S} intensity (cps)	Thickness (nm)	Contact angle of PS at 170˚C (deg)
PS-1	8.9×10^3	1.7	24
PS-2	2.7×10^4	5.1	6
PS-3	3.6×10^4	8.7	0

Next, a 1.0 wt % PS-OH solution in toluene was spin-coated onto the Si substrate to a thickness of about 50 nm. The grafting of PS on the Si substrate was completed by annealing the PS-OH-coated Si wafer in vacuum at 140 °C for 48 h. Unreacted PS-OH was removed by rinsing the substrate with toluene. I investigated three kinds of grafted PS-OH chemical templates, each with a different molecular weight, as listed in Table 2-1. Table 2-1 also shows the molecular weights of the diBCPs that were later deposited on the substrates. The measured characteristics of each grafted layer are listed in Table 2-2. In Table 2-2, one can see that the average thickness of PS grafted layer increased with molecular weight of PS-OH, and the wettability of PS to the PS grafted surface also increased with the molecular weight of the PS-OH.

Next, the PS-grafted layer was patterned by EB lithography. The patterning process is schematically shown in Figure 2-1. PMMA resist was spin-coated onto the PS-grafted Si

substrate (Figure 2-1(a)) to thicknesses of 60 or 85 nm. The 60 nm PMMA was used with diBCP, SMMA-2, to achieve finer period e-beam patterns. The samples were exposed by electron-beam in hexagonal arrays of dots with a Vistec VB6, e-beam lithography system and developed in 3:1 isopropanol:deionized water at 4 °C, under ultrasonic agitation. Since the dots were, e-beam exposed, development removed only the dots in the PMMA. The samples were subsequently etched in a Surface Technology Systems Multiplex Inductive Coupled Plasma instrument with an O_2 environment. The etching time was short, 5-10 s, so that the PMMA mask remained and only the grafted PS in the holes was selectively reacted with the plasma. The PMMA mask was removed by rinsing the substrate with *N*-methyl-2-pyrolidone and/or toluene, leaving a chemically prepatterned substrate. The details of the patterns are described below.

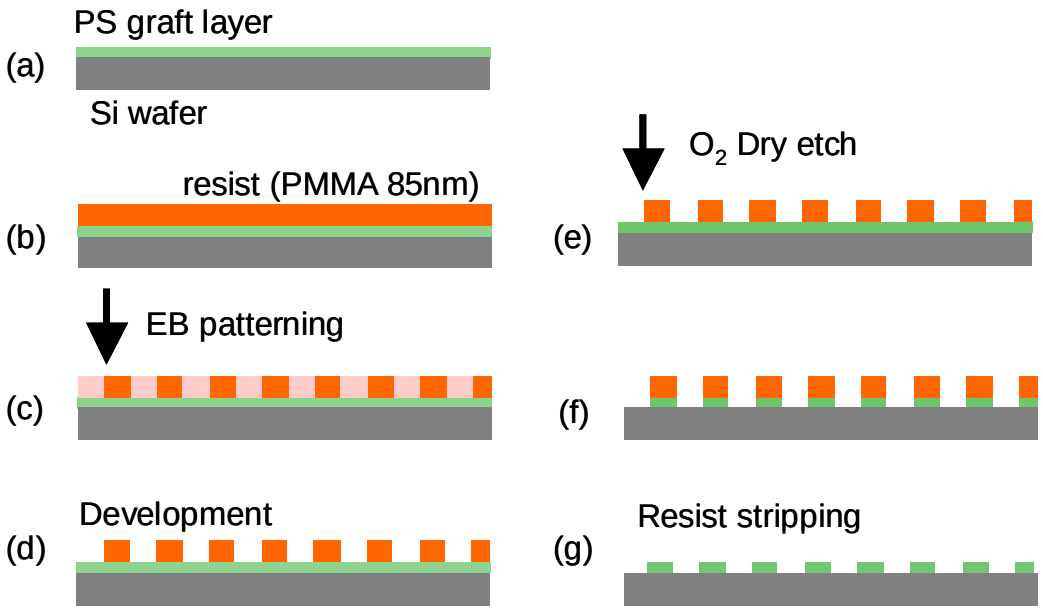

Figure 2-1. Schematic illustration of EB lithography process to form chemically prepatterned substrate.

2.2.3 Sample Preparation.

Thin films of PS-*b*-PMMA were spin-coated from a dilute solution in toluene. The thickness of the films was controlled by the concentration of the solutions and the spin speed. The spin-coated samples were then annealed at 170 °C for 12 h in vacuum to reach their equilibrium state.

2.2.4 Scanning Electron Microscope (SEM) Observation.

I observed the microdomain structures of PS-*b*-PMMA by using a Hitachi S-4800 field-emission SEM instrument operated at an acceleration voltage of 0.7kV. For contrast between the PMMA and PS phases, the BCP specimens were etched by O_2 RIE with a SAMCO RIE-10NR. Since the O_2 RIE preferentially etches the PMMA structures, the dark and bright parts of SEM images correspond to PMMA and PS microdomains, respectively.

2.3 Results and Discussion

2.3.1 Microdomain Structures of SMMA-1 and SMMA-2 on a Si Substrate.

In order to establish a basis for comparison, the structures of SMMA-1 and SMMA-2 self-assembled on Si without chemical prepatterning was examined. Figure 2-2(a) shows the SEM image of the thin film of the SMMA-2 on a Si wafer. In this case, the spin-coated SMMA-2 wafer was annealed at 170 °C for 24 h. The film thickness, t_f,was 45 nm. Here most of part in the image exhibits hexagonally packed cylindrical structures of the PMMA domains oriented perpendicular to the film surface, although there are some regions where PMMA domains oriented parallel to the film surface. However, the extent of the hexagonal lattices on the surface was broken by grain boundaries and the film exhibits a poly granular structure. It should be noted that perpendicular orientation can be formed without any treatment on Si substrate, although I usually need to treat the surface, such as random copolymer or corrugated substrate, to form the perpendicular orientation. This may be

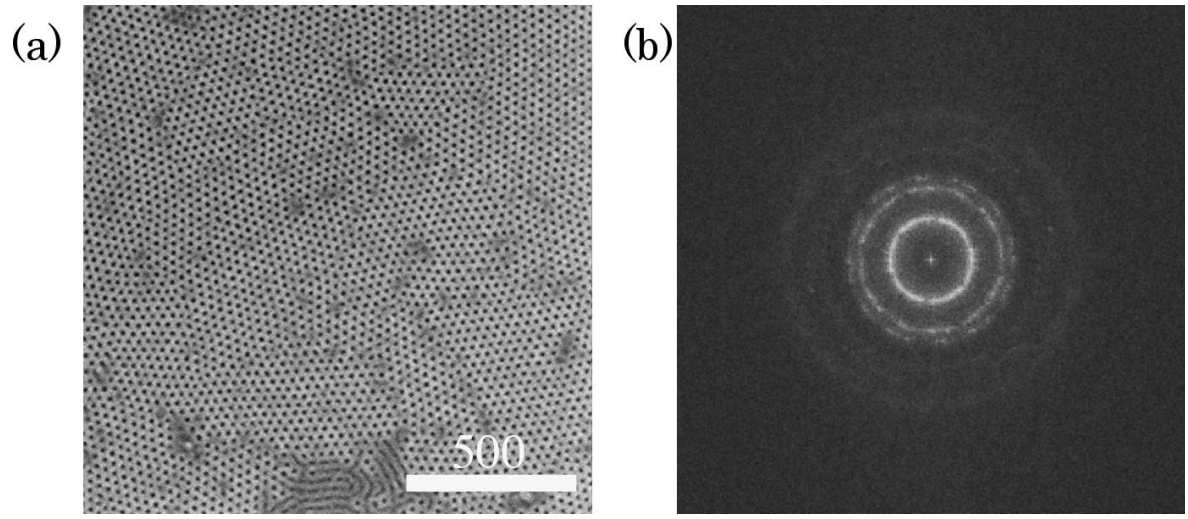

Figure 2-2. (a) SEM image of SMMA-2 on Si substrate and (b) corresponding 2D-FFT image.

because the thickness of the sample is suitable for the perpendicular orientation. Actually, the thickness of the parallel orientation regions is thicker than that of the perpendicular orientation. Figure 2-2(b) is a 2-dimensional Fast Fourier Transform (2D-FFT) image of the region having perpendicular orientation in the Figure 2-2(a). There are several higher order peaks, with up to sixth order, at q/q_m = 1, √3, √4, √7, √9, and √12, with q_m being the first order peak of the 2D-FFT image. The 2D-FFT image shows that the cylinders were packed regularly on a hexagonal lattice within the grains. However, the 2D-FFT image has isotropic halos with some spots. This pattern suggests a poly crystalline type structure with several hexagonal lattices that are not of the same orientation. From first order peak positions, the intrinsic domain spacing of the self-assembled lattice, d_0, on Si substrate was calculated to be 24 nm. Similar results were obtained for the SMMA-1 thin film on a Si substrate, with d_0 of 32 nm.

2.3.2 Characterization of Chemically Prepatterned Substrate.

Two types of substrate patterns were investigated: one with $d_S \approx d_0$, and the other with $d_S \approx 2d_0$, where d_S is the d-spacing specified in the e-beam digital file. The pattern with $d_S \approx 2d_0$ was used to test whether the self-assembling process of PS-*b*-PMMA can interpolate the chemical pattern. A matrix of array patterns, in which the array spacing was varied in 1 nm steps about $d_S \approx d_0$ and $d_S \approx 2d_0$, were written on the substrate. The radius of the dots in the grafted layer was ~10 nm. The nature and magnitude of defects in the original e-beam patterns were observed through SEM image of the original PMMA mask. The PMMA mask was sputter coated with 1.8 nm of Pt-Pd prior to SEM measurement. Figure 2-3 shows SEM images of PMMA-mask patterned with $d_S \approx d_0$ for SMMA-1 and SMMA-2 and $d_S \approx 2d_0$ for SMMA-2. While there were several defects in the smaller d_S patterns (Figure 2-3, parts (a) and (b)), there were almost no defects in the larger d_S patterns (Figure 2-3, parts (c) and (d)). A summary of the characterization of the e-beam patterns is given in Table 2-3. L_S is the nearest lattice distance specified in e-beam pattern file. The parameters, d_S and L_S, are limited to 1 nm integers due to the resolution of the digital grid for the e-beam tool. The parameter dobs is the average *d*-spacing measured from SEM micrographs, and σ is the standard deviation of measured *d*-spacings from the average measured value. The final column on the right gives the diBCP and parameter relevant to the e-beam patterns. The method by which d_{obs}, and σ were calculated is described in below.

Here I shall show the procedure to estimate the standard deviation σ of the distance between the centers of the PMMA domains. First, I determined the center of PMMA domain from the SEM image (Figure 2-4) and applied FFT to the obtained distribution of the centers (Figure 2-5). Then, I calculated an autocorrelation 2D pattern (Figure 2-6) from the 2D-FFT pattern, circularly averaged the autocorrelation 2D pattern to obtain a radial distribution function g(r) (Figure 2-7). By fitting the first order peak reflecting the distribution of the distance between nearest neighbor centers of gravity with Gaussian

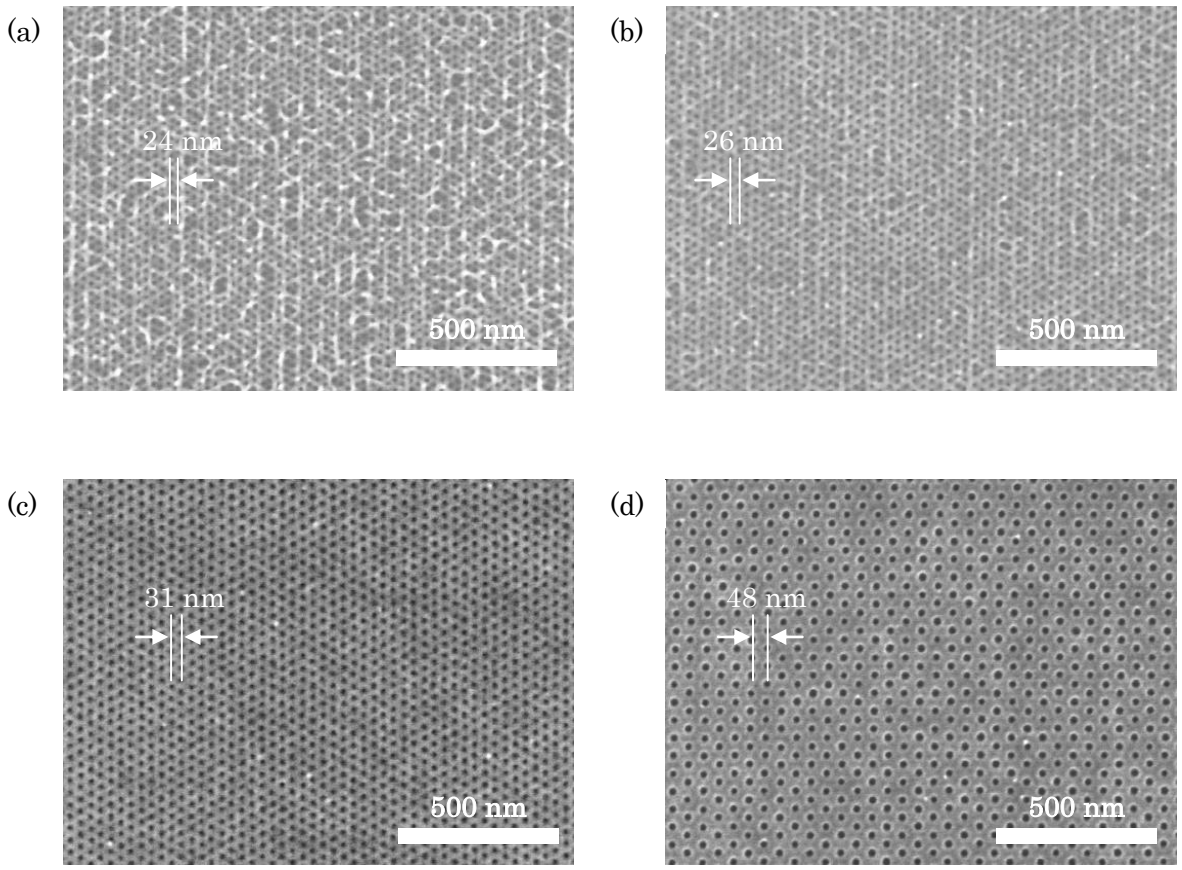

Figure 2-3. SEM images of patterns of PMMA resist formed with EB lithographic process. (a) d_S = 24 nm, (b) d_S = 26 nm, (c) d_S = 31 nm, and (d) d_S = 48 nm.

Table 2-3. Characterization of Patterns Formed with EB Lithography

d_S (nm)	L_S (nm)	d_{obs} (nm)	σ (nm)	
24	28	23.8	5.2	$d_S \approx d_0$ for SMMA-2
26	30	26.0	3.6	$d_S \approx d_0$ for SMMA-2
47	54	47.5	2.2	$d_S \approx 2d_0$ for SMMA-2
48	56	48.4	2.0	$d_S \approx 2d_0$ for SMMA-2
50	58	50.7	2.4	$d_S \approx 2d_0$ for SMMA-2
31	36	31.0	2.8	$d_S \approx d_0$ for SMMA-1
32	36	32.2	2.5	$d_S \approx d_0$ for SMMA-1
61	70	61.3	3.6	$d_S \approx 2d_0$ for SMMA-1
62	72	63.2	3.8	$d_S \approx 2d_0$ for SMMA-1
64	74	64.8	2.6	$d_S \approx 2d_0$ for SMMA-1

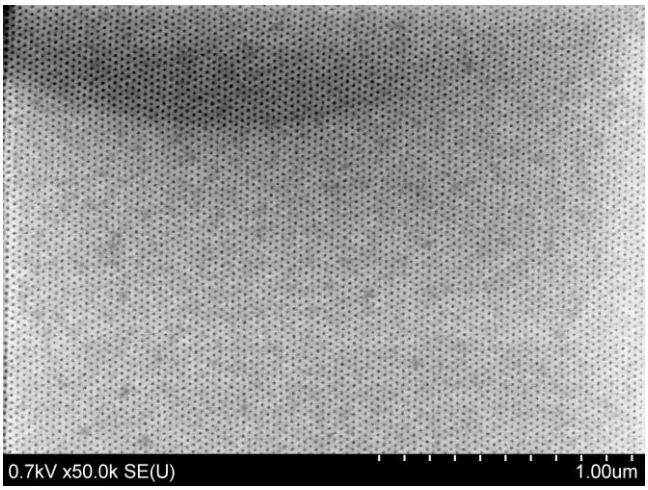

Figure 2-4. SEM image of microdomain structure of BCPs.

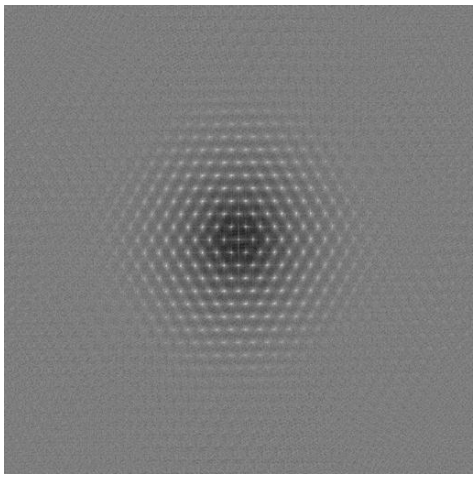

Figure 2-5. 2D-FFT image of Figure 2-4.

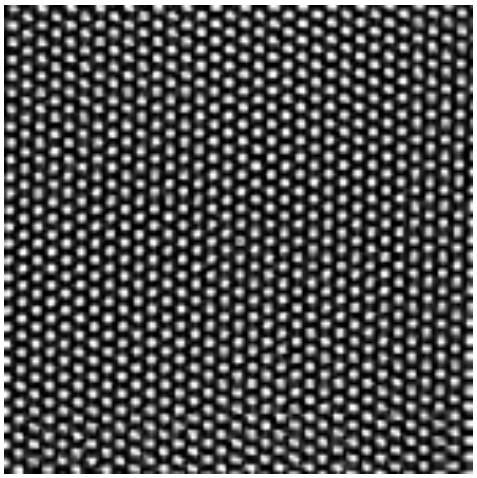

Figure 2-6. Autocorrelation patterns of Figure 2-4.

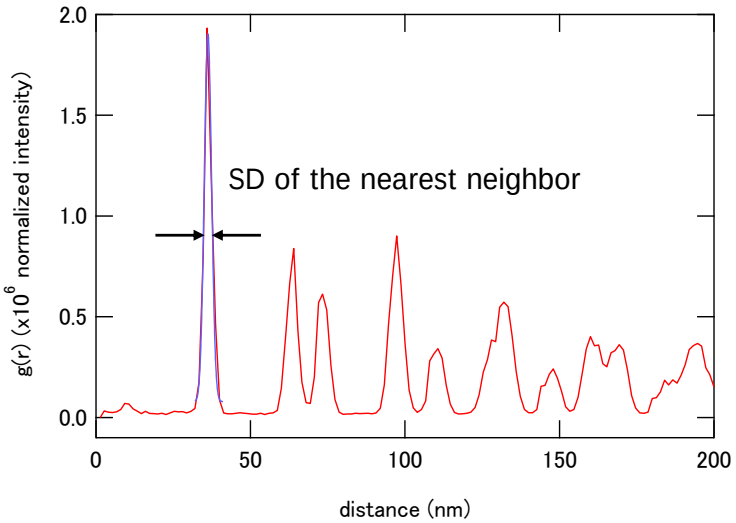

Figure 2-7. Radial distribution function g(r) plotted as a function of the distance r.

function I estimated the standard deviation σ.

2.3.3 Microdomain Structures of PS-*b*-PMMA on Chemically Prepatterned Substrates with $d_S \approx d_0$.

Figure 2-8(a) shows the SEM image of the microdomain structures of SMMA-1 on chemically prepatterned substrate with d_S= 31 nm being nearly equal to the *d*-spacing of SMMA-1, d_0 = 32 nm. The thickness of the SMMA-1 film was t_f = 48 nm. PS-2 was used as the PS-grafted layer. In the case of the thin film of SMMA-1 on the Si substrate, poly grain structure was observed as shown in Figure 2-2. On the other hand, the microdomain ordered structure on the chemically prepatterned substrate did not have any defects and formed a single hexagonal lattice commensurate with the chemical pattern beneath. Moreover, further SEM observation showed that the single hexagonal lattice extended all over the entire 100 × 100 μm2 extent of the chemically prepatterned region. Figure 2-8(b) is the 2D-FFT image of the SEM image of Figure 2-8(a). In contrast to the 2D-FFT pattern of the thin film of SMMA-1 on the Si substrate without a chemically prepatterned template (Figure 2-2(b)),

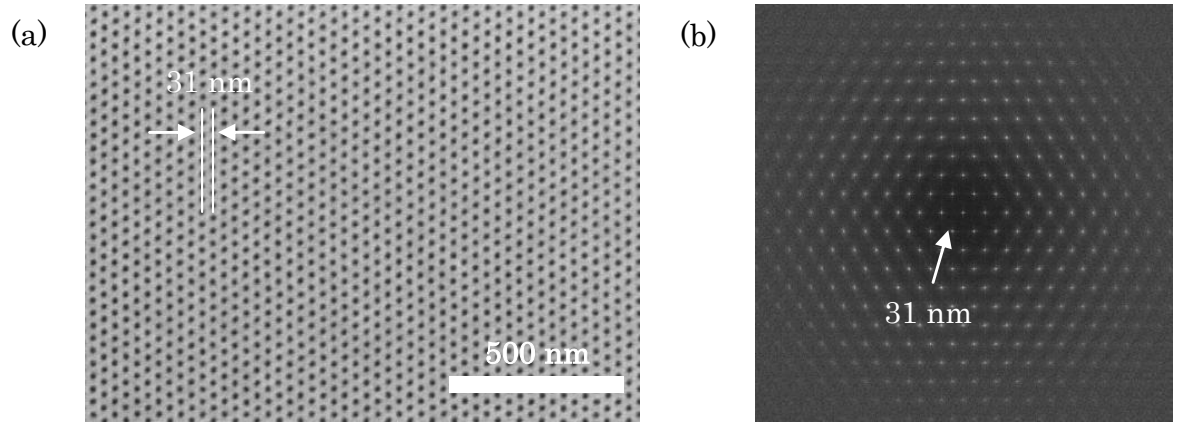

Figure 2-8. (a) SEM image of self-assembled microdomain structures of SMMA-1 on the chemically prepatterned substrate with d_S = 31 nm and (b) the corresponding 2D-FFT image.

the 2D-FFT image of the diBCP ordered on the chemical template exhibits only spots as expected from a single hexagonal lattice, with peaks up to the 11th order. The results show that the microdomain structure formed a well-oriented hexagonal lattice pattern along the chemically prepatterned substrate with long-range order. The *d*-spacing calculated from the 2D-FFT was 31 nm, which equaled the *d*-spacing of the substrate but was slightly smaller than the *d*-spacing of the SMMA-1 film on the Si substrate. Thus the domain spacing was constrained by the pattern of the substrate.

Figure 2-9(a) shows the SEM images of the domain structures of SMMA-2 (d_0 = 24 nm) on chemically prepatterned substrate with d_S = 24 nm. The thickness of the film was 48 nm. PS-2 was used as the PS-grafted layer. Similar to the result of the case of SMMA-1, the cylindrical microdomains on chemically prepatterned substrate form a single hexagonal lattice commensurate with the lattice of the chemically prepatterned substrate. In the 2D-FFT image (Figure 2-9(b)), a spot pattern of a single hexagonal lattice was found.

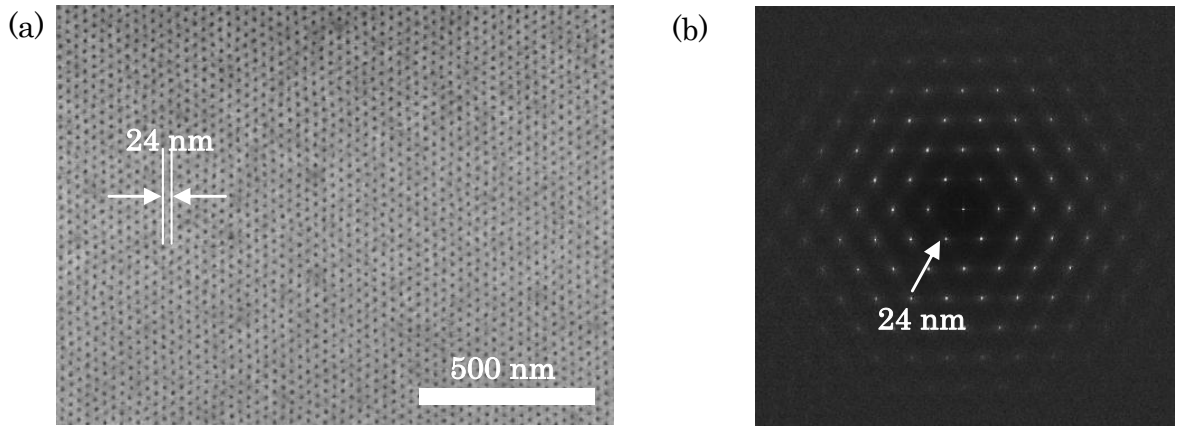

Figure 2-9. (a) SEM image of self-assembled microdomain structures of SMMA-2 on the chemically prepatterned substrate with d_S = 24 nm and (b) the corresponding 2D-FFT image.

Table 2-4. Quantitative Comparison of d and σ between Patterns Formed with EB Lithography only and That of Self-Assembling Structure of PS-*b*-PMMA on the chemically prepatterned Substrate

target d_S (nm)	EB lithography		microdomain	
	d_{obs} (nm)	σ (nm)	*d* (nm)	σ (nm)
24	23.8	5.3	24.1	2.6
48	48.3	2.0	23.8	2.6

To estimate the precision of the hexagonal lattice quantitatively, I calculated the *d*-spacing dobs and the standard deviation of nearest neighbor lattice distance σ for the vertically oriented cylindrical microdomain structure of the SMMA-2 on the patterns with d_S = 24 nm and compared them with those for the patterns formed with EB lithography process as listed in Table 2-4. The *d*-spacing for the microdomain structure agrees with that of the e-beam patterns. However, the standard deviation of the lattice spacing, σ, for the microdomain structure was measured to be 2.6 nm, which was half-that of the EB pattern. This results clearly shows that the self-assembling process of the BCP can correct patterns formed with EB lithography. Similar result has been found by Ruiz et al.[34] They also investigated the directed self-assembling process of cylinderforming PS-*b*-PMMA on e-beam pattern and standard deviation of dot placement errors has been found to be much improved in comparison to the e-beam pattern.

2.3.4 Effects of the Mismatch between d_S and d_0 on the Microdomain Structures on Chemically Prepatterned Substrates with $d_S \approx d_0$.

As described above, the chemically prepatterned substrates can control the orientation and spacing of the microdomain structure of the diBCP. I now investigate, the amount of lattice mismatch the lithographically guided self-assembly process can tolerate. Figure 2-10

shows the SEM and 2D-FFT images of the microdomain structure of SMMA-1 (d_0 = 32 nm) on the chemically prepatterned substrates with different values for d_S. The diBCP film thickness was t_f = 48 nm and PS-2 was used as the PS-graft layer. As shown in Figure 2-10, the regularity and the long-range order of PS-*b*-PMMA become worse with increasing the mismatch between d_S and d_0. In the case of d_S = 35 nm, there are some grains and the defects between grains in the SEM image (Figure 2-10(a)). Although the 2D-FFT image still shows a hexagonal pattern, reflecting the single orientation of the domain structure, the peaks are broader than those of d_S = 32 nm, and the higher order peaks have been lost. The *d*-spacing of the domain structure the perpendicular orientation. Actually, the thickness of the parallel orientation regions is thicker than that of the perpendicular orientation. Figure e packed regularly on a hexagonal lattice within the grains. However, the 2D-FFT image has isotropic halos with some spots. This pattern suggests a poly crystalline type structure with several hexagonal lattices that are not of the same orientation. From first order peak positions, the intrinsic domain spacing of the self-assembled lattice, d_0, indicating little interaction with substrate surface.

I investigated the azimuthal dependence of the first peak intensity in 2D-FFT image to quantify the distribution of the orientation of the lattice structures. Figure 2-11 shows the azimuthal angle dependence of the first peak intensity in 2D-FFT image shown in Figures 2-8 and 10. The peaks become broader with with d_S. The width w obtained by fitting the peaks at 180° with Gaussian function are 3.3° and 9.8° for d_S = 31 and 35 nm, respectively, and I can not fit the data for d_S = 37 and 41 nm with Gaussian function.

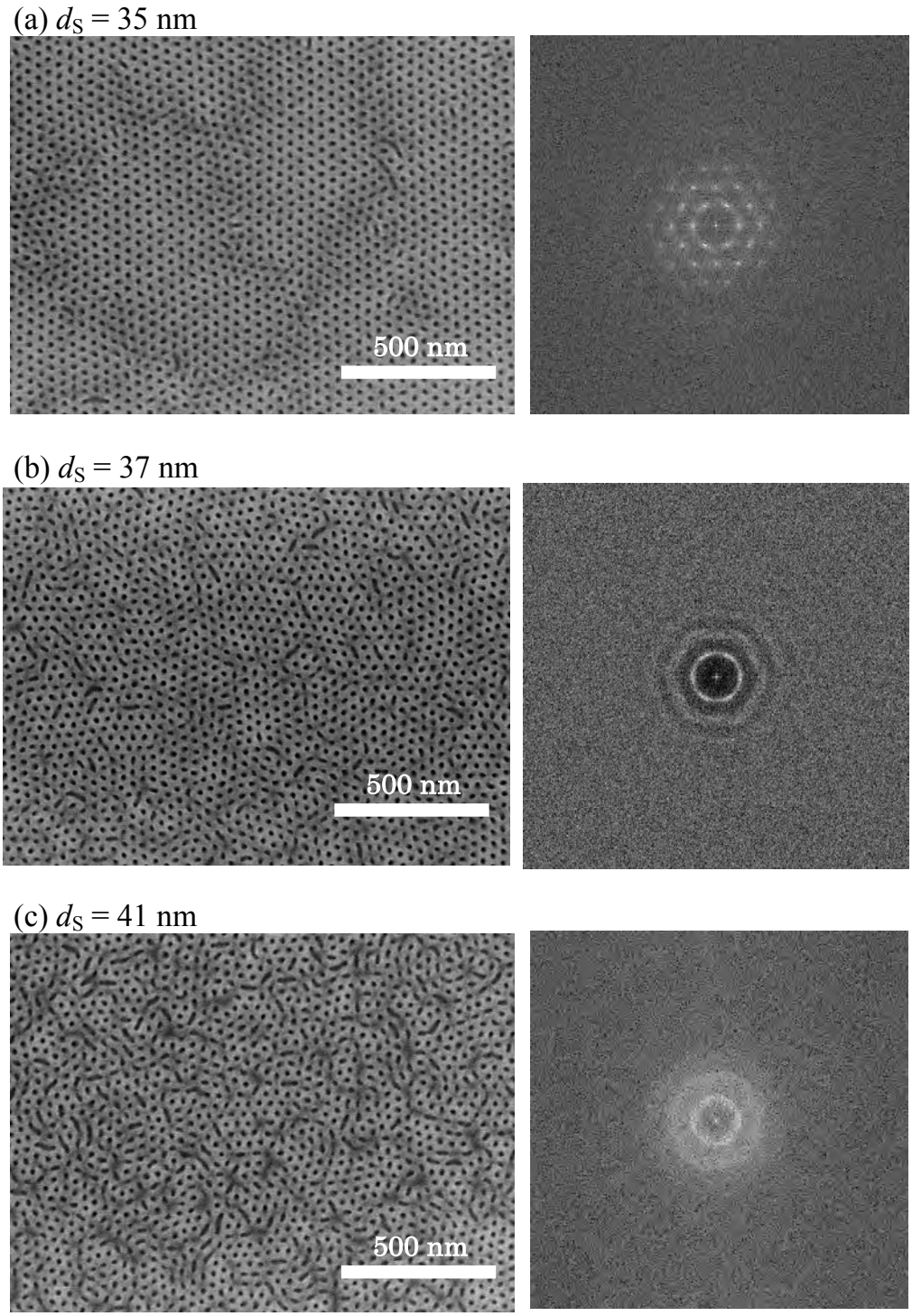

Figure 2-10. SEM images and corresponding 2D-FFT images for selfassembled microdomain structures of SMMA-1 on the chemically prepatterned substrate with (a) d_S = 35 nm, (b) d_S = 37 nm, and (c) d_S = 41 nm.

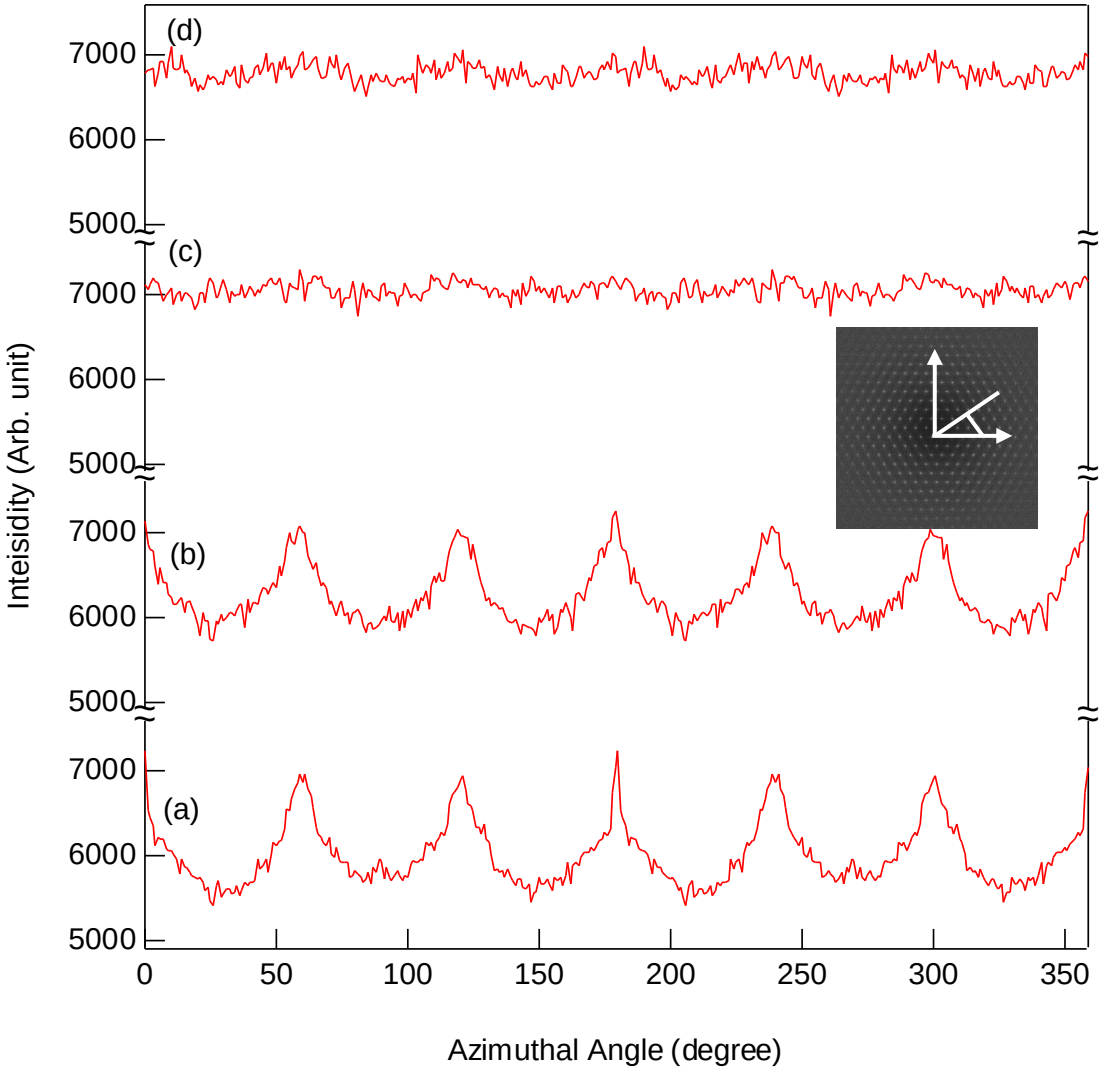

Figure 2-11. Azimuthal angle dependence of first peak intensity in 2DFFT image for (a) d_S = 31 nm, (b) d_S = 35 nm, (c) d_S = 37 nm, and (d) d_S = 41 nm.

The results are interpreted as a thermodynamic competition between the enthalpy of the lower surface energy in aligning the diBCP domains with the surface chemical pattern, and the loss of conformational entropy as the chains stretch to achieve the lattice spacings of the chemical patterns that increasingly became larger than the equilibrium spacing for that diBCP. Up to a 10% stretch of the lattice spacing (d_S = 35 nm), the surface interaction enthalpy dominates and determines d_S of the diBCP. However, the loss of entropy due to the

extension of the polymer chains causes the loss of the long-range order so that the thin film can not maintain the single crystal-like structure and multiple grains form to relieve the stress. As the stretch of the lattice spacing becomes 15% (d_S = 37 nm), the substrate pattern still tends to control the *d*-spacing of the microdomain structure, but the loss of entropy term becomes comparable and an isotropic microdomain structure with *d*-spacing of 32 nm region appears as a large defects. As the surface pattern stretches d_S by 27% (d_S = 41 nm), the surface energy can not make up for the loss of the entropy and the entropy term dominates the control of the *d*-spacing of the microdomain structure. However, the substrate patterns limit the size of the ordered regions with d_0 aligning and prevent any long-range order. Thus, the random orientation is observed in the SEM image. The SEM image of the microdomain structures of SMMA-2 (d_0 = 24 nm) on the chemically prepatterned substrate with d_S =26 nm, which is an 8% stretch relative to d_0, is shown in Figure 2-12(a). Differing from the case of the chemically prepatterned substrate with d_S = 24 nm (Figure 2-9), the hexagonal lattice was found to be distorted and the points had a variation in position off the correct lattice points.

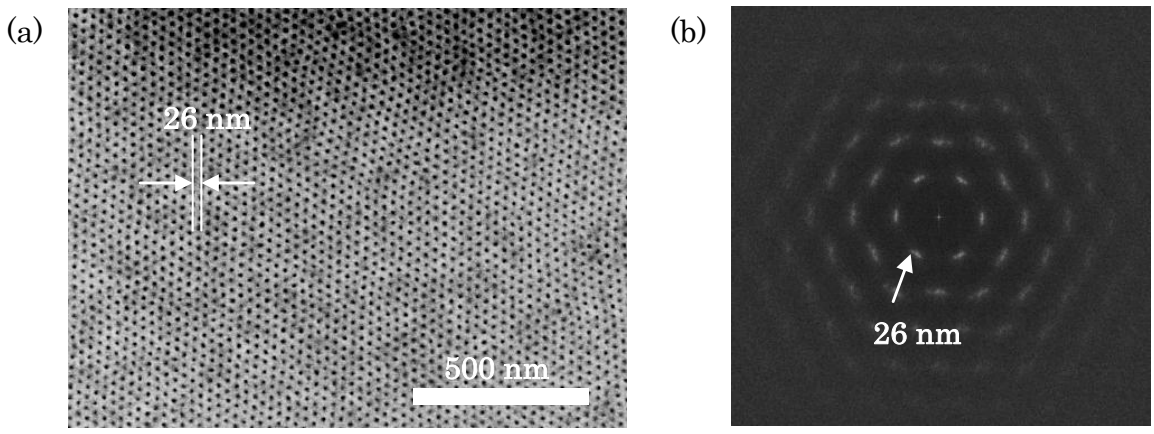

Figure 2-12. (a) SEM image of self-assembled microdomain structures of SMMA-2 on the chemically prepatterned substrate with d_S = 26 nm and (b) the corresponding 2D-FFT image.

The 2D-FFT image for d_S = 26 nm displayed a spot-like pattern forming a hexagonal lattice indicating that the *d*-spacing of the chemical pattern of 26 nm was still preserved. However, the spots are broader than those of the d_S = 24 nm case, suggesting that the hexagonal lattice of the microdomain structure was distorted and the lattice points had some spread in orientations. The lack of the long-range order for d_S = 26 nm is caused by the mismatch between d_0 and d_S.

Kim et al. have investigated how the mismatch between d_0 and d_S affects the long-range order of the microdomain structure in lamellar systems of PS-*b*-PMMA.[31] For $d_S < d_0$, although *d*-spacing becomes d_S and there are few defects in the microdomains, the most of part of the microdomains is well registered and epitaxial to the surface pattern. On the other hand, for $d_S > d_0$, there are found to be the two kinds of defects: the formation of herringbone patterns and the unregistered lamellae with d_0. They found the fraction of the unregistered lamellae with d_0 increases with the mismatch. This increase agrees with the case of cylinder-forming systems.

2.3.5 Effects of Molecular Weight of PS-OH on the Orientation of the Microdomain Structures on chemically prepatterned substrates with $d_S \approx d_0$.

In the previous sections, the chemically prepatterned substrate was formed with PS-2, which had a number-average molecular weight (M_n) of 3,700. Here I investigate the effect of molecular weight of PS-OH surface on the microdomain structure of the diBCPs. Figure 2-13 shows the SEM images of the microdomain structure of SMMA-1 on chemically prepatterned substrates with three different molecular weights of PS-OH. Here the d_S = 32 nm = d_0. The thickness of the films were t_f = 35 nm for all samples. I found that the microdomain structures on chemically prepatterned PS-OH with M_n = 3,700 had fewer defects the than those on chemically prepatterned surfaces with the other molecular weight PS-OH films. The percentage of point defects in the lattice was determined from SEM

(a) M_n = 900

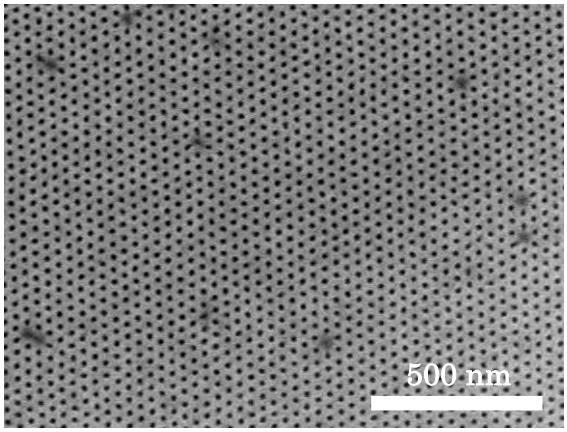

Point defect: 0.9%

(b) M_n = 3,700

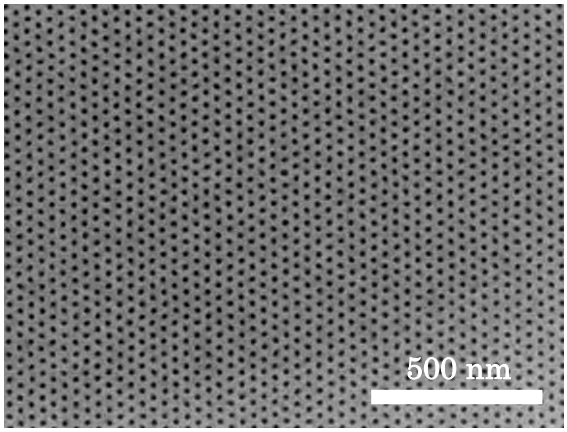

Point defect: 0.01%

(c) M_n = 10,000

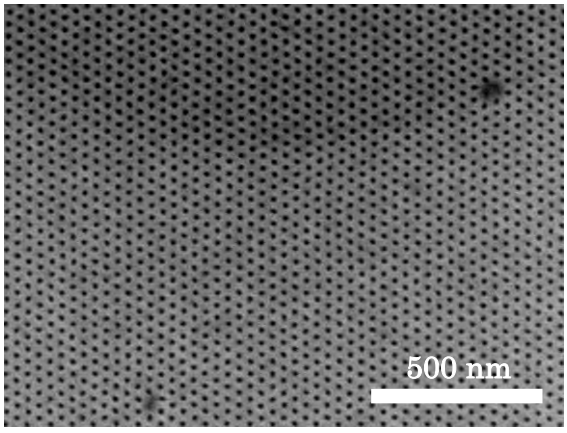

Point defect: 0.05%

Figure 2-13. SEM images of the microdomain structures of SMMA-1 on the chemically prepatterned substrate with (a) PS-1, (b) PS-2, and (c) PS-3. d_S is 32 nm and the film thickness of each sample is 35 nm.

images with 10,000 lattice points to be 0.9%, 0.01%, and 0.05% for PS-1, PS-2, and PS-3, respectively. The results indicate that PS-2 (PS-OH with M_n = 3,700) was optimal as a chemically prepatterned substrate.

From examination of the contact angles, in Table 2-2, I can see that PS-1 has the largest contact angle and poorest wetting of the PS. Thus, the imperfection of the coating may cause the defects in lattice structure. Conversely, the substrate with PS- 3, which also exhibited more defects than the PS-2 substrate, showed much better wetting of the polystyrene than the PS-2 film. The contradiction between the contact angle and the defects rate may be due to the fact that the contact angle characterizes wetting in macroscopic scale but does not reflect the heterogeneity of the wetting layer in nanometer scale. The heterogeneity may affect the defect rate. I need to characterize such a heterogeneity of the wetting layer to resolve the contradiction in future work.

2.3.6 Microdomain Structures of PS-*b*-PMMA on Chemically Prepatterned Substrates with $d_S \approx 2d_0$.

So far I have demonstrated the conditions under which the self-assembled microdomain structure can replicate and correct a chemical pattern in the substrate. In this section, the concept is taken at step further. I demonstrate that the self-assembled microdomain structure can interpolate patterns in which the substrate was chemically prepatterned with $d_S \approx 2d_0$. Figure 2-14 shows the SEM images of (a) PMMA resist pattern with d_S = 64 nm, (b) the microdomain structure of SMMA-1 (d_0 = 32 nm) on the chemically prepatterned substrate with d_S = 64 nm, and (c) the corresponding 2D-FFT image. The film thickness was t_f = 48 nm and PS-2 was used as the PS-grafted chemically prepatterned layer. I found a hexagonal lattice in most of the area in the SEM image but several cylinders oriented parallel to the substrate surface were also observed. 2D-FFT image exhibits a spots-like pattern with several higher order spots, but a halo ring was also observed, reflecting the defects. Therefore, in

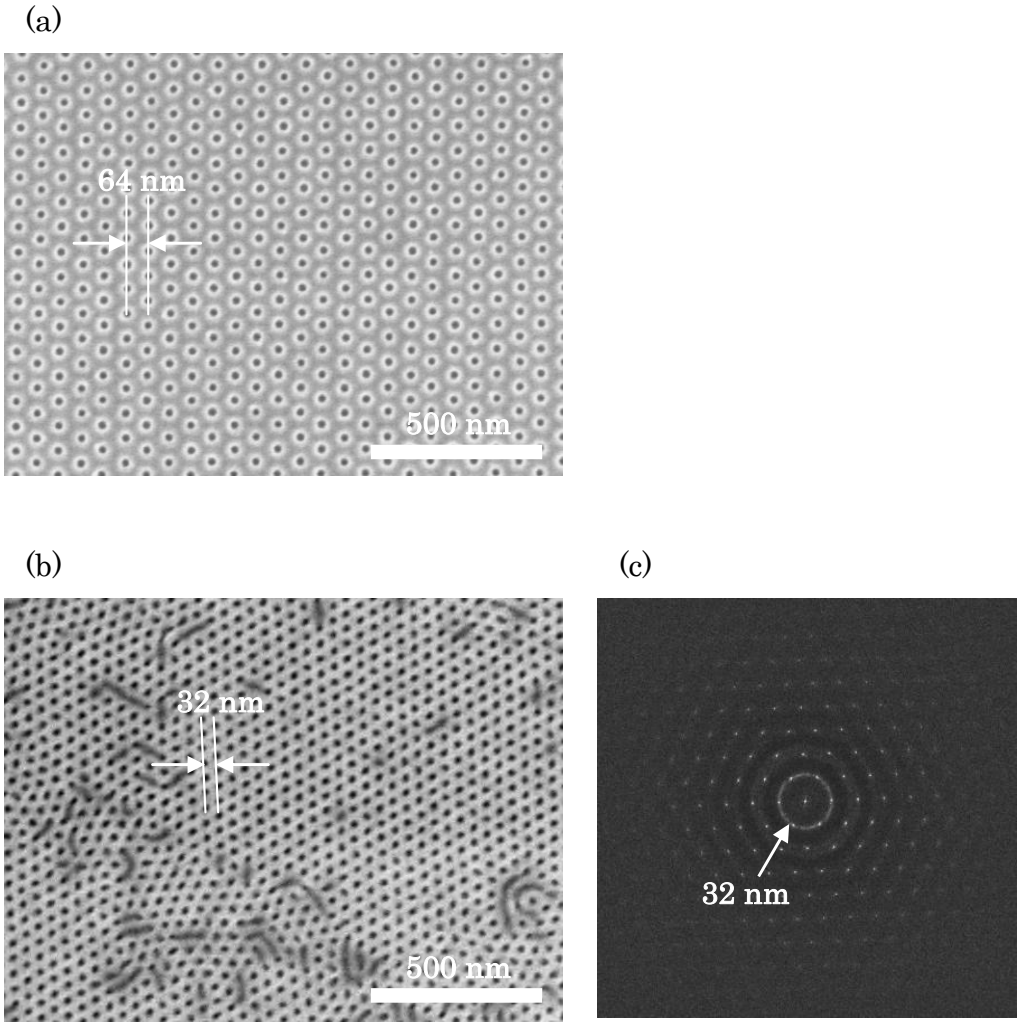

Figure 2-14. (a) SEM image of PMMA resist pattern with d_S = 64 nm, (b) SEM image of the microdomain structure of SMMA-1 on the chemically prepatterned substrate with d_S = 64 nm, and (c) the 2D-FFT image obtained from the SEM image of the microdomain structure.

the case in which d_S = 64 nm = $2d_0$, the microdomain structures were well-directed by the substrate with long-range order but that there were some defects in the microdomain structures.

Figure 2-15 shows the SEM images of the microdomain structures of SMMA-1 (d = 32 nm) on chemically prepatterned substrate with (a) d_S = 61 nm, (b) d_S = 62 nm, and the corresponding 2D-FFT images. Again the thickness of the film was t_f = 48 nm. PS-2 was

used as the PS-grafted layer. In each SEM image, I found several cylinders oriented parallel to the substrate surface, although the most of the SEM imaged regions show hexagonal lattices, suggesting the lack of the long-range order. In the case of d_S = 61 nm, the 2D-FFT image exhibited a hexagonal spot pattern with limited higher order spots, indicating that the grain size of hexagonal lattice was not large. On the other hand, 2D-FFT images for d_S = 62 nm and d_S = 64 nm (Figure 2-14(c)), exhibit halo rings with the spots. The higher order peaks were observed more clearly than those in the 2D-FFT image of d_S= 61 nm. Thus, the grain sizes of the d_S = 62 nm and d_S = 64 nm (Figure 2-14(b)) patterns were larger than that

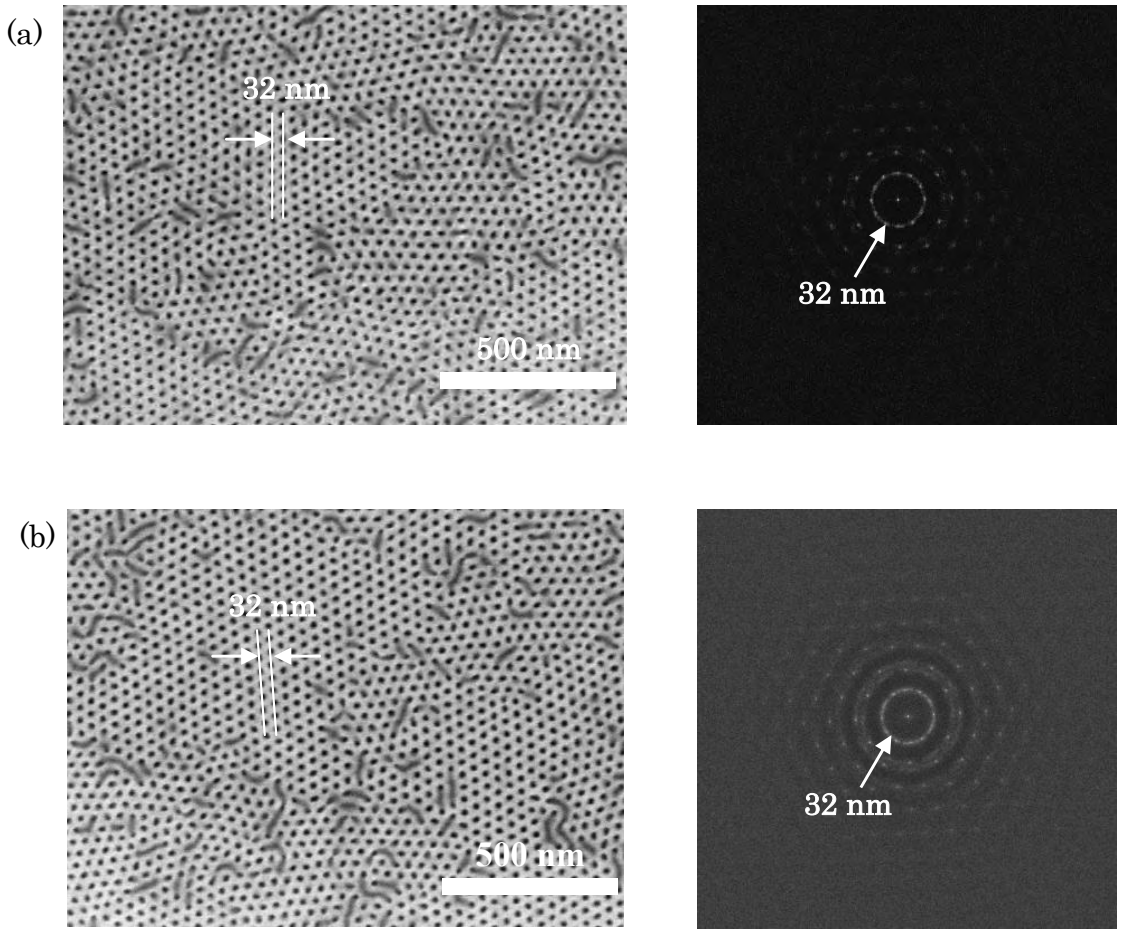

Figure 2-15. SEM images and corresponding 2D-FFT images for selfassembled microdomain structures of SMMA-1 on the chemically prepatterned substrate with (a) d_S = 61 nm, (b) d_S = 62 nm.

for the d_S = 61 nm pattern. The *d*-spacing estimated from all three 2D-FFT images were 32 nm and were independent of d_S. Since the azimuthal angle dependences of the first order peak intensity for d_S = 61 nm, 62 and 64 nm do not have distinct peaks, I can not characterize the distribution.

Figure 2-16 shows the SEM images of (a) PMMA resist pattern with d_S = 48 nm, (b) the microdomain structure of SMMA-2 (d_0 = 24 nm) on the chemically prepatterned substrate with d_S = 48 nm, and (c) the corresponding 2D-FFT image. The film thickness was t_f = 38

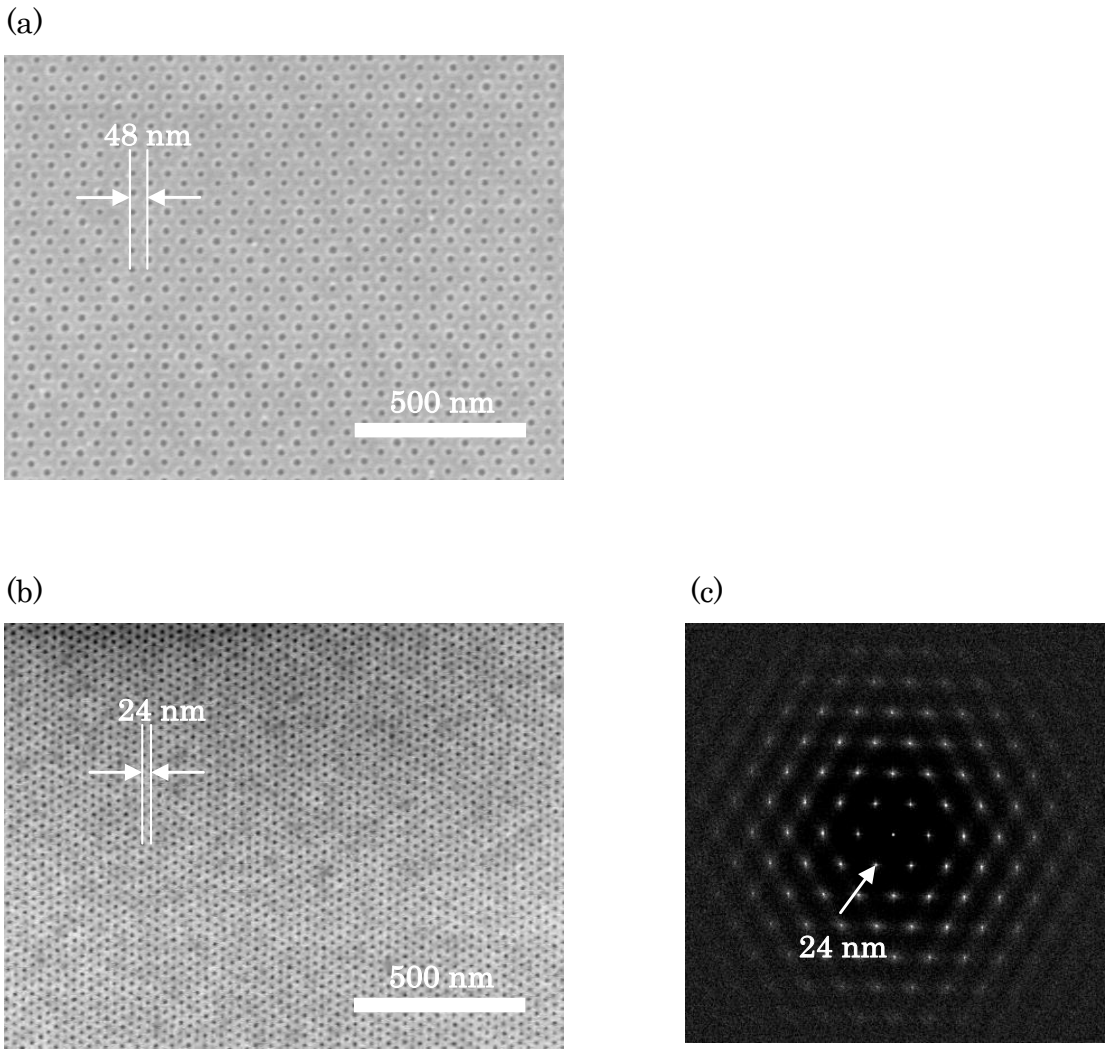

Figure 2-16. (a) SEM image of PMMA resist pattern with d_S = 48 nm, (b) SEM image of the microdomain structure of SMMA-2 on the chemically prepatterned substrate with d_S = 48 nm, and (c) the 2D-FFT image obtained from the SEM image of the microdomain structure.

nm and PS-2 was used for PS-graft layer. In contrast to the results for SMMA-1 described above, I obtained defect-free and single-crystal-like microdomain structure on the substrate. The corresponding 2D-FFT images exhibit spot-like patterns aligned to the chemical patterns with higher-order peaks. This result indicates that the self-assembling of PS-*b*-PMMA can well interpolate the chemical patterns formed with EB lithography process. As already mentioned above, Ruiz et al. recently reported that the interpolation by the selfassembling of PS-*b*-PMMA can be done successfully on the chemical patterns formed with an EB lithography process.[34] Both results clearly show that directed self-assemble of BCPs can duplicate the density of nanopatterns.

Figure 2-17 shows the SEM images of the microdomain structures of SMMA-2 on a chemically prepatterned substrate with (a) d_S = 47 nm, and (b) d_S = 50 nm, and the corresponding 2D-FFT images. The thickness of the film was t_f = 38 nm and PS-2 was used. In the case of d_S = 47 nm, the SEM image did not exhibit large defects but the orientation of hexagonal lattices was slightly distorted. The 2D-FFT image did not show higher-order peaks. The estimated *d*-spacing from the 2D-FFT image was 24 nm in agreement with d_0 = 24 nm, which was slightly larger than half of 47 nm. If the microdomain structure was constrained by the chemically prepatterned substrate, a *d*-spacing of 23.5 nm would be expected.

In the cases of d_S = 50 nm and d_S = 48 nm, single hexagonal lattices were formed in the microdomain structures as shown in the SEM images of Figures 16(b) and 17(b). The corresponding 2D-FFT images exhibited spot-like patterns in the orientation aligned to that of the chemical patterns with higher-order peaks. These results show that self-assembling of PS-*b*-PMMA can interpolate between lattice points in the substrate template, even when a slight mismatch is present, when $d_S > 2d_0$.

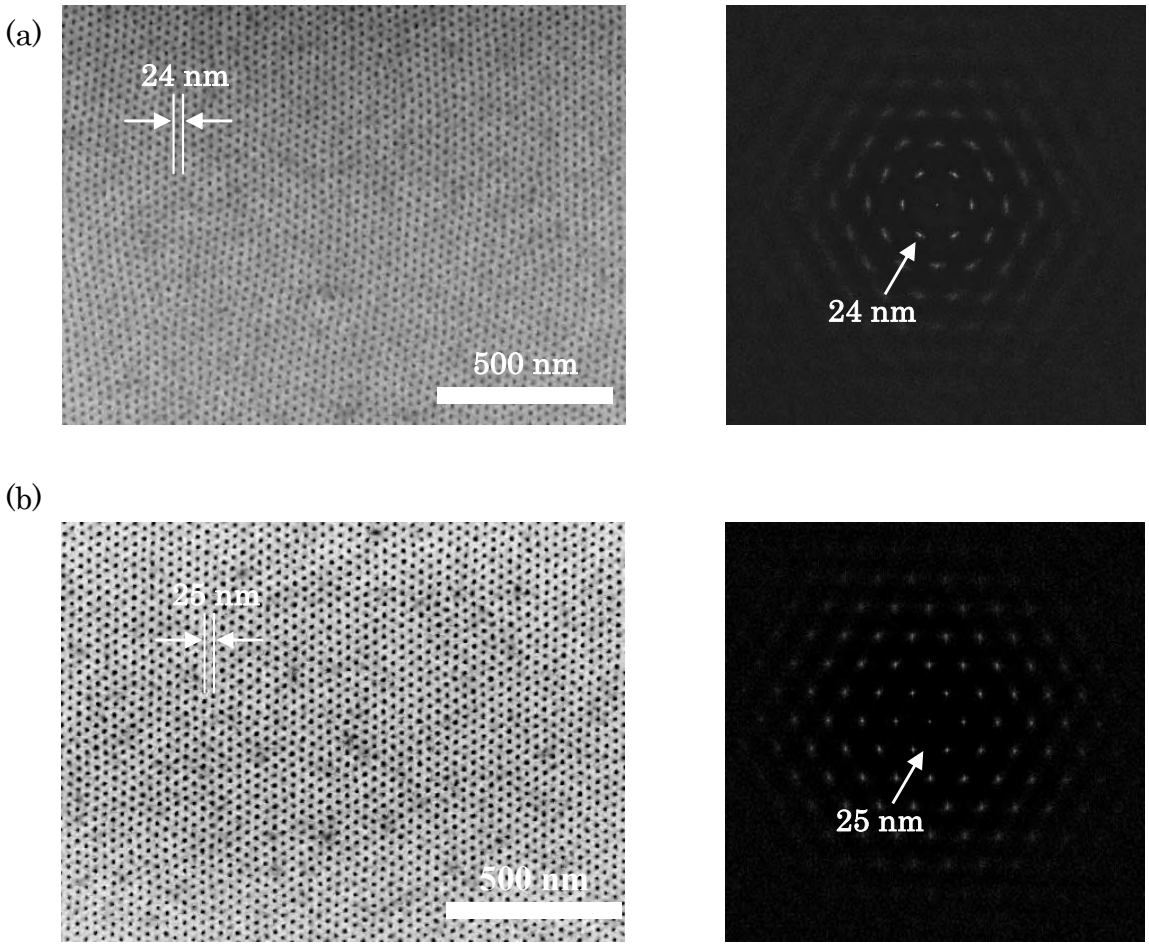

Figure 2-17. SEM images and corresponding 2D-FFT images for self-assembled microdomain structures of SMMA-2 on the chemically preatterned substrate with (a) d_S = 47 nm, and (b) d_S = 50 nm.

I investigated the azimuthal dependence of the first peak intensity in 2D-FFT image shown in Figures 2-16 and 2-17. The width w obtained by fitting the peaks at 180° with Gaussian function are 4.9°, 3.0° and 3.1° for d_S = 47 nm, 48 nm, and 50 nm, respectively.

The interesting point is that the interpolation can be done successfully when $d_S > 2d_0$, while the self-assembly can not interpolate the patterns of the substrate when d_S is slightly smaller than $2d_0$. A similar amount of conformational entropy loss is expected from compression, for $d_S < 2d_0$, as from extension, for $d_S > 2d_0$ in PS chains. However, the

extension of polymer chains causes increased surface contact area between PS chains and the PS-graft layer, which should result in a further decrease in the interfacial energy. A compression would have the opposite effect, to the extension, with less surface area of the PS-grafted layer exposed to the polystyrene and an increase in surface energy. Therefore I would not expect interpolation to work at $d_S < d_0$ or when d_S is slightly smaller than $2d_0$.

To estimate the accuracy of the hexagonal lattice quantitatively, I calculated the *d*-spacing and the standard deviation for the microdomain structure of the SMMA-2 on the patterns with d_S = 48 nm and compared them with the substrate patterns formed with EB lithography and the results of the self-assembled patterns for $d_S = d_0$. The results are summarized in Table 2-4. The *d*-spacing of the microdomain structure was almost half of the *d*-spacing of the pattern and agreed with the *d*-spacing of the microdomain structure for 1:1 correspondence. The results indicate that self-assembly interpolated the pattern of the substrate. The standard deviation of the interpolated pattern was slightly worse than that of the $2d_0$ patterned substrate but was identical to that of the microdomain structure on the $d_S \approx d_0$ patterned substrate. This indicates that the regularity of lattice structure is controlled by the self-assembled microdomains and that self-assembly is a viable process to quadruple lithographic pattern density resolution.

As described above, the interpolation in 1:2 correspondence can successfully performed for d_0 = 24 nm but can not be done well for d_0 = 32 nm. The following discussion could explain the difference between d_0 = 24 nm and d_0 = 32 nm: For the interpolation, the PMMA cylinders at the interpolation points have to stand perpendicular to the substrate on PS-graft layer. If the segregation between PMMA cylinders and PS-graft layers is strong, the cylinders can not stand perpendicular to the substrate on the PS-graft layer. The segregation strength is usually quantified by χN, which depends on the Flory-Huggins interaction parameter per monomer χ, and degree of polymerization N. Since the molecular weight of PMMA in SMMA-1 is larger than that in SMMA-2, the segregation between PMMA chains

and PS-graft layer for SMMA-1 is stronger than that of SMMA-2. Thus the stability of PMMA cylinders oriented perpendicular to the substrate for d_0 = 32 nm will be worse compared to that for d_0 = 24 nm. Since density multiplication is most applicable to the densest of patterns the effect of molecular weight on the ability to interpolate is favorable to lithographic applications.

2.3.7 Effects of the Film Thickness on the Orientation of the Microdomain Structure on the Chemically Prepatterned Substrate with $d_S \approx 2d_0$.

In the previous section, I proved that the self-assembling process of the diBCP can interpolate the chemically prepatterned lattice points so that a single crystal-like lattice can be formed on the chemically prepatterned substrate with $d_S \approx 2d_0$ and thus multiply the pattern density. Here I examine the effects of film thickness t_f on the orientation of the microdomain structures for $d_S \approx 2d_0$.

Figure 2-18 shows effects of film thickness, t_f, on the orientation of the microdomain structures of SMMA-1 (d_0 = 32 nm) on the substrate with d_S = 64 nm. In the case where the film thickness was t_f = 32 nm, which is almost equal to d_0, the interpolation was not observed in most of the area. PMMA cylinders were registered on the chemically prepatterned lattice points with their orientation perpendicular to the substrate, but PS formed hexagonal shaped domains surrounded by the PMMA continuous phase in between the lattice points. On the other hand, when film thickness was adjusted to t_f = 48 nm, which is almost equal to $(3/2)d_0$, the PMMA cylinders stand perpendicular to the surface of the substrate in between the chemically prepatterned lattice points as well as on the lattice points, and the interpolation by the self-assembling of PS-*b*-PMMA can be observed over most of the area in the SEM image (Figure 2-14(b)). Interpretation of structure observed for t_f = 32 nm and influence of film thickness on the interpolation are discussed below.

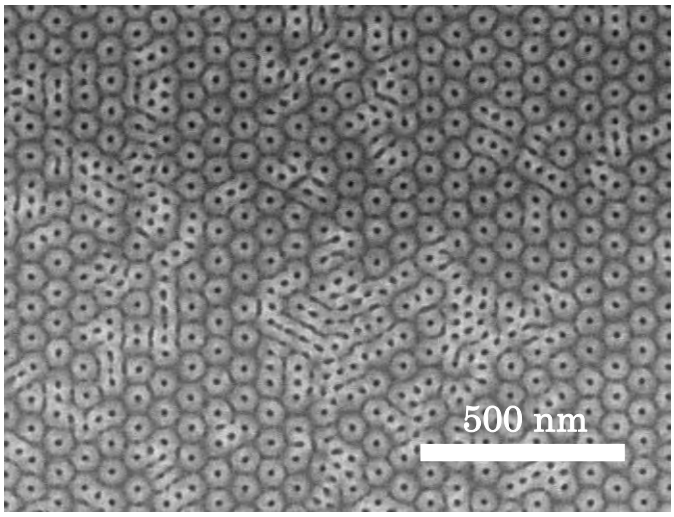

Figure 2-18. SEM images of the microdomain structures of SMMA-1 on the Chemically-Patterned substrate with d_S = 62 nm and the film thickness of 32 nm.

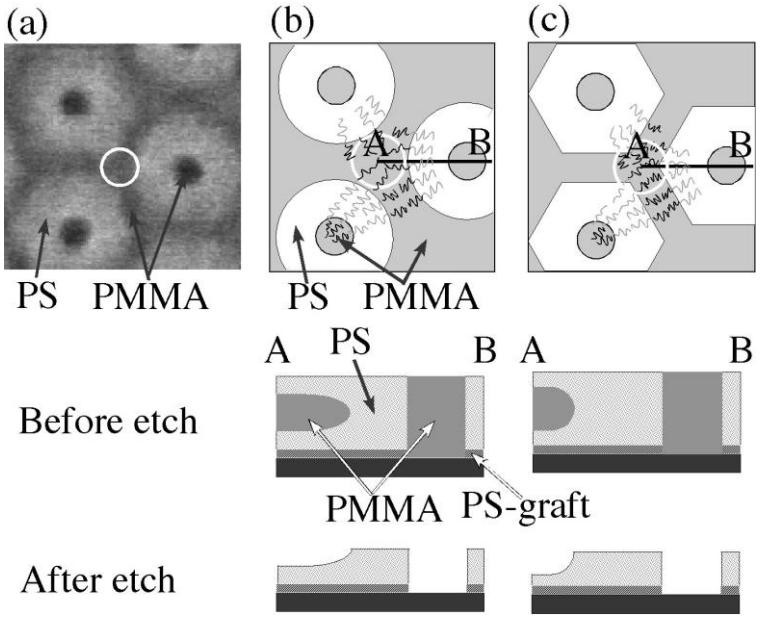

Figure 2-19. (a) Enlarged SEM images of hexagonal structure of PS domains. (b) Chain packing model for circular PS domain surrounding the perpendicularly oriented cylinder on the chemical lattice point, and cross sections of the thin film along A to B before and after etch for SEM observation. (c) Chain packing model for hexagonal PS domain surrounding the perpendicularly oriented cylinder on the chemical lattice point, and cross sections of the thin film along A to B before and after etch for SEM observation. White circles in parts a-c correspond to junction regions of the PMMA continuous phase, where PMMA domains connected each other.

When t_f = 32 nm, the PMMA domains on chemically prepatterned lattice points (which appear as black dots in Figure 2-18), were surrounded by lighter PS domains as mentioned above. The shape of surrounding PS domains were mainly hexagonal as can be clearly seen in the enlarged SEM image presented in Figure 2-19(a). Between the PS domains, PMMA formed a continuous phase, which appeared as a gray phase in Figure 2-18 and Figure 2-19(a). I can speculate the origin of this hexagonal structure as follows: The PS-*b*-PMMAs used in this study forms PMMA cylinders in PS matrix as their equilibrium structure in bulk state, and they tend to form cylindrical microdomains rather than lamellae or plate-like structures even in thin films. PS chains of PS-*b*-PMMA tend to preferentially wet the PS-graft layer. PS chains are also favored at the free surface.[36,21] Therefore, in the region between the chemically prepatterned lattice points, the PMMA forms a continuous phase in between two PS layers, one facing the free surface and one facing the PS graft layer, as presented in the schematic cross section in Figure 2-20(a). If the PS domains surrounding the vertical PMMA cylinders were to form concentric cylinders as shown in Figure 2-19(b), the PMMA junctions in the continuous phase region (indicated by gray in Figure 2-19(b)) would becomes platelet shape at the junctions of the PMMA cylinders. This shape would cause a loss of the conformational entropy of PMMA chains. If the PS domains form hexagons as shown in Figure 2-19(c), the PMMA at the junction region in the continuous phase region can form a structure closer to cylinders. In this case, the loss of conformational entropy of joining PMMA chains would be less than the case where joining PMMA chains form platelets. Although PS chains looses the conformational entropy in this case by expanding the PS domains to form hexagons, the enthalpic term due to the decrease in the contact area between PS chains and PMMA chains can compensate the loss of the entropy. Also the PS would be in contact with both surfaces and lower the surface energy. To confirm the discussion on the effects of the thickness on the orientation of the microdomains as described above, I need to investigate the cross sectional images of the samples. The investigation remains as a future

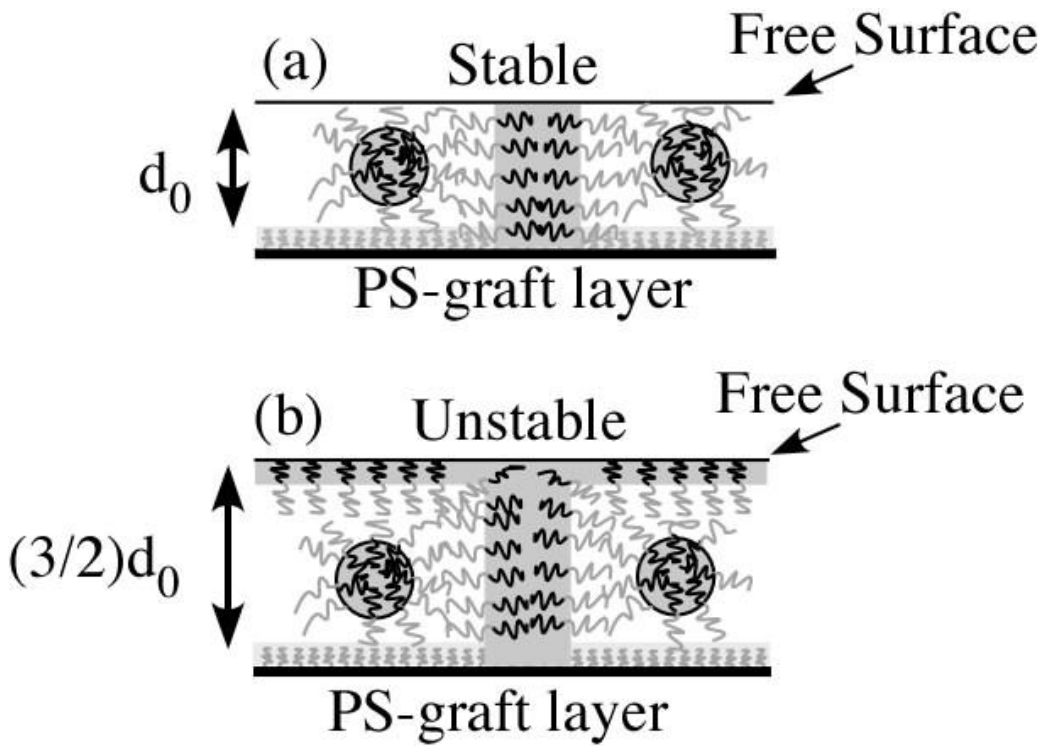

Figure 2-20. Schematic illustration of chains of PS and PMMA for (a) $t_i = d_0$ and (b) $t_i = (3/2)d_0$. The substrate is a PS-graft layer.

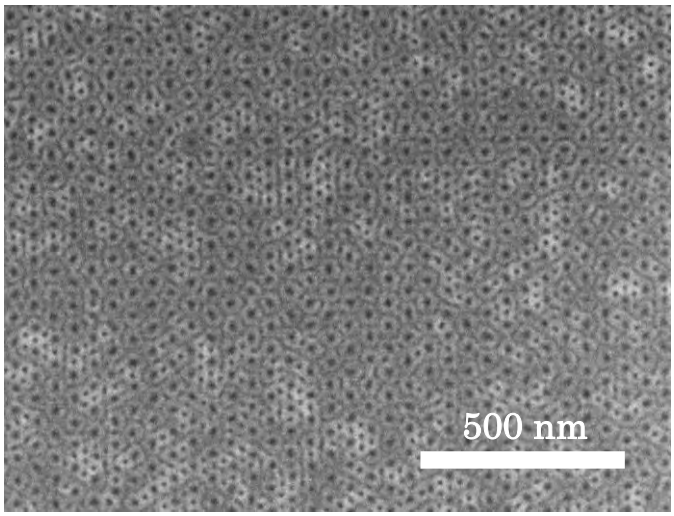

Figure 2-21. SEM images of the microdomain structures of SMMA-2 on the chemically prepatterned substrate with $d_S = 48$ nm and the film thickness of 25 nm.

work. In the case of the thicker BCP film, t_f = 48 nm = (3/2)d_0, the PMMA cylinders stand perpendicular to the PS-grafted surface of the substrate and successfully the interpolate the points between the chemically prepatterned lattice points. This is also driven by surface chemistry as shown in Figure 2-20. In the thicker film case, shown in Figure 2-20(b), if the cylinders were oriented parallel to the substrate surface, sterical filling of the film thickness would bring the PMMA chains in contact with the free surface. This situation is energetically unfavored.[36,21] The contact area between the two surfaces and the PMMA cylinders is minimized if the PMMA cylinders are perpendicular to the surface. Thus, the PMMA cylinders tend to orient perpendicular to the substrate surface and interpolate the chemical pattern. If on the other hand, t_f is equal to d_0, as in Figure 2-20(a), the PMMA cylinders can orient parallel to the substrate with the PS contacting both surfaces.

A similar tendency was observed for SMMA-2 as shown in Figure 2-21. In the case when the film thickness was t_f = 25 nm, which is equal to d_0 of SMMA-2 (Figure 2-17), the interpolation was not observed in all regions and PMMA domains on substrate template were surrounded by hexagonal PS domains. The PMMA formed a continuous phase between the PS domains as observed with SMMA-1 with t_f = 32 nm. In the case for t_f = 38 nm, which is equal to (3/2)d_0, the single crystal-like hexagonal lattice was completed by the interpolation as shown in Figure 2-16(b). The enhancement of the interpolation is caused by the minimization of the surface energy for perpendicular PMMA cylinders, as in the case of SMMA-1 with t_f = 48 nm. The results show that the perpendicular orientation of the PMMA cylinders in substrate surface pattern interpolation is strongly controlled by the film thickness.

2.4 Conclusion

I have investigated how the chemically prepatterned substrate affects the microdomain structure of BCPs on the substrate. First, I characterized the EB patterned substrate and found the imperfection in patterns increases with decreasing *d*-spacing. I investigated the microdomain structure of PS-*b*-PMMA, on the chemically prepatterned substrate with *d*-spacing of the pattern being nearly equal to the intrinsic *d*-spacing of the PS-*b*-PMMA. The epitaxially grown cylinder structures are well aligned in a defect-free hexagonal lattice, although the chemically prepatterned substrate pattern has defects. Self-assembly of PS-*b*-PMMA can repair the pattern defects of the patterned substrate. At the same time, the chemically prepatterned substrate forms a template to align the orientation of the domain structures of BCP into a long-range ordered single crystal structure not achievable by self-assembly alone. I have also investigated the effects of the molecular weight of PS-OH of the patterns and found PS-2 having M_n = 3,700 is most suitable for making defect-free microdomain structures. I successfully demonstrated that self-assembly of the PS-*b*-PMMA can interpolate points in between the chemical lattice pattern generated by EB lithography, thus multiplying the pattern density. I have found that the diBCP film thickness plays an important role on the ability of the microdomains to interpolate the lithographic pattern.

The combined process of nanolithography and self-assembly of diBCPs provides a promising fabrication method for extension of top down-type lithographic capabilities to very high densities.

2.5 References

1. Smith, B. W.; Bourov, A.; Kang, H.; Cropanese, F.; Fan, Y.; Lafferty, N.; Zavyalova, L. *Proc. SPIE* **2004**, *273*, 5377.
2. Terris, B. D.; Thomson, T. *J. Phys. D: Appl. Phys.* **2005**, *38*, R199.
3. Muray, A.; Scheinfein, M.; Isaacson, M.; Adesida, I. *J. Vac. Sci. Technol.* **1985**, *B3*, 367.
4. Yasin, S.; Hasko, D. G.; Ahmed, H. *Microelectron. Eng.* **2002**, *61-62*, 754.
5. Yang, X. M.; Xiao, S.; Wu, W.; Xu, Y.; Lee, K.; Kuo, D.; Weller, D. *J. Vac. Sci. Technol.* **2007**, *B25*, 2202.
6. Park, C.; Yoon, J.; Thomas, E. L. *Polymer* **2003**, *44*, 6725.
7. Hamley, I. W. *Angew. Chem., Int. Ed.* **2003**, *42*, 1692.
8. Segalman, R. A. *Mater. Sci. Eng. Res.* **2005**, *48*, 191.
9. Hawker, C. J.; Russell, T. P. *MRS Bull.* **2005**, *30*, 952.
10. Stoykovich, M. P.; Nealey, P. F. *Mater. Today* **2006**, *9*, 20.
11. Khandpur, A. K.; Forster, S.; Bates, F. S.; Hamley, I. W.; Ryan, A. J.; Bras, W.; Almdal, K.; Mortensen, K. *Macromolecules* **1995**, *28*, 8796.
12. Bate, F. S.; Fredrickson, G. H. *Annu. Re*V. *Phys. Chem.* **1990**, *41*, 525.
13. Hashimoto, T., In *Thermoplastic Elastmers*; Legge, N. R., Holden, G., Schroeder, H. E., Eds.; Hanser: Vienna, 1996.
14. Matsen, M. W.; Schick, M. *Phys. Re*V. *Lett.* **1994**, *72*, 2660.
15. Takenaka, M.; Wakada, T.; Akasaka, S.; Nishitsuji, S.; Saijo, K.; Shimizu, H.; Kim, M. I.; Hasegawa, H. *Macromolecules* **2007**, *40*, 4399.
16. Black, C. T.; Guarini, K. W.; Milkove, K. R.; Baker, S. M.; Russell, T. P.; Tuominen, M. T. *Appl. Phys. Lett.* **2001**, *79*, 409.
17. Segalman, R. A.; Yokoyama, H.; Kramer, E. J. *Ad*V. *Mater.* **2001**, *13*, 1152.
18. Sundrani, D.; Sibener, S. J. *Macromolecules* **2002**, *35*, 8531.
19. Cheng, J. Y.; Mayes, A. M. *Nat. Mater.* **2004**, *3*, 823.

20. Xiao, S. G.; Yang, X. M.; Edwards, E. W.; La, Y. H.; Nealey, P. F. *Nanotechnology* **2005**, *16*, S324.

21. Chen, F.; Akasaka, S.; Inoue, T.; Takenaka, M.; Hasegawa, H.; Yoshida, H. *Macromol. Rapid Commun.* **2007**, *28*, 2137.

22. Angelescu, D. E.; Waller, J. H.; Adamson, D. H.; Deshpande, P.; Chou, S. Y.; Register, R. A.; Chaikin, P. M. *Ad*V. *Mater.* **2004**, *16*, 1736.

23. Thurn-Albrecht, T.; Scotter, J.; Kastle, G. A.; Emley, N.; Shibauchi, T.; Krusin-Elbaum, L.; Guarini, K.; Black, C. T.; Tuominen, M. T.; Russell, T. P. *Science* **2000**, *290*, 2126.

24. Mansky, P.; DeRouchey, J.; Russell, T. P.; Mays, J.; Pitsikalis, M.; Morkved, T.; Jaeger, H. *Macromolecules* **1998**, *31*, 4399.

25. Mansky, P.; Liu, Y.; Huang, E.; Russell, T. P.; Hawker, C. *Science* **1997**, *275*, 1458.

26. Morkved, T. L.; Lu, M.; Urbas, A. M.; Ehrichs, E. E.; Jaeger, H. M.; Mansky, P.; Russell, T. P. *Science* **1996**, *273*, 931.

27. Xu, T.; Zvelindovsky, A. V.; Sevink, G. J. A.; Lyakhova, K. S.; Jinnai, H.; Russell, T. P. *Macromolecules* **2005**, *38*, 10788.

28. Kim, S. H.; Misner, M. J.; Russell, T. P. *Ad*V. *Mater.* **2004**, *16*, 2119.

29. Kim, S. H.; Misner, M. J.; Xu, T.; Kimura, M.; Russell, T. P. *Adv. Mater.* **2004**, *16*, 226.

30. Rockford, L.; Liu, Y.; Mansky, P.; Russell, T. P.; Yoon, M.; Mochrie, S. G. J. *Phys. Re*V. *Lett.* **1999**, *82*, 2602.

31. Kim, S. O.; Solak, H. H.; Stoykovich, M. P.; Ferrier, N. J.; dePablo, J. J.; Nealey, P. F. *Nature* **2003**, *424*, 411.

32. Edwards, E. W.; Stoykovich, M. P.; Solak, H. H.; Nealey, P. F. *Macromolecules* **2006**, *39*, 3598.

33. Welander, A. M.; Kang, H.; Stuen, K. O.; Solak, H. H.; Mu¨ller, M.; de Pablo, J. J.; Nealey, P. F. *Macromolecules* **2008**, *41*, 2759.

34. Ruiz, R.; Kang, H.; Detcheverry, F. A.; Dobisz, E.; Kercher, D. S.; Alberecht, T. R.; de

Pablo, J. J.; Nealey, P. F. *Science* **2008**, *321*, 936.

35. Cheng, J. Y.; Rettner, C. T.; Snaders, D. P.; Kim, H. C.; Hinsberg, W. D. *Adv. Mater.* **2008**, *20*, 3155.

36. Russell, T. P.; Coulon, G.; Deline, V. R.; Miller, D. C. *Macromolecules* **1989**, *22*, 4600.

CHAPTER3 NINE-FOLD DENSITY MULTIPLICATION OF HCP LATTICE PATTERN BY DIRECTED SELF-ASSEMBLY OF BLOCK COPOLYMER

3.1 Introduction

Demand forever smaller critical dimensions in the semiconductor and storage industries continue pressing conventional photolithography beyond the diffraction limit. Scientific and technological challenges arise as resolution requirements approach molecular length scales and the economics of new lithographic technologies become prohibitively expensive.[1,2] While electron beam (EB) lithography can routinely produce features in the 15–25 nm range (and even down to 2–5 nm [3–5] under special conditions), the application is often limited by low feature densities and low throughput. In this context, self-assembling structures at the nanometer scale have emerged as a way to overcome current lithographic resolution limitations.[6–10] In particular, block copolymer (BCP) directed assembly with a high density multiplication factor stands out as a promising alternative to overcome EB lithographic resolution and throughput limitations.

BCPs exhibit a wide variety of periodic nanodomain structures, such as parallel-oriented lamellar, hexagonallypacked cylinder, and a body centered lattice of spheres.[11–15] BCP thin films deposited onto substrate surfaces, can be utilized as resist patterns that can be transferred into a variety of substrates. Methods, such as graphoepitaxy[16–21] and chemical registration[22–27] have been proposed to precisely control the domain morphology and its orientation to obtain patterns with precision required for lithographic applications. The effect of a chemically-patterned surface template on the orientation of microphase separated diBCP was first reported by Rockford et al.[22] Nealey et al.

have shown directed lamellar-[23] and cylinder-[24,25] microdomains of poly(styrene-*block*-methyl methacrylate) (PS-*b*-PMMA) in registration with the lithographically defined patterns in chemically modified surfaces with a one-to-one correspondence. Recently, Ruiz et al.[26] and Tada et al.[27] successfully demonstrated that areal density of chemical templates can be multiplied by a factor of 4 in hexagonal array patterns. The vertical cylinders filled lattice points halfway between the lattice points on the template pattern. Cheng et al. showed a similar template pattern interpolation for line arrays applying lamella-forming PS-*b*-PMMA[28]. The combination of chemical registration and self-assembly of BCP would enable us to attain higher density multiplication.

In this chapter, I demonstrate a nine-fold feature density multiplication by directed BCP assembly. I clarify the tolerance ranges for nine nine-fold feature density multiplication in terms of film thickness and lattice mismatch and compare the tolerance ranges with those for the four-fold feature density multiplication. I also show that the critical dimension formed by the BCP domains is independent of that defined by the EB pre-patterned features.

3.2 Experimental Section

Figure 3-1 illustrates the density multiplication process. I first prepared hexagonal array of dots on Si substrates by chemical patterning and then the density multiplication was attained by directed self-assemble of BCP in thin film.

3.2.1 Materials.

PS-*b*-PMMA and hydroxy-terminated polystyrene (PS–OH) were purchased from Polymer Source Inc., Quebec, Canada. The weight averaged molecular weight and weight fraction of its PS block were 4.8×10^4 and 0.75, respectively. The weight averaged molecular weight of PS–OH was 3.7×10^3.

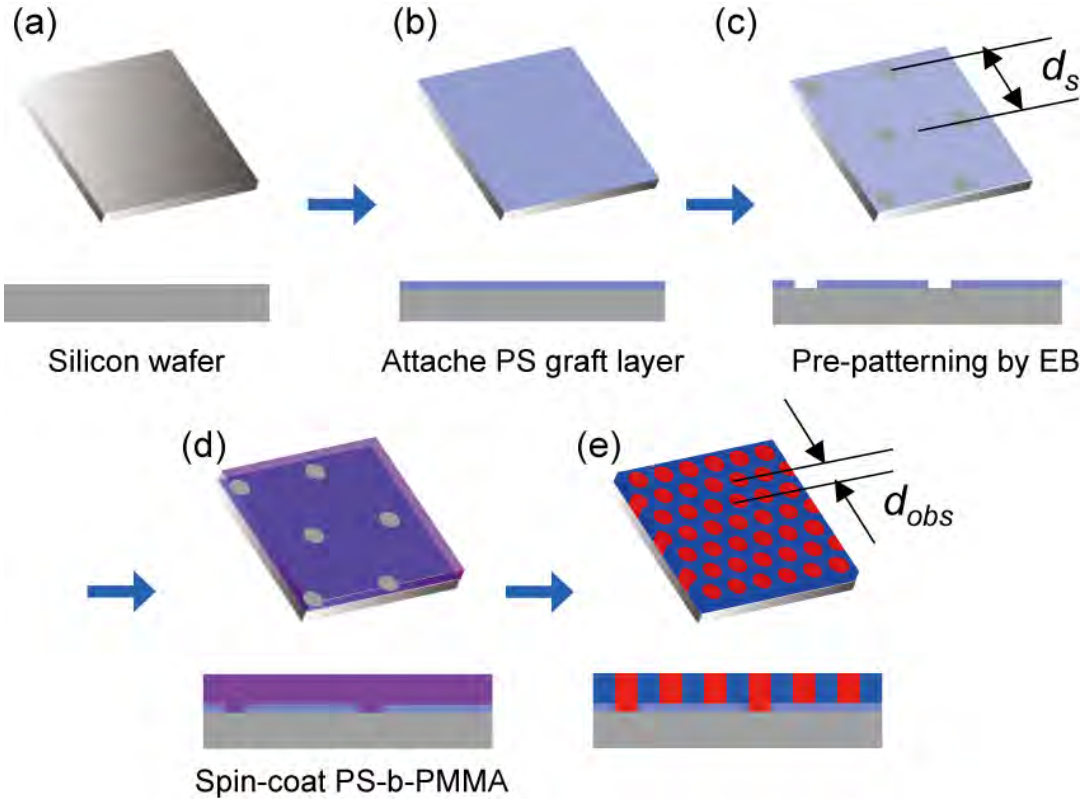

Figure 3-1. Schematically illustrated density multiplication process with chemically pre-patterned template.

3.2.2 Substrate preparation.

Si substrate surfaces were chemically-patterned in the following manner. First the Si substrate was cleaned in a piranha solution at 80°C for 15 min and rinsed in deionized water. Next, a 1.0 wt% PS–OH solution in toluene was spin-coated onto the Si substrate to a thickness of about 50 nm. The grafting of PS on the Si substrate was completed by annealing the PS–OH-coated Si wafer in vacuum at 140°C for 48 h. Unreacted PS–OH was removed by rinsing the substrate with toluene. The thickness of PS grafted layer was determined by X-ray reflectometry to be 5.1 nm. Next, the PS grafted layer was patterned by EB lithography. PMMA resist was spin-coated onto the PS-grafted Si substrate to thicknesses of 50 nm. The samples were exposed by electron beam in hexagonal arrays of dots and developed. Since the dots were exposed by EB, development removed only the dots in the PMMA. Lattice

spacings of hexagonal arrays of dots used in this study were slightly around $d_S = 3d_0$, where d_S is the spacing between lattice planes defined by EB on the substrate and d_0 is the corresponding natural spacing of the BCP in the bulk, as shown in Figure. 3-1. The samples were subsequently etched by O_2 reactive etching technique (RIE) using a SAMCO RIE-10NR etcher operated at the plasma power of 100W. The etching time was short, 5 s, so that the PMMA mask remained and only the grafted PS in the holeswas selectively reacted with the plasma. The PMMA mask was removed by rinsing the substrate with *N*-methyl-2-Pyrolidone and/or toluene, leaving a chemicallypatterned substrate. The treated areas on the substrate have a higher affinity for PMMA while the PS-grafted surface has a weak preferential affinity for PS.

3.2.3 Sample preparation.

Thin films of PS-*b*-PMMA were spin-coated from a dilute solution in toluene. The thickness of the films was controlled by the concentration of the solutions and the spin speed. Spin-coated samples were then annealed at 170°C for 12 h in vacuum to reach their equilibrium state. Thicknesses of the PS-*b*-PMMA films t_f were determined by subtracting the thickness of the PS-graft layer from the total thickness of the organic film composed of PS-grafted layer and PS-*b*-PMMA layer on the Si substrates. The total thickness of the organic film was measured by removing a portion of the film from the substrate with a sharp knife and measuring the step between the substrate surface and the film surface with a Veeco Nano Scope III atomic force microscope.

3.2.4 Scanning electron microscope observation.

Microdomain structures of PS-*b*-PMMA were observed by using a Hitachi S-4800 field-emission Scanning Electron Microscope (SEM) instrument operated at an acceleration voltage of 0.7 kV. For contrast between the PMMA and PS phases, the BCP specimens were etched by O_2 RIE with a SAMCO RIE-10NR. Since the O_2 RIE preferentially etches

the PMMA structures, the dark and bright parts of SEM images correspond to PMMA and PS microdomains, respectively.

3.3 Results and Discussion

3.3.1 Nine-fold density multiplication.

Figure 3-2a–d shows the results obtained for nine-fold density multiplication, $d_S = 3d_0$. Figure 3-2a shows an SEM micrograph of the EB resist pattern employed to prepare the chemical template with d_S = 72 nm. Figure 3-2b shows a SEM image of PS-*b*-PMMA thin film self-assembled on the pre-patterned chemical template. The film thickness of the PS-*b*-PMMA was optimized to t_f = 38 nm, which nearly corresponds to $(3/2)d_0$ of the PS-*b*-PMMA BCP. The self-assembled filmis well-aligned to the template pattern with long-range order in the lattice. Figure 3-2c is a 2-dimensional fast Fourier transform (2D-FFT) image of Figure 3-2b. Several higher order peaks were observed, with up to 6th order, at $(q/q_m)^2$ = 1, 3, 4, 7, 9, and 12, with q_m being the 1st order peak position of the 2D-FFT image. From 1st to 3rd order peak positions in the circular averaged 2D-FFT image, the lattice spacing of the self-assembled PMMA cylindrical microdomain was determined to be d_{obs} = 24 nm, which was a third of the value of the lattice spacing, d_S = 72 nm, of chemically pre-patterned substrate. Figure 3-2(d) shows a computer generated image in which the SEM image of the EB resist pattern in orange was superimposed with the SEM image of the directed PS-*b*-PMMA self-assembled pattern in green. This image demonstrates that two PMMA cylinders interpolated linearly between lattice points of the pre-patterned template thus multiplying the feature area density by a factor of 9. To clarify the regularity of the microdomain spacing quantitatively, I calculated standard deviation σ of *d* spacing for the microdomain of nine-fold density multiplication and compared the results for nine-fold density multiplication with those for four-fold density multiplication and 1:1 correspondence ($d_S = d_0$) from auto-correlation function[27]. It should be noted that the value

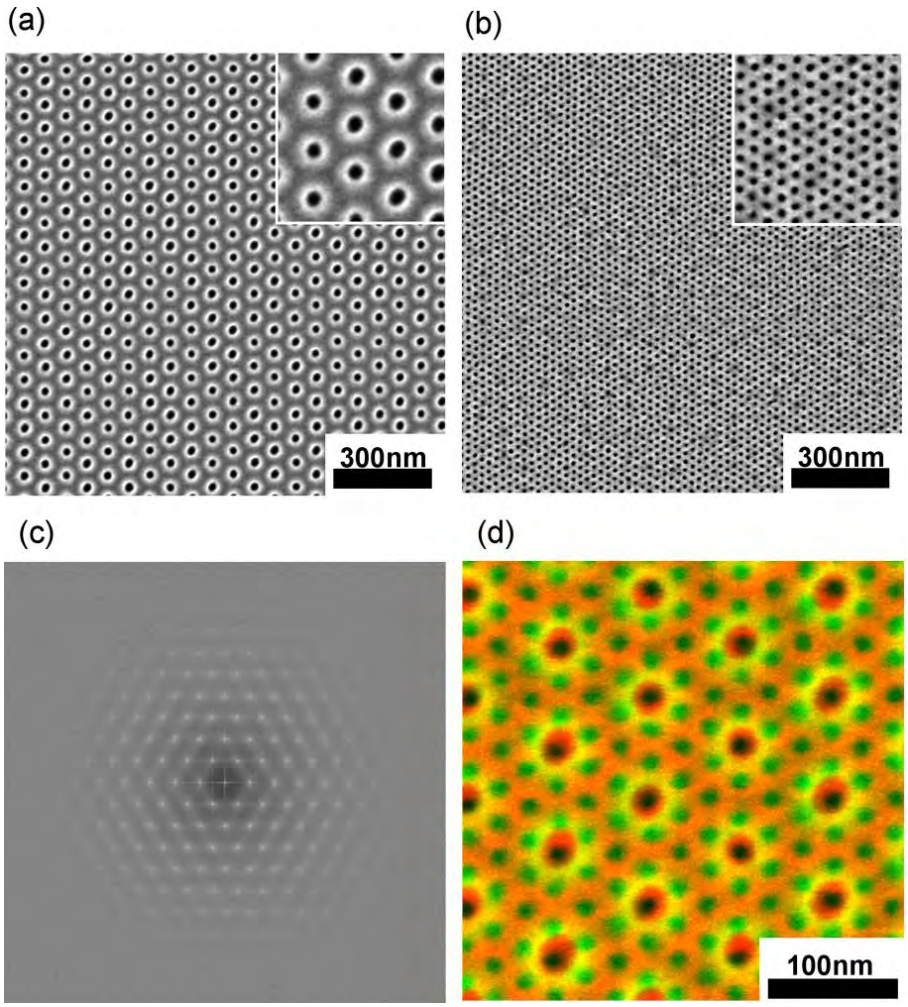

Figure 3-2. (a): Top-view SEM image of EB resist employed to pattern PS graft layer on Si wafer surface for a chemically pre-patterned template with d_S = 72 nm. (b): Top-view SEM image of cylinder structures of PS-*b*-PMMA with d_0 = 24 nm self-assembled on the chemically pre-patterned template. Thickness of PS-*b*-PMMA film t_f = 38 nm. (c): 2D-FFT image of (b) in arbitrary scale. (d): Computer generated image prepared by over laying (a) and (b) in orange and green, respectively.

Table 3-1. *d* and σ for Chemical Prepatterns and Microdomain of PS-*b*-PMMA.

configuration	chemical prepattern		PS-*b*-PMMA self-assembly	
	d (nm)	σ (nm)	*d* (nm)	σ (nm)
1:1 correspondence ($d_s = d_0$)	23.8	5.3	24.1	2.6
4x multiplication ($d_s = 2d_0$)	2.0	2.0	23.8	2.6
9x multiplication ($d_s = 3d_0$)	71.9	2.7	23.8	2.0

of σ estimated from auto-correlation function tends to become larger than that estimated fromreal space analyses though it can express the tendency of the regularity well. The results are shown in Table 3-1. We also displayed the d spacing and standard deviation of chemical patterns for each condition in Table 3-1. As for the results for the microdomain, standard deviation for the nine-fold becomes better than the others, although the degree of interpolation is large. This improvement may originate from the fact that the self-assembling of BCP becomes dominant in the case of the nine-fold while the chemical pattern having worse standard deviation affects the regularity of the microdomain.

Lithographic applications for high fidelity pattern transfer require a perpendicular orientation of the BCP domains. Equilibrium structures of BCP thin films including phase morphology and domain orientation are determined by the various parameters that characterize the free energy of a thin film confined between a pre-patterned surface and a top homogenous surface, including annealing temperature, chain conformation, domain–domain interaction, interfacial energies between the BCP and the pre-patterned substrate and the free surface (which in turn is determined by the vacuum level and gas composition).[29–33] The final equilibrium phase morphology and domain orientation correspond to those that minimize the free energy expression[29,33]:

$$F = F_{\text{elastic}} + F_{\text{S–MMA}} + F_{\text{surface}} + F_{\text{interface}} \qquad (1)$$

where F_{elastic} being the free energy for the chain conformation, $F_{\text{S-MMA}}$ being the free energy for domain–domain interaction, F_{surface} being the free energy for the free surface, and $F_{\text{interface}}$ being the free energy for the interface between chemically-patterned substrate and PS-*b*-PMMA. The range of thickness values and commensurability tolerance to the chemical pre-pattern for which a perpendicular orientation is more favorable depends on the minimization of the expression in Eq. (1). Keeping interface interactions and the annealing temperature constant, simulations[26,30–32] and experiments[27,30,33] have shown that film thickness

and commensurability to d_0 span a parameter space where perpendicular orientation is energetically more favorable.

3.3.2 Effects of thickness of sample on density manipulation.

The effect of t_f on nine-fold density multiplication was studied and the results are shown in Figure 3-3. The substrate surfaces were patterned with the same template as above with $d_S \approx 3d_0 = 72$ nm. Figure 3-3a and b show SEM images of PS-*b*-PMMA thin film self-assembled on the pre-patterned templates with $t_f = 23$ nm $\approx d_0$ and $t_f = 46$ nm $\approx 2d_0$, respectively. In Figure 3-3, it is clear that the film thicknesses corresponding to $t_f \approx d_0$ and $t_f \approx 2d_0$, do not show the long-range order exhibited in Figure 3-2b, $t_f \approx (3/2)d_0$. In Figure 3-3a, where $t_f \approx d_0$, the SEM image shows PMMA cylinders both parallel and perpendicular to the substrate surface. In Figure 3-3b, where $t_f \approx 2d_0$, the PMMA cylinders with perpendicular orientation to the substrate surface, but with a poly-grain structure, were observed. The results suggest that when $t_f = 2d_0$, the chemical template prepattern does not direct the assembly to the top surface.

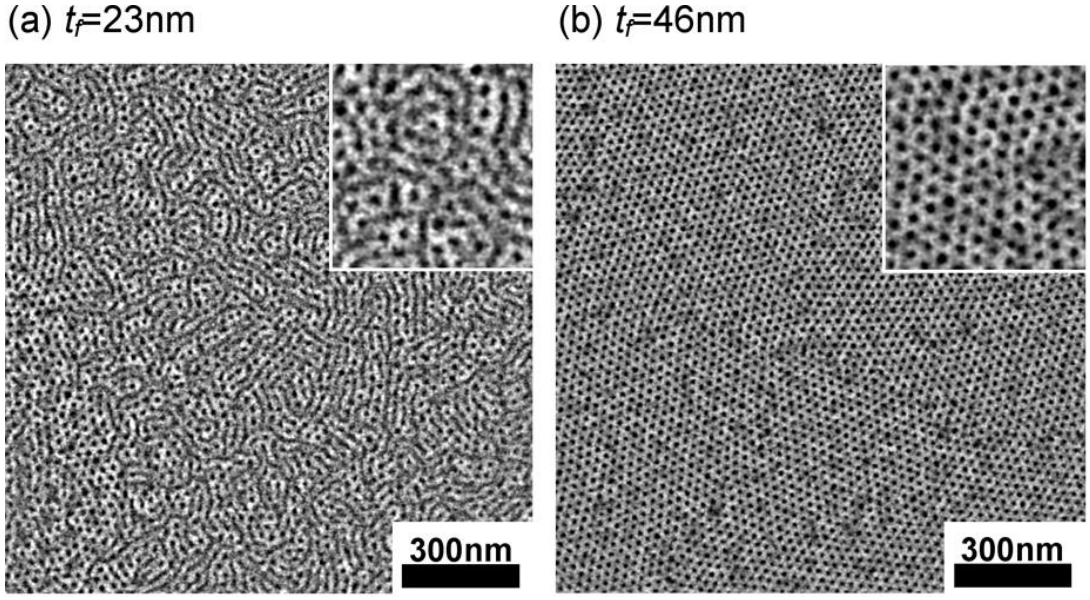

Figure 3-3. Top-view SEM images of cylinder structures of PS-*b*-PMMA with $d_0 = 24$ nm self-assembled on the chemically prepatterned template with $d_S = 72$ nm. Thickness of PS-*b*-PMMA film: (a) $t_f = 23$ nm and (b) $t_f = 46$ nm.

The effect of t_f on the cylinder orientation can be discussed in terms of three controlling factors: the conformational entropy of BCPs (corresponding to Felastic), the interaction between free surface and BCPs (free surface interaction corresponding to $F_{surface}$), and the interaction between substrate and BCPs (substrate interaction corresponding to $F_{interface}$). The conformational entropy tends to align PMMA cylinders perpendicular[34]. Free surface interaction is almost neutral for both PS and PMMA but varies slightly with annealing temperature and vacuum condition applicable for the experiments. Thus, in principle, free surface interaction induces the cylinder to orient perpendicular to the surface but the strength of free surface interaction depends on the annealing condition. The substrate interaction of the chemically patterned substrate causes the perpendicular orientation on the lattice pointswhere PS graft layer is etched. However, as for chemical pattern with $d_S = 3d_0$, wide un-etched region with PS graft layer exist in between the etched lattice points. This region favors PS and induces parallel orientation of the PMMA cylinders. In the case of thin samples with $t_f \leq d_0$, the substrate interaction becomes dominant rather than the conformational entropy and the free surface interaction. Therefore, manyPMMAcylinders are oriented parallel to the surface. On the other hand, as t_f increases, the surface area to volume ratio decreases and the effect of substrate interaction becomes weaker than that for $t_f \leq d_0$. Conversely, the effects of the conformational entropy affect the orientation of PMMA cylinders more strongly. Thus, the perpendicular orientation becomes dominant as t_f increases. However, as the effect to register PMMA cylinders on the pre-patterned lattice points are caused by the substrate interaction, the effect diminishes with increasing t_f. Therefore, orientation of hexagonal lattices cannot be directed for thicker samples.

Consideration above suggests that there exist an optimum t_f range for the PMMA cylinders to align perpendicular to the surface and to be directed to form a hexagonal lattice by the substrate pattern. The optimum thickness for complete 9× interpolation was found to be around $t_f = 1.5d_0$ in the experimental conditions I have employed, and agrees with that for

4× interpolation as shown in our previous report[27]. However, the value may change with annealing condition (temperature, degree of vacuum) and/or molecular weights of BCPs and polymer applied as a graft layer.

3.3.3 Effects of lattice mismatch on 9× density multiplication.

I also investigated the effect of lattice mismatch on the quality of the 9× density multiplication by using chemical prepatterns slightly below and above the commensurability condition ($d_S = 3d_0 = 72$ nm). Figure 3-4 shows SEM micrographs and corresponding 2D-FFT images of the microdomain structure of the PS-*b*-PMMA on chemical templates that are slightly mismatched from $3d_0$, namely $d_S = 70$ nm $= 2.9d_0$ and $d_S = 74$ nm $= 3.1d_0$. The PS-*b*-PMMA copolymer film thickness was the prior determined optimal thickness, $t_f = 38$ nm. As can be seen in Figure 3-4, regularity and long-range order of PS-*b*-PMMA is worse for the mismatched configurations, than the exact template match, in Figure 3-2.

In the case of $d_S = 70$ nm, there are some grains and defects between grains observed in the SEM image (Figure 3-4a-i). 2D-FFT image displayed a halo pattern suggesting a lack of registration with the surface template (Figure 3-4a-ii). On the other hand, although grains and defects between grains can be also observed in the SEM image for $d_S = 74$ nm (Figure 3-4b-i), regularity of the pattern of $d_S = 74$ nm is better than that of $d_S = 70$ nm. The 2D-FFT image (Figure 3-4b-ii) still shows a hexagonal pattern reflecting the single orientation of the domain structure, though the peaks are broader than that of $d_S = 72$ nm (Figure 3-2). The lattice spacing of the domain structure determined from the 2D-FFT image for $d_S = 74$ nm was $d_{obs} = 25$ nm, indicating that the diBCP chains are slightly extended to follow the chemical pattern of the template. The difference in the FFT patterns between $d_S = 70$ nm and $d_S = 74$ nm indicates that compression of the PS-*b*-PMMA chains is energetically unfavored in comparison to the case of stretching. This tendency have been shown for the chemical registration of PS-*b*-PMMA lamella[23] and cylindrical morphologies

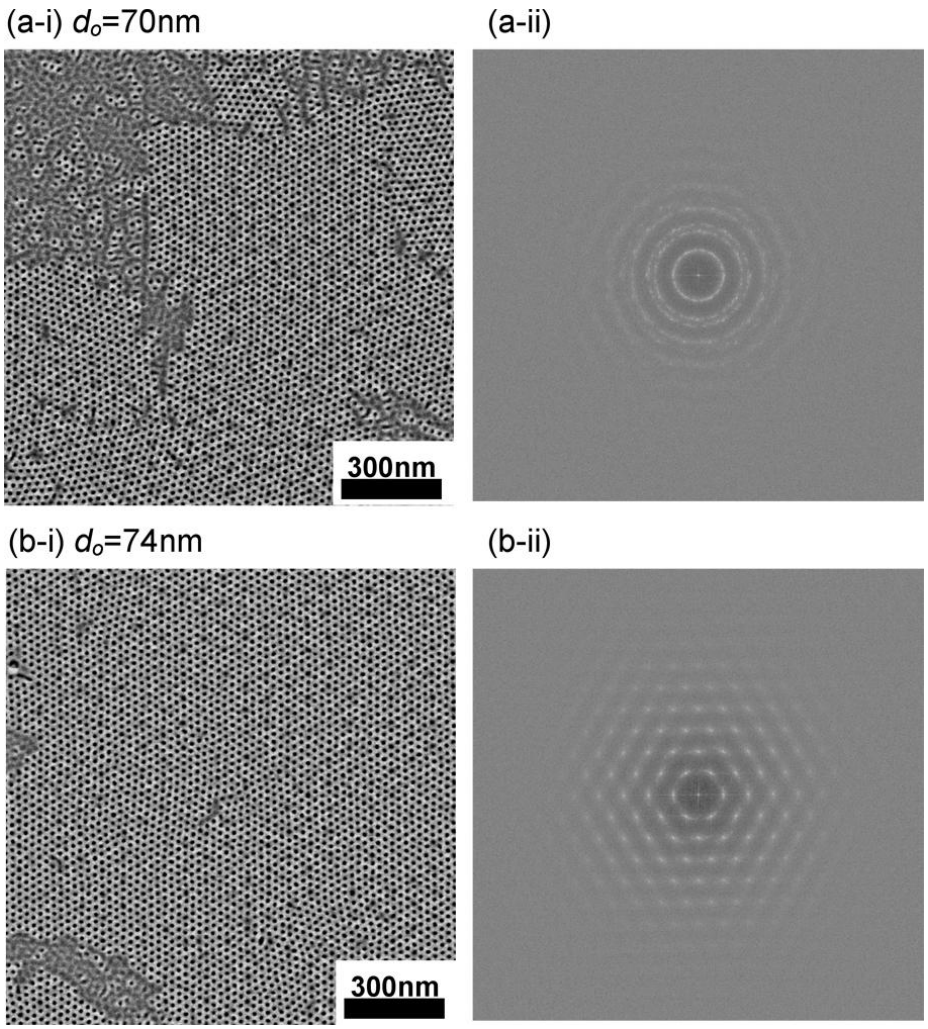

Figure 3-4. Top-view SEM images of cylinder structures of PS-*b*-PMMA with d_0 = 24 nm self-assembled on the chemically pre-patterned template with (a-i) d_S = 70 nm and (b-i) d_S = 74 nm. (a-ii) and (b-ii) display 2D-FFT images of (a-i) and (b-i), respectively in arbitrary scale. Thickness of PS-*b*-PMMA film: t_f = 38 nm.

for $d_S \approx d_0$[27,33], and for the 4× density multiplication of PS-*b*-PMMA cylindrical morphology with $d_S \approx 2d_0$[27]. However, the tolerance of the mismatch for nine-fold density multiplication is smaller than that for 4× density multiplication. The effect of commensurability is interpreted as a thermodynamic competition between the interfacial free energy gain in aligning the diBCP microdomains with the surface template, and the loss of conformational entropy as the chains stretch or compress to achieve the template lattice spacing. In most cases, surface interaction enthalpy dominates to maintain single crystal-like structure up to

about 6–10% stretch of the lattice spacing d_0 in the case of $d_S \approx d_0$.[23,27,33] In comparison, the result presented in Figure 3-4(b-i) and (b-ii) demonstrates that PS-*b*-PMMAcannot maintain a defect-free lattice on d_S = 74 nm. The increase in the lattice spacing from its natural value of d_0 = 24 nm to self-assembled value of d_{obs} = 25 nm on the substrate of d_S = 74 nm corresponds to about 4% stretch in d_0, which is considerably smaller than the critical value for the mismatch in the case of 4× density multiplication with $d_S \approx 2d_0$.[27] The number of pre-patterned lattice points for $d_S \approx 3d_0$ is 1/9 of that for $d_S \approx d_0$ and 4/9 of that for $d_S \approx 2d_0$. Although further systematic work is required, observed results can be attributed to relatively smaller gain in surface interaction enthalpy to overcome the conformational entropy loss of BCP chains for $d_S \approx 3d_0$ compared to that for $d_S \approx d_0$ and $d_S \approx 2d_0$.

3.3.4 Effects of size of chemical pattern points on 9× density multiplication.

Lastly, the effect of size of chemical template lattice points on the self-assembly is examined. As can be clearly seen in Figure 3-2d, radius of the holes of resist pattern prepared by EB lithography, r_{EB} was larger than that of the PMMA cylindrical microdomain self-assembled on the template robs. The r_{EB} and robs measured from SEM micrographs presented in Figure 3-2a and b were 11 nm and 6 nm, respectively. To investigate the limitation of r_{obs}/r_{EB}, chemical templates were prepared by using resist patterns with larger r_{EB} and PS-*b*-PMMA was conducted to self-assemble on them. Results are presented in Figure 3-5. Figure 3-5(a-i) and (b-i) displays SEM images of resist pattern with r_{EB} = 13 nm and 19 nm, respectively. Figure 3-5(a-ii) and (b-ii) displays SEM images of PS-*b*-PMMA self-assembled film with t_f = 38 nm on the chemically pre-patterned templates prepared from the resist patterns in Figure 3-5(a-i) and (b-i), respectively. As can be seen, with increasing r_{EB}, regions with cylinders parallel to the substrate are shown in the SEM images of the self-assembled BCP. The areal regions of cylinders parallel to the substrate increased with increasing template point size. In addition, 2D-FFT image obtained from the region with

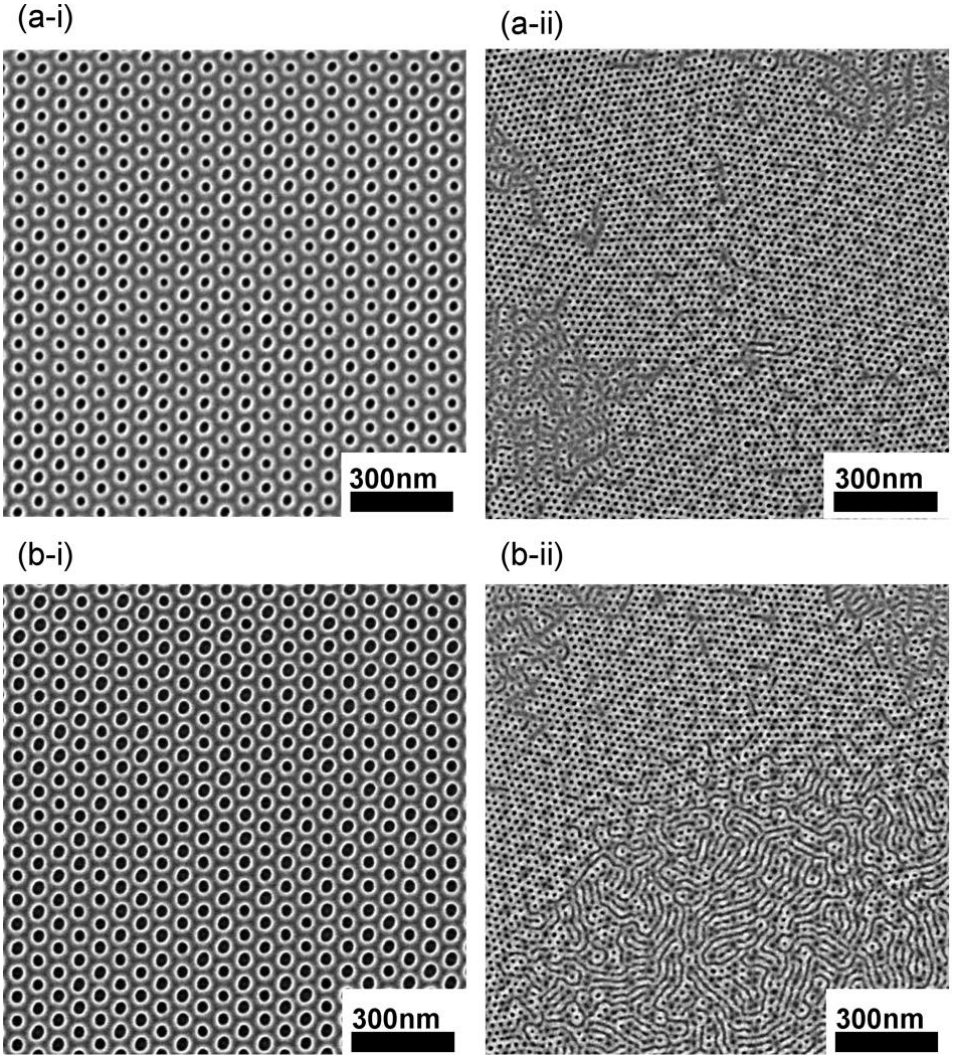

Figure 3-5. (a-i) and (b-i): Top-view SEM images of EB resist employed to pattern PS graft layer on Si wafer surface for a chemically pre-patterned template with d_S = 72 nm. (a-ii) and (b-ii): Top-view SEM images of cylinder structures of PS-*b*-PMMA with d_0 = 24 nm self-assembled on the chemically prepatterned template prepared by applying EB mask shown in (a-i) and (b-i), respectively. Thickness of PS-*b*-PMMA film: t_f = 38 nm.

perpendicularly oriented cylinders displayed a halo pattern (not shown) suggesting that the pre-pattern underneath had limited influence on the arrangement of PMMA cylindrical microdomains. In spite of the changes in PMMA cylindrical microdomain formation, the radii of perpendicularly oriented PMMA cylindrical microdomains remained almost constant at r_{obs} = 6 nm and independent of r_{EB}. The increase in r_{EB} tends to enlarge r_{obs} to minimize

the substrate interaction. However, the increase of robs is unfavorable in terms of the conformational entropy of PMMA chains. Thus, to compensate the substrate interaction and the conformational entropy, the cylinders tend to align parallel to the substrate.

3.4 Conclusion

I have demonstrated a nine-fold feature density multiplication by EB directed BCP assembly that enhances both resolution and throughput of the EB-generated patterns providing a feasible path to fabricating master molds of nanometer scale patterns over macroscopic areas. I have found that the equilibrium formation of perpendicular cylindrical domains in registration with the pre-patterned surface is confined within a narrow thickness and commensurability range as observed in previous simulations and experiments with lower density multiplication factors. As for lattice mismatch between chemical pattern and d spacing of domains, compression of the PS-*b*-PMMA chains is energetically unfavored in comparison to the case of stretching. This tendency has been shown for the four-fold feature density multiplication. However, the tolerance of the mismatch for 9× feature density multiplication is smaller than that for 4× feature density multiplication. I also show that the critical dimension formed by the BCP domains is independent of that defined by the EB pre-patterned features bringing a reliable method for CD control at sub-lithographic resolutions. Viewed from the opposite side, these results indicate that the chemical registration of PS-*b*-PMMA cannot only reduce the lattice spacing but also reduce the pattern radius. Current photolithographic technology utilizes projection exposure to transfer mask pattern in reduced size to the resist. The present results indicate that directed self-assembly can provide alternative route to reduce pattern to the size which cannot be achieved by the current lithography due to the diffraction limit. It should be noted that Stoykovich et al. have successfully directed BCPs to self-assembled into various isolated patterns applicable for integrated circuit by registering the lamella microdomains one-to-one on the chemical

prepattern by applying BCP/homopolymer blend systems.[35] Although present experiments were performed for hcp regular pattern, their results strongly support the possibility to adapt the presented technique to more complex configurations.

3.5 References

1. Smith, B. W.; Bourov, A.; Kang, H.; Cropanese, F.; Fan, Y.; Lafferty, N.; Zavyalova, L. *Proc. SPIE* **2004**, *273*, 5377.
2. Terris, B. D.; Thomson, T. *J. Phys. D Appl. Phys.* **2005**, *38*, R199.
3. Muray, A.; Scheinfein, M.; Isaacson, M.; Adesida, I. *J. Vac. Sci. Technol*. **1985**, *B3*, 367.
4. Yasin, S.; Hasko, D. G.; Ahmed, H. *Microelectron. Eng.* **2002**, *61–62*, 745.
5. Yang, X. M.; Xiao, S.; Wu, W.; Xu, Y.; Mountfield, K.; Rottmayer, R.; Lee, K.; Kuo, D.; Weller, D. *J. Vac. Sci. Technol* **2007**, *B25*, 2202.
6. Park, C.; Yoon, J.; Thomas, E. L. *Polymer* **2003**, *44*, 6725.
7. Hamley, I. W. *Angew. Chem. Int. Ed.* **2003**, *42*, 1692.
8. Segalman, R. A. *Mater. Sci. Eng. R* **2005**, *48*, 191.
9. Hawker, C. J, Russell, T. P. *MRS Bull.* **2005**, *30*, 952.
10. Stoykovich, M. P.; Nealey, P. F. *Mater Today* **2006**, *9*, 20.
11. Khandpur, A. K.; Forster, S.; Bates, F. S.; Hamley, I. W.; Ryan, A. J.; Bras, W.; Almdal, K.; Mortensen, K. *Macromolecules* **1995**, *28*, 8796.
12. Bates, F. S.; Fredrickson, G. H. *Annu. Rev. Phys. Chem.* **1990**, *41*, 525.
13. Hashimoto, T. In *Thermoplastic Elastmers*; Legge, N. R., Holden, G., Schroeder, H. E., Eds.; Hanser: Vienna, 1996.
14. Matsen, M. W.; Schick, M. *Phys. Rev. Lett*. **1994**,*72*, 2660.
15. Takenaka, M.; Wakada, T.; Akasaka, S.; Nishitsuji, S.; Saijo. K.; Shimizu. H.; Kim, M. I.; Hasegawa, H. *Macromolecules* **2007**, *40*, 4399.
16. Black, C. T.; Guarini, K. W.; Milkove, K. R.; Baker, S. M.; Russell, T. P.; Tuominen, M. T. *Appl. Phys. Lett.* **2001**, *79*, 409.
17. Segalman, R. A.; Yokoyama, H.; Kramer, E. J. *Adv. Mater*. **2001**, *13*, 1152.
18. Sundrani, D.; Sibener, S. J. *Macromolecules* **2002**, *35*, 8531.
19. Cheng, J. Y.; Mayes, A. M. *Nature Mater.* **2004**, *3*, 823.

20. Xiao, S. G.; Yang, X. M.; Edwards, E. W.; La, Y. H.; Nealey, P. F. *Nanotechnology* **2005**, *16*, S324.

21. Chen, F.; Akasaka, S.; Inoue, T.; Takenaka, M.; Hasegawa, H.; Yoshida, H. *Macromol. Rapid Commun.* **2007**, *28*, 2137.

22. Rockford, L.; Liu, Y.; Mansky, P.; Russell, T. P.; Yoon, M.; Mochrie, S. G. J. *Phys. Rev. Lett.* **1999**, *82*, 2602.

23. Kim, S. O.; Solak, H. H.; Stoykovich, M. P.; Ferrier, N. J.; de Pablo, J. J.; Nealey, P. F. *Nature* **2003**, *424*, 411.

24. Edwards, E. W.; Stoykovich, M. P.; Solak, H. H.; Nealey, P. F. *Macromolecules* **2006**, *39*, 3598.

25. Welander, A. M.; Kang, H.; Stuen, K. O.; Solak, H. H.; Müller, M.; de Pablo, J. J.; Nealey, P. F. *Macromolecules* **2008**, *41*, 2759.

26. Ruiz, R.; Kang, H.; Detcheverry, F. A.; Dobisz, E.; Kercher, D. S.; Alberecht, T. R.; de Pablo, J. J.; Nealey, P. F. *Science* **2008**, *321*, 936.

27. Tada, Y.; Akasaka, S.; Yoshida, H.; Hasegawa, H.; Dobisz, E.; Kercher, D.; Takenaka, M. *Macromolecules* **2008**, *41*, 9267.

28. Cheng, J. Y.; Rettner, C. T.; Snaders, D. P.; Kim, H. C.; Hinsberg, W. D. *Adv. Mater.* **2008**, *20*, 3155.

29. Edwards, E. W.; Montague, M. F.; Solak, H. H.; Hawker, C. J.; Nealey P. F. *Adv. Mater.* **2004**, *16*, 1315.

30. Wang, Q.; Nath, S. K.; Graham, M. D.; Nealey, P. F.; de Pablo, J. J. *J. Chem. Phys.* **2000**, *112*, 9996.

31. Wang, Q.; Nealey, P. F.; de Pablo, J. J. *Macromolecules* **2001**, *34*, 3458.

32. Wang, Q.; Nealey, P. F.; de Pablo J. J. *Macromolecules* **2003**, *36*, 1731.

33. Park, S. M.; Craig, G. S. W.; Liu, C. C.; La, Y. H.; Ferrier, N. J.; Nealey, P. F. *Macromolecules* **2008**, *41*, 9118.

34. Pickett, G. T.; Witten, T. A.; Nagel, S. R. *Macromolecules* **1993**, *26*, 3194.

35. Stoykovich, M. P.; Kang, H.; Daoulas, K. C.; Lui, G.; Liu C.-C.; de Pablo J. J.; Müller, M.; Nealey P. F. *ACS Nano* **2007**, *1*, 168.

CHAPTER4 DIRECTED SELF-ASSEMBLY OF POSS CONTAINING BLOCK COPOLYMER ON LITHOGRAPHICALLY DEFINED CHEMICAL TEMPLATE WITH MORPHOLOGY CONTROL BY SOLVENT VAPOR

4.1 Introduction

Advances in directed assembly of block copolymer (BCP) thin films are quickly positioning self-assembly as a next-generation lithographic technique.[1−3] BCPs self-assemble via microphase separation to form periodic nanometer-scale structures in the range 5 − 100 nm. The most commonly observed morphologies of diblock copolymers are spherical domains in a body-centered lattice, hexagonally packed cylinders, or alternating lamellae.[4-8] The particular morphology of the self-assembled structure is determined by the relative volume fraction of the constituent blocks. The lattice length parameter of the phase-separated structure depends on the degree of polymerization, N. In order to assemble, the polymer chains must obtain sufficient mobility either by heating above their glass transition temperature, T_g, or by plasticizing with a solvent. However, both thermal and solvent annealing lowers the strength of block copolymer segregation, referred to as Flory−Huggins interaction parameter, χ. Therefore, both annealing conditions must be tuned to allow sufficient mobility for assembly but still fall below conditions that lead to the order−disorder transition(ODT). When annealing between T_g and ODT, the amount of microphase separation is limited by molecular diffusion. Because of the slow mechanism of diffusion, the self-assembled phase lattices form with localized order into numerous polycrystalline type structures with grain boundaries between them. For this reason, the first demonstrations of BCP phase separation as a form of lithography focused on the high pattern

densities that could be attained and ignored the issues of pattern registration and long-range order.[1] More demanding applications such as magnetic storage or semiconductor devices require both registration and long-range ordering. Potential manufacturing applications have fueled extensive research to attain long-range ordering, good feature registration, and accurate placement with a very low number of defects. The BCP self-assembly can be directed by graphoepitaxy (lithographically predefined templates with topographic relief)[9−16] or chemical heteroepitaxy (chemically prepatterned substrates).[17−24] Recent studies have demonstrated that directed self-assembly can have long-range ordering, with a multiple of the density and improved feature placement compared to the original lithographic templates.[9,21−27] Recently reports in which chemical heteroepitaxy was combined with nanofabrication techniques have shown much more complex patterns such as jogs, bends, junctions, chevrons, dashes, rectangular features and even three-dimensional structures.[28−31]

A vast majority of research work on directed self-assembly has been devoted to polystyrene-*block*-poly(methyl methacrylate) (PS-*b*-PMMA), a model material that can be thermally annealed and, because of its PMMA content, may be used as a lithographic photoresist.[10,12,15−24] However, it is difficult for PS-*b*-PMMA to form features with a full pitch below 20 nm because of its small Flory−Huggins interaction parameter. More strongly segregating BCPs have been reported with ≤10 nm scale features.[25,26,32−36] However, achieving long-range order of some highly desirable BCP materials by thermal annealing is not possible because T_g exceeds the thermal degradation temperature of the BCP. In such cases solvent annealing offers an attractive alternative to thermal annealing to order the BCP. Here the solvent vapors dissolve in the BCP and act as a plasticizer. The swollen polymer chains attain sufficient mobility to order at temperatures (commonly at room temperature) well below their degradation temperature.[37] Solvent annealing can be applied to most types of self-assembling BCPs, opening many opportunities to extend directed self-assembly to the sub-10 nm scale.

Solvent annealing also offers the possibility of ordered structures not attainable with thermal annealing. By controlling the degree of swelling of each block, it is possible to reversibly tune the microdomain morphology (i.e., from spherical to cylindrical morphology and vice versa) through order−order transitions.[32,33,38,39] A solvent annealing process is described as follows: first, the as-spun BCP thin film is exposed to solvent vapor. Solvent vapor infiltrates into the BCP and swells the film, creating more free volume in the structure and a different conformational structure for the polymer chains, depending on solubility. In the swollen state, the BCP molecules have the mobility to form the self-assembled patterns.[40,41] After the solvent evaporates, the BCP molecules become frozen in the ordered structure. The morphology of the ordered structure depends on the solubility of the solvent vapor in the polymer blocks and on the degree of swelling during annealing. In fact, the morphologies of BCPs such as polystylene-*block*-polydimethylsiloxane and poly(α-methylstylene)-*block*-poly(4-vinylpyridine) have been engineered over a wide range of structures by controlling the amount and mixture of solvent vapors.[32,38] Bosworth et al.[42] reported that the self-assembled structure of poly(α-methylstyrene)-*block*-poly(4-vinyl-pyridine) ordered by solvent annealing can multiply the areal density of the chemically patterned template with a hexagonal array by a factor of four.

In this chapter, I focus on polyhedral oligomeric silsesquioxane (POSS) containing BCPs. POSS is an attractive organic−inorganic hybrid material because of its molecular cage structure, the flexible functionality based on the substituents on the silicon atoms, and the high etch resistance to oxygen plasma. Hirai et al.[43−45] reported that POSS-containing BCPs, such as polystyrene-*block*-poly(methyl acrylate) POSS (PS-*b*-PMAPOSS) and poly(methyl methacrylate)-*block*-PMAPOSS (PMMA-*b*-PMAPOSS), can be synthesized by living anionic polymerization. They may offer a number of remarkable advantages for self-assembling lithography materials. In particular, the POSS-containing BCPs can self-assemble to well-defined features of a 10 nm scale in the thin films by solvent annealing

under carbon disulfide (CS_2) vapor, and the resulting films show impressive structural stability without dewetting structures even in low molecular weight polymers around 10 K compared with other silicon-containing BCPs such as polystyrene-*block*-polydimethyl-siloxane because of the high T_g of PMAPOSSs. Furthermore, POSS-containing domains have significantly higher etch resistance compared with the organic domains to oxygen reactive ion etching, resulting in promising formation of well-defined nanoporous films as lithography template by the dry etching process.

A solvent annealing process provides a much wider range of parameters that control the ordering of the BCP than a thermal annealing process. Therefore, it is important to characterize the solvent annealing process in detail and understand the effects of each parameter on the ordering process. I show that PMMA-*b*-PMAPOSS thin films annealed in CS_2 vapor undergo an order−order transition from cylindrical domains to spherical domains, with an increase in the degree of swelling. I also show that higher swelling is required for higher molecular weight BCPs to undergo the transition. The results are interpreted in terms of the relative solubility of the solvent vapor in each copolymer and the change in the effective Flory-Huggins parameter in the swollen state, the rate of the solvent evaporation on quenching the film and trapping the structure, and so on. The controlled solvent annealing is applied to the directed self-assembly of PMMA-*b*-PMAPOSS on chemically patterned substrates. I show the feature density multiplication over that of the original chemical pattern via controlled solvent annealing and the effect of the degree of swelling on the uniformity of the density multiplication. I report the long-range ordering and a density gain of 4 times of PMMA-*b*-PMAPOSS BCP films on the chemically prepatterned substrates, to produce 3.7 Tdot/in^2 by the optimized solvent annealing process. I would like to emphasize how critical the precise control of the degree of swelling is to obtain the long-range ordering.

4.2 Experimental Section

4.2.1 Materials.

Figure 4-1 shows the chemical structures of the polymers examined. Five PMMA-*b*-PMAPOSS diblock copolymers and a PMAPOSS homopolymer (hPMAPOSS) were synthesized by living anionic polymerization.[43] A hydroxyl-terminated PMAPOSS (PMAPOSS-OH) was synthesized according to the method described in the Supporting Information. Actually, these materials was supplied by Prof. Hayakawa and coworkers, Tokyo Institute of Technology. A hydroxy-terminated polystyrene (PS-OH) and a PMMA homopolymer (hPMMA) were purchased from Polymer Source Inc., Quebec, Canada, and Sigma-Aldrich, respectively.

The characteristics of the polymers are listed in Table 4-1. The volume fractions of the PMAPOSS blocks in the PMMA-*b*-PMAPOSS samples used in this study were in the range of 83-87%.

4.2.2 Substrates.

The Si wafer substrates were cleaned by immersion in a 7:3 mixture of sulfuric acid and hydrogen peroxide (*piranha solution*) at 80 °C for 10 min and washed with deionized water before using in each experiment.

4.2.3 Preparation of Chemically Patterned Templates.

The piranha solution-cleaned Si substrates were spin-coated with PS-OH or PMAPOSS-OH dissolved in toluene. The PS or PMAPOSS was grafted onto the Si substrate by annealing the substrates in vacuum at 170 °C for 72 h. After the thermal treatment, the substrates were rinsed twice with toluene to remove any unreacted polymers. The characteristics of the PS and PMMAPOSS layers grafted on the Si substrate are listed in

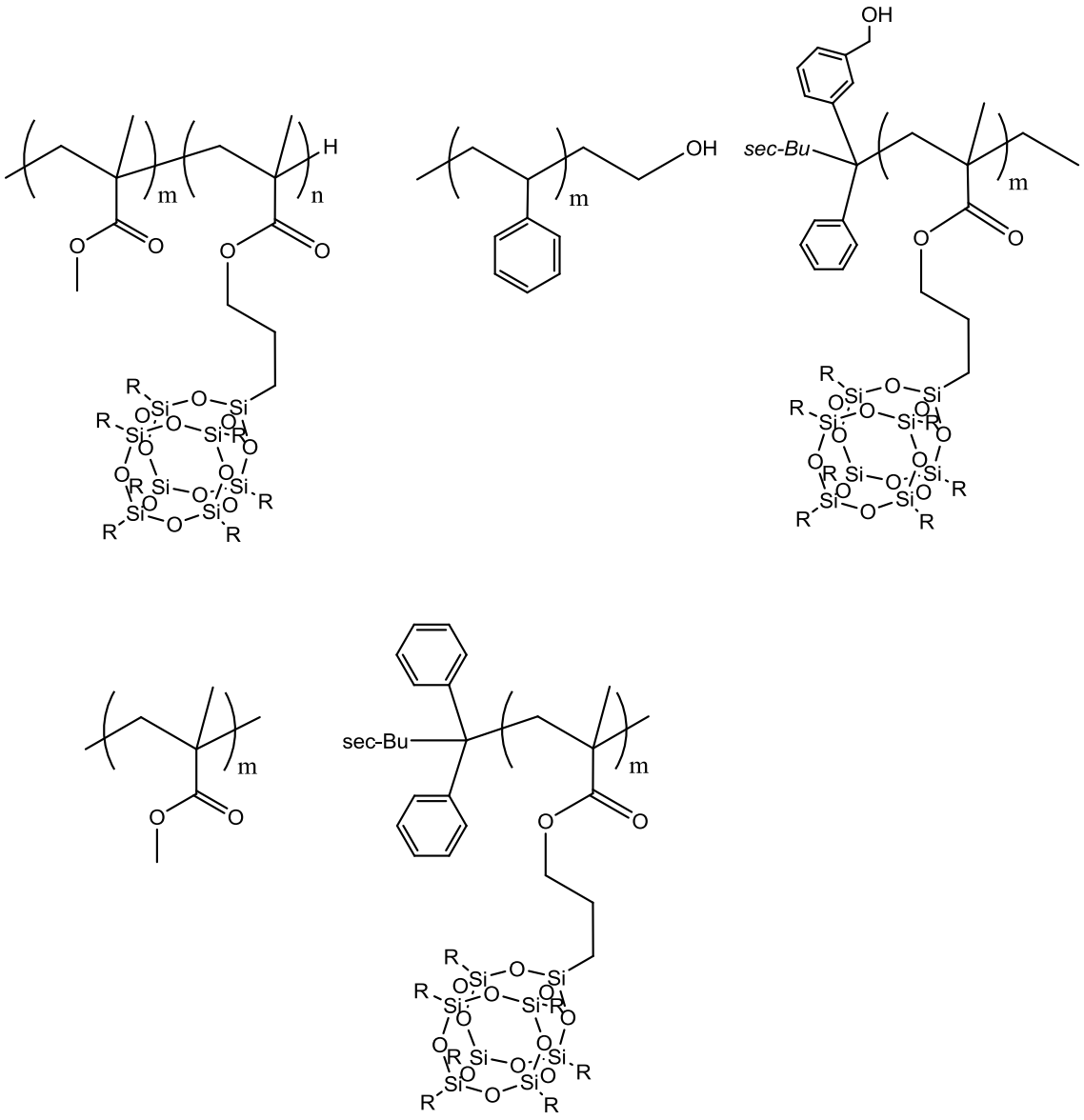

Figure 4-1. Representation of the polymer structures used in this study.

Table 4-1. Characterization of Polymers Used in This Study

Composition [a)-]	M_n [b)] (kg/mol)	M_w/M_n	PMAPOSS Volume fraction [c)]	d_0 [d)](nm)
$PMMA_{49}$-*b*-$PMAPOSS_{34}$	37.4	1.08	0.87	30.0
$PMMA_{41}$-*b*-$PMAPOSS_{29}$	31.3	1.03	0.87	23.7
$PMMA_{34}$-*b*-$PMAPOSS_{18}$	20.9	1.06	0.83	18.3
$PMMA_{27}$-*b*-$PMAPOSS_{14}$	16.2	1.04	0.84	14.0
$PMMA_{25}$-*b*-$PMAPOSS_{13}$	14.9	1.04	0.83	12.4
PMAPOSS-OH	16.5	1.09	-	-
PS-OH	3.7	1.08	-	-
hPMMA	4.0	< 1.1	-	-
hPMAPOSS	29.8	1.04	-	-

[a] The subscript numbers refer to the final composition in terms of the degree of polymerization of each component determined from the gel permeation chromatography (GPC) results and integration from ^{1}H NMR spectra.
[b] Determined by GPC, calibrated against PS standards with THF as an eluent.
[c] Determined by integration from ^{1}H NMR spectra and PMMA and PMAPOSS density of 1.15 and 1.13 g/cm^3 respectively, measured by the density gradient tube method.
[d] Calculated from the 2D-FFT image of the SEM image of PMMA-*b*-PMAPOSS film solvent-annealed on the Si substrate at a certain t_{DS}.

Table 4-2. The average thicknesses of the grafted layers were measured by a ULVAC ESM-4500 ellipsometer. The coverage of the substrate surface was determined by the amount of carbon in a X-ray photoelectron spectroscopy, and the contact angle of PMMA to the polymer grafted surfaces was measured by a Kyowa Interface Science contact angle meter.

A method to measure the contact angle of PMMA with the substrate was described previously.[47]

The PS- or PMAPOSS-grafted layer was patterned by e-beam lithography. A 50 nm PMMA e-beam resist layer was spin-coated onto the PS- or PMAPOSS-grafted Si substrate. The PMMA e-beam resist layer was exposed with a 100 kV electron-beam in a Vistec VB6 system. Arrays of hexagonal dots were exposed, and the resist was developed in a 3:1 isopropanol and deionized water mixture at 2 °C, under ultrasonic agitation. The lattice spacings of the lithographically defined hexagonal arrays of dots, d_S, were set close to equal or twice the lattice spacing, d_0, of the hexagonal array formed by the PMMA-*b*-PMAPOSS. The developed PMMA resist pattern was used to selectively etch the underlying PS- or PMAPOSS-grafted layer by 5 s exposure to oxygen plasma. The surrounding PMMA film was sufficient to mask the matrix of the underlying brush layer during the 5 s etch. After the plasma etching the PMMA was removed with *N*-methyl-2-pyrolidone and toluene, leaving the chemically patterned PS- or PMAPOSS-grafted layer on the Si substrate.

Table 4-2. Characteristics of the Surfaces of the Si Substrate and the Substrates with a Polymer-Grafted Layer Treated by Oxygen Plasma.

surface	thickness of grafted layer[a] (nm)	XPS C_{1S} (CPS)	Contact angle of hPMMA at 170 °C (deg)	
			Before oxygen plasma	After oxygen plasma
Si treated by oxygen plasma	-	1.2×10^3	-	-
PS-OH	5.1	2.7×10^4	25	0
PMAPOSS-OH	3.9	1.2×10^4	66	0

[a] Measured by ellipsometry.

4.2.4 Solvent Annealing.

Thin films of PMMA-*b*-PMAPOSS were spin-cast on the Si substrates or the chemically patterned templates from the dilute solutions either in cyclohexane or chloroform. Cyclohexane and chloroform were used for dissolving $PMMA_{41}$-*b*-$PMAPOSS_{29}$ and the other PMMA-*b*-PMAPOSS, respectively. The film thickness was controlled by the concentration of the solutions and the spinning speed. The film thicknesses were determined by measuring the step height of the film scratched with a sharp knife with a Veeco Dimension 5000 atomic force microscope (AFM).

Figure 4-2 schematically illustrates the solvent annealing apparatus to expose the spin-cast films to carbon disulfide (CS_2) vapor. The concentration (or partial pressure) of CS_2 vapor was controlled indirectly with nitrogen counterflow in a sealed stainless steel chamber. The flow rates of the nitrogen were adjusted by using a flowmeter. As the reference sample,

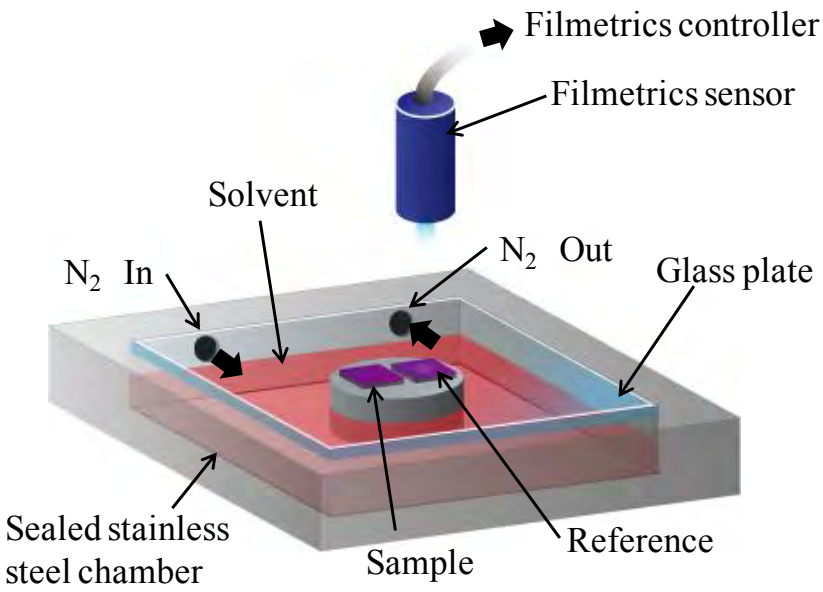

Figure 4-2. Schematic illustration of solvent annealing with an in-situ film thickness monitor. The swollen state of the sample film is controlled by N_2 counterflow rate.

a PMMA-*b*-PMAPOSS film of thickness of 100 nm was always placed in the solvent annealing chamber along with the test samples, and its thickness change was monitored *in situ* with a Filmetrics F20 spectroscopic reflectometer. The degree of swelling (or swelling factor) of PMMA-*b*-PMAPOSS film, t_{DS}, is defined as the thickness of the reference sample in the swollen state divided by the initial film thickness. t_{DS} can be precisely controlled by the counterflow rate as shown in Figure 4-3. The test samples of $PMMA_{41}$-*b*-$PMAPOSS_{29}$ films had a thickness of 35 nm before the solvent annealing. The $PMMA_{41}$-*b*-$PMAPOSS_{29}$ films on the Si substrates were solvent-annealed at various t_{DS} for 1 h. The microstructures of the test samples were determined after the removal of the solvent in less than 30 s by excess nitrogen counterflow.

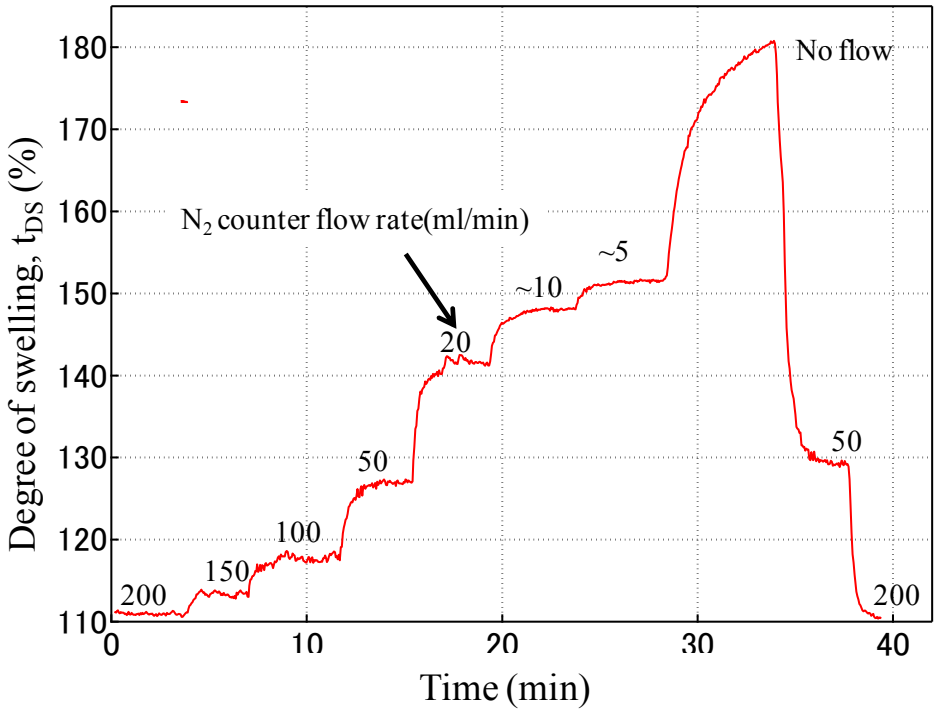

Figure 4-3. Reversible stepwise swelling and deswelling behavior of the $PMMA_{41}$-*b*-$PMAPOSS_{29}$ film by CS_2 vapor. The thin $PMMA_{41}$-*b*-$PMAPOSS_{29}$ film is swollen stepwise with decreasing the N_2 counterflow rate and deswollen with increasing the N_2 conterflow rate. The thickness of the thin film was 118 nm.

In general, the structures of the as-spun films, which depend on the casting solvent, can affect the morphologies after solvent annealing. However, in our experiments, no difference was observed between the two different casting solvents because the mobility of the PMMA-*b*-PMAPOSS chains is sufficient to erase the thermal history of the phase-separated structures in the as-spun films.

4.2.5 Microscopy.

I examined the structures of the self-assembled PMMA-*b*-PMAPOSS films in a Hitachi S-4800 field-emission scanning electron microscope (SEM) operated with an acceleration voltage of 1.5 kV. Since the microdomains of the PMAPOSS blocks contain Si atoms, they discharge more secondary electrons than the microdomains of the PMMA blocks. Therefore, the dark and bright parts of the SEM images correspond to PMMA and PMAPOSS microdomains, respectively. I observed the surface of the self-assembled PMMA-*b*-PMAPOSS films by a Veeco Dimension 5000 AFM instrument to investigate their surface structure.

A thin film of $PMMA_{49}$-*b*-$PMAPOSS_{34}$ was deposited on a KBr substrate with the thickness of 170 nm. The film was swollen to t_{DS} = 185% with CS_2 and held for 1 h. The thin film was dipped in distilled water to dissolve the KBr substrate and floated on water. Ultra thin sections of the thin film of $PMMA_{49}$-*b*-$PMAPOSS_{34}$ with the thickness of ca. 60 nm were prepared at -75°C with a Leica EM FCS ultramicrotome equipped with a cryogenic sectioning kit and observed under a JEOL JEM-2000FX TEM operated at 200 kV. The TEM images were collected with a Bioscan CCD camera with 1k × 1k resolution.

4.3 Results and Discussion

4.3.1 Solvent-Annealed Structures of PMMA-*b*-PMAPOSS Thin Films on Si Substrates without Chemically Patterned Templates.

Hirai et al.[43–45] reported that PMMA-*b*-PMAPOSS can form well-ordered microdomain structures by solvent annealing under CS_2 vapor. I focused our experiments on the effect of the degree of swelling of the BCP on the self-assembled structures during solvent annealing and observed the microdomain structures of the quenched films. Figure 4-4 shows the SEM images of the thin films of $PMMA_{41}$-*b*-$PMAPOSS_{29}$ after solvent evaporation. The dark and bright parts of SEM images correspond to the PMMA and the PMAPOSS domains, respectively. The as-spun film, shown in Figure 4-4(a) did not exhibit a regular structure, although I can distinguish the PMMA domains from the PMAPOSS domains. The rapid evaporation of solvent during spin-coating of the BCP did not allow sufficient molecular mobility for the complete microphase separation of $PMMA_{41}$-*b*-$PMAPOSS_{29}$. In Figure 4-4(b), line structures of the PMMA domains were observed in the films annealed with the swelling factor, t_{DS} = 125%. Figure 4-4(c) shows the coexistence of line and dot structures of the PMMA domains after solvent annealing with the swelling factor, t_{DS} = 150%. The film annealed with the swelling factor, t_{DS} = 175%, shown in Figure 4-4(d), exhibited only the dot structures, where the dots formed hexagonal lattices in the polycrystalline structure. Figure 4-4(e) shows a 2-dimensional Fast Fourier Transform (2D-FFT)[48] image of the hexagonally packed dot structure shown in Figure 4-4(d). The 2D-FFT image exhibited isotropic halos with some spots. From the radius of the circular average of the intensity profile of the first halo in the 2D-FFT image, the lattice spacing of the self-assembled of $PMMA_{41}$-*b*-$PMAPOSS_{29}$ structure, d_0, was calculated to be 23.7 nm. The average radial distribution of the intensity was fitted to a Gaussian function.

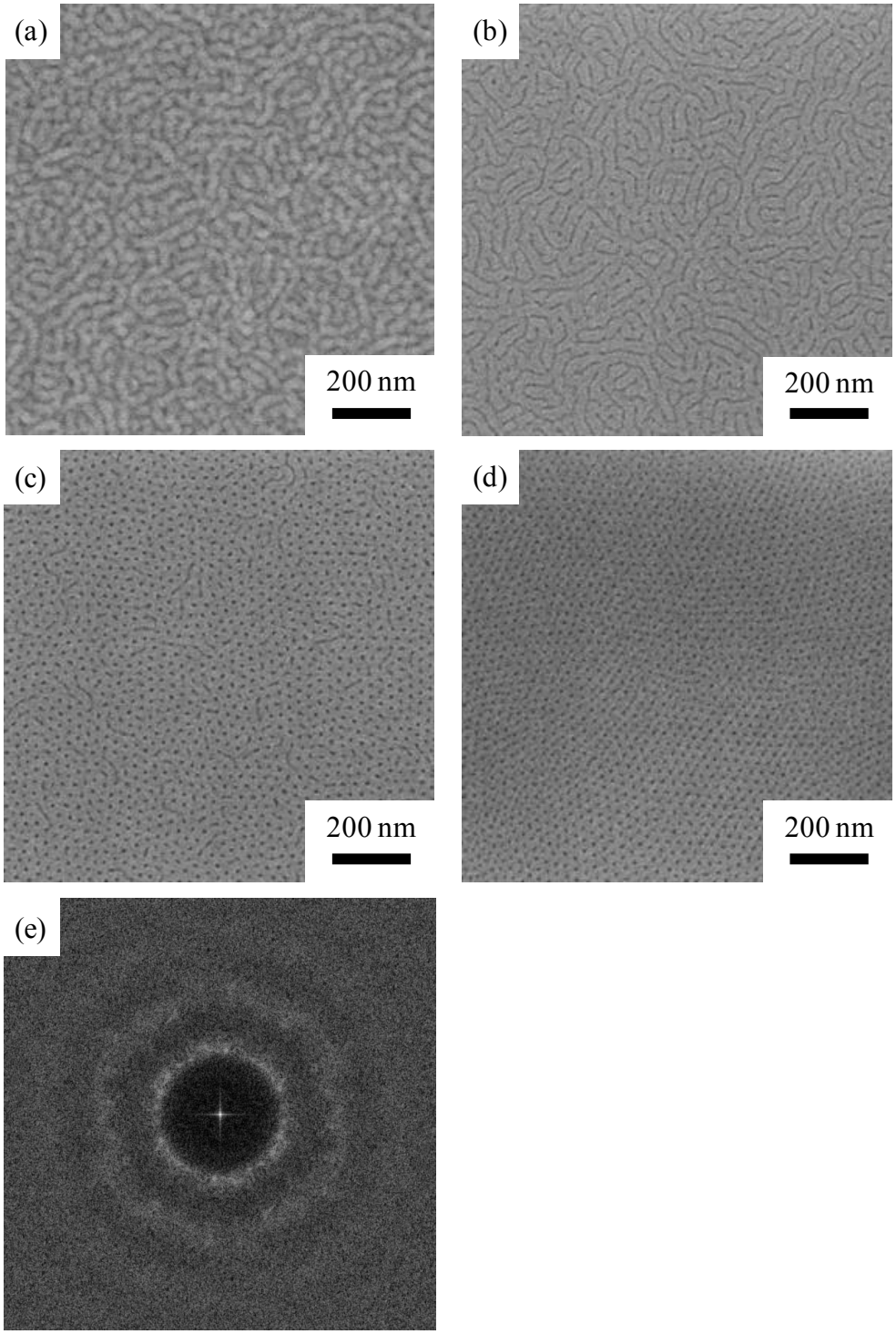

Figure 4-4. SEM images of the $PMMA_{41}$-*b*-$PMAPOSS_{29}$ films on the Si substrates. (a) As-spun film. (b)-(d) Solvent-annealed films. The films were solvent-annealed under CS_2 vapor for 1 h at three different degrees of swelling, t_{DS} of (b) 125%, (c) 150% and (d) 175%. (e) The 2D-FFT image of the SEM image (c). The dark and bright parts of the SEM images correspond to the PMMA and PMAPOSS domains, respectively.

To reveal the morphology of the PMMA domains forming the dot images, as in Figure 4-4(c) and 4-4(d), a cross section of the PMMA-*b*-PMAPOSS film was observed with a transmission electron microscope (TEM). I used a thicker film of the higher molecular weight sample, $PMMA_{49}$-*b*-$PMAPOSS_{34}$, with a larger d_0 of 30.0 nm compared to that of the $PMMA_{41}$-*b*-$PMAPOSS_{29}$ for the purpose of observing the self-assembled structure clearly under TEM. The film was solvent-annealed with the swelling factor, t_{DS} = 185%. The initial film thickness was about 170 nm and the swollen film thickness was 315 nm, which corresponds to about $11d_0$ of $PMMA_{49}$-*b*-$PMAPOSS_{34}$. In the cross section, the PMAPOSS domains were preferentially stained with RuO_4. In the TEM image, shown in Figure 4-5, the bright PMMA domains were observed as the dot structures. Since the top-down SEM image also showed the images with a matrix of spheres, I conclude that the PMMA domains are spherical in the solvent annealed $PMMA_{49}$-*b*-$PMAPOSS_{34}$ (t_{DS} = 185%). I further suggest that since the PMAPOSS volume fractions in the $PMMA_{49}$-*b*-$PMAPOSS_{34}$ BCP and the $PMMA_{41}$-*b*-$PMAPOSS_{29}$ BCP are the same and the swelling factors are similar, the morphology of the PMMA polymer in Figure 4-4(c) and 4-4(d) is also spherical. In this case the polymer morphology changed from cylindrical to spherical as the swell factor increased.

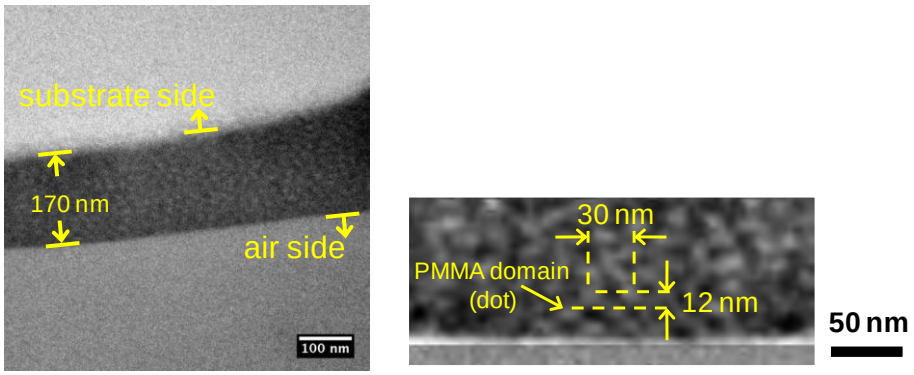

Figure 4-5. Cross-sectional TEM images of the $PMMA_{49}$-*b*-$PMAPOSS_{34}$ film. The dark and bright parts of the TEM images correspond to the PMAPOSS and PMMA domains, respectively.

A morphology change could be explained by a change in relative volume fraction of the constituent blocks of the BCP in the swollen state. Since the block copolymer comprises two immiscible chains, I would expect the solvent molecules to have different affinities for the microdomains with the different blocks.[38] To investigate the relative solubility of the PMMA and PMAPOSS block chains with CS_2, I evaluated the swelling behaviors of the single component films of hPMMA and hPMAPOSS. Each of the hPMMA and hPMAPOSS films spun on the Si substrates was exposed to CS_2 vapor under a N_2 counterflow adjusted to 20 ml/min and t_{DS} was measured as a function of time until it reached a constant value. Under this flow condition, the degree of swelling, $t_{DS,}$ was 123% for hPMMA and 139% for hPMAPOSS (Figure 4-6). This result suggests that CS_2 is slightly selective to PMAPOSS. Thus, preferential partitioning of CS_2 into the PMAPOSS domains is expected in the solvent annealing of the PMMA-*b*-PMAPOSS films. I propose that the solvent annealing induces a change in the effective volume fractions of the two constituent blocks and can change the microdomain morphology from cylinders to spheres in this case.

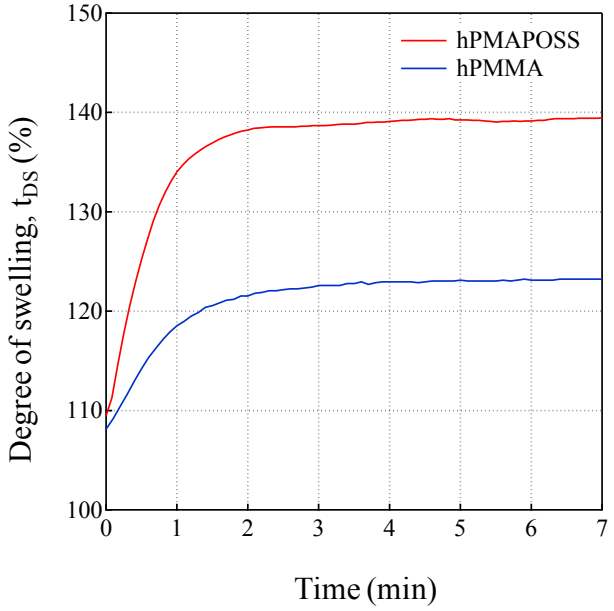

Figure 4-6. Comparison of the degree of swelling between the hPMMA and hPMAPOSS films under a constant N_2 counterflow, and therefore, under a constant CS_2 vapor pressure.

I can further explain the morphologies in Figure 4-4 and Figure 4-5 in terms of the surface energies. Figure 4-7(a) shows the schematic illustrations of the solvent annealing process and the possible cross-sectional structure of the PMMA-*b*-PMAPOSS film at each stage. At the as-spun stage, PMMA-*b*-PMAPOSS is mostly in the disordered state although there may be slightly phase-separated regions. At the swollen stage, the solvent-swollen PMMA-*b*-PMAPOSS chains gain the mobility to diffuse and undergo microphase separation to form the self-assembled structure in thermodynamic equilibrium. If t_{DS} is large enough to induce the order-order transition, the morphology of the PMMA domains might change from cylinders to spheres. Since the surface tension of PMMA against the Si surface is smaller than that of PMAPOSS,[47] a thin wetting layer of PMMA may be formed adjoining to the Si surface. In contrast, the CS_2 vapor at the surface of the film has preference to PMAPOSS. On the solvent evaporation after the solvent annealing, the PMMA-*b*-PMAPOSS film may shrink in the thickness while the lateral size of the film remains unchanged. Therefore, the shape of the PMMA domains in the dried film may not be spherical but ellipsoidal. This expectation was confirmed by the TEM observation of the cross-sectional images of the dried film (Figure 4-5). Figure 4-7(b) shows the AFM height image of the thin film of $PMMA_{41}$-*b*-$PMAPOSS_{29}$ solvent-annealed at t_{DS} = 185%. The hexagonally packed bright dots of the PMMA domains were observed under the topographical contrast and the dots were found to be 2-3 nm thicker than the PMAPOSS matrix. This result suggests that the degree of shrinkage of the PMMA domains is less than that of the PMAPOSS matrix, which is consistent with the higher solubility of CS_2 in PMAPOSS. Final confirmation of the above model would require *in-situ* observation of the swollen films by grazing incidence small-angle X-ray scattering (GI-SAXS) with synchrotron radiation, which is beyond the scope of this work.

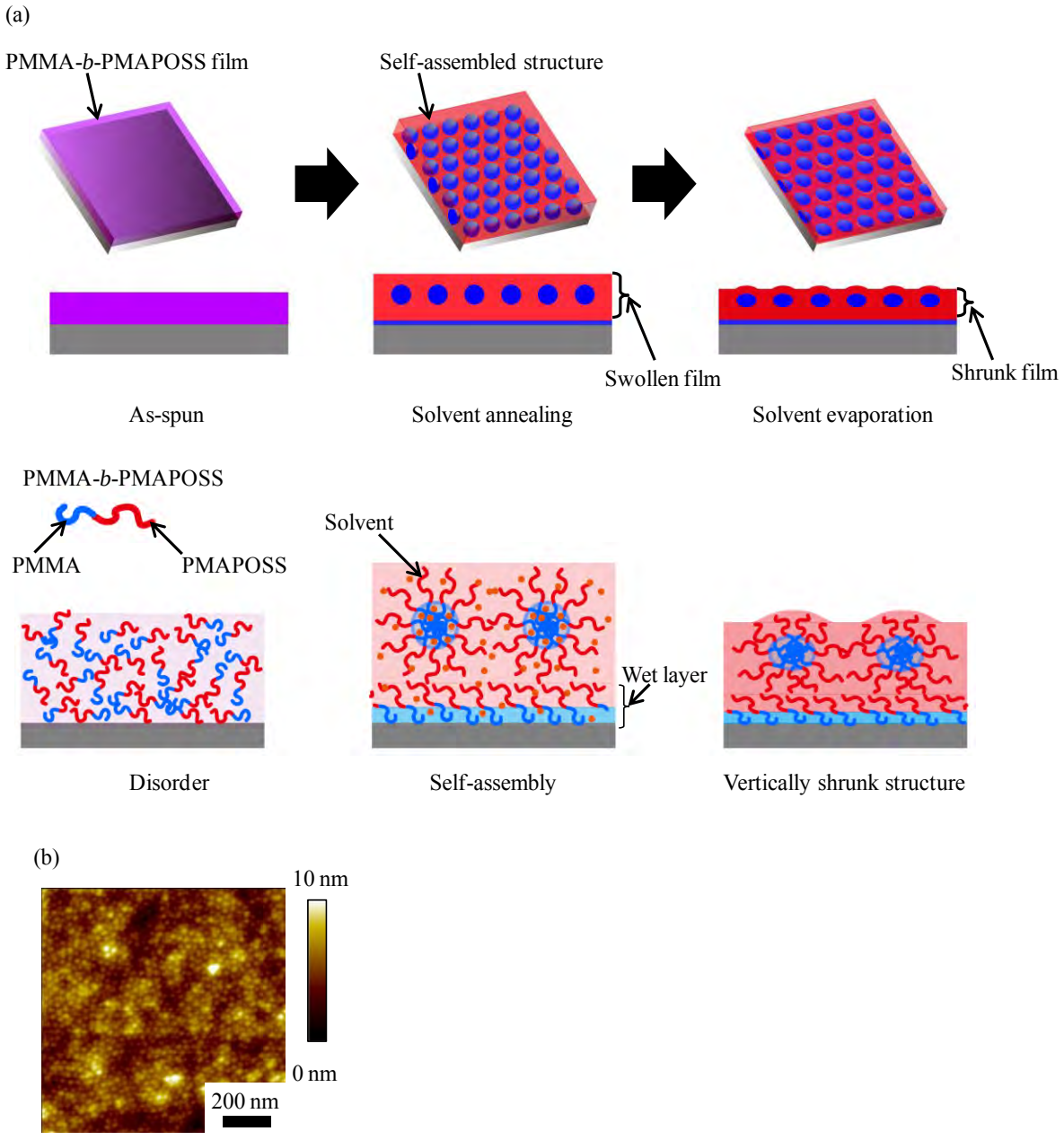

Figure 4-7. (a) Schematic illustrations of the solvent annealing process and the possible cross-sectional structures at each stage of the process. Red and blue chains represent the PMAPOSS and PMMA chains, respectively. Orange dots represent the CS_2 solvent molecules. (b) The AFM topographic image of the $PMMA_{41}$-*b*-$PMAPOSS_{29}$ film solvent-annealed at t_{DS} = 185% for 1h on the Si substrate.

4.3.2 Effect of Molecular Weight of PMMA-*b*-PMAPOSS on Self-assembled Structures.

I further examined the CS_2 solvent annealing behavior of other molecular weights of PMMA-*b*-PMAPOSS.

Figure 4-8 shows the SEM images of the 15 nm thick, as-spun, films of $PMMA_{25}$-*b*-$PMAPOSS_{13}$ solvent annealed for one hour under different swelling factors. As expected in Figure 4-8(a), the as-spun film did not exhibit a periodic structure. Figure 4-8(b) shows coexistence of line and dot structures of the PMMA domains when the swelling factor was t_{DS} = 120% during annealing. The line structures are derived from the cylindrical PMMA microdomains oriented parallel to the Si substrate. The dot structures are most likely the spherical PMMA microdomains. When the swelling factor was increased to t_{DS} = 130%, the PMMA domains exhibited a disordered dot structure as shown in Figure 4-8(c). This result suggests that with the 130% swelling factor, the PMMA-*b*-PMAPOSS chains do not gain sufficient mobility to form a single hexagonal lattice. However, as the degree of swelling of the film increased to t_{DS} = 140% and 150%, a regular hexagonal array of dots formed as shown in Figure 4-8(d) and (e). From the position of the first-order halo observed in the 2D-FFT image of Figure 4-8(g) obtained from the SEM image in Figure 4-8(d), d_0 of the self-assembled structure of $PMMA_{25}$-*b*-$PMAPOSS_{13}$ at t_{DS} = 140% was determined to be 12.4 nm. In the same way, d_0 at t_{DS} = 150% was calculated to be 12.7 nm. Conversely, as the degree of swelling of the film further increased to t_{DS} = 175%, the hexagonally packed dot pattern did not exhibit the extent of order observed in the samples annealed with the swelling factors of t_{DS} = 140% and 150%, as shown in Figure 4-8(f). According to Lodge et al.,[49] swelling of cylinder-forming BCP systems with a neutral solvent lowers the effective Flory-Huggins interaction parameter of the copolymers. In addition, greater swelling of one component of the BCP that has a slightly greater affinity for the solvent can increase the volume fraction of the corresponding microdomains in the swollen state. CS_2 is slightly selective for PMAPOSS over PMMA and the solvent annealing can increase $\phi_{PMAPOSS}$ and

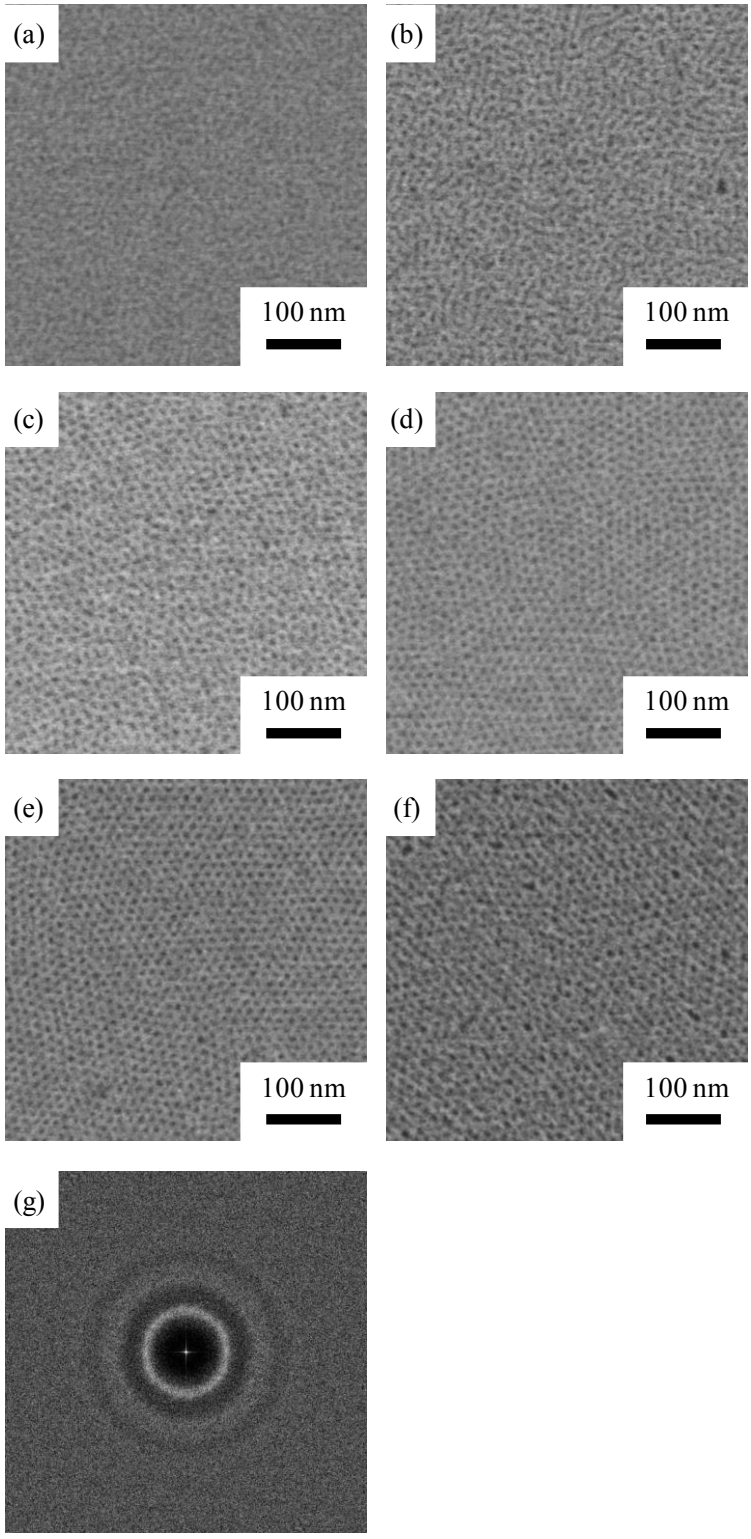

Figure 4-8. SEM images of the $PMMA_{25}$-*b*-$PMAPOSS_{13}$ films. (a) As-spun film. (b)-(f) Solvent-annealed films. The films were solvent-annealed on the Si substrates at various t_{DS} of (b) 120%, (c) 130%, (d) 140%, (e) 150% and (f) 175%. (g) The 2D-FFT image of the SEM image (d). The dark and bright parts of the SEM images correspond to the PMMA and PMAPOSS domains, respectively.

decrease χ in the swollen state.[43] The effects of the solvent annealing can be described with a schematic phase diagram of the microdomain morphology in $\chi_{eff}N$ versus $\phi_{PMAPOSS,\ eff}$ space as shown in Figure 6 where χ_{eff}, N, and $\phi_{PMAPOSS,\ eff}$ are the effective Flory-Huggins interaction parameter in the swollen state, the degree of polymerization, and the effective volume fraction of the PMAPOSS blocks in the swollen state, respectively.[38,49,50] The morphological change with increasing t_{DS} can be recognized as a diagonal shift in the phase diagram along the solid arrow in Figure 4-9. Therefore, the morphology of the PMMA domains changes from cylindrical to spherical with increasing t_{DS}. Furthermore, the phase separated structure may become unstable and the long-range order may become worse on the solvent annealing at t_{DS} > 175% because of the transition from the spherical microdomain

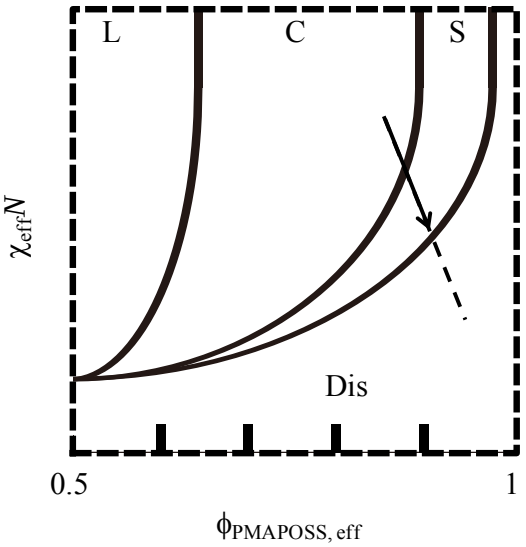

Figure 4-9. Right half of the schematic phase diagram of $\chi_{eff}N$ versus $\phi_{PMAPOSS,eff}$ for PMMA-*b*-PMAPOSS/CS_2 system. PMMA is the minor component and forms the dispersed domains in the cylindrical (C) and spherical (S) morphologies. The $\chi_{eff}N$ value of the BCP decreases with the infiltration of the solvent into the film. Since CS_2 swells the PMAPOSS matrix more than the PMMA domains, the effective volume fraction of PMAPOSS, $\phi_{PMAPOSS,\ eff}$, increases on swelling. The phase behavior of the BCP with increasing t_{DS} on solvent annealing is represented by the solid arrow, which predicts the morphological transition from cylinders to spheres upon swelling. The dashed line predicts the order-disorder transition at excess t_{DS}. The behavior of the BCP with a higher M_n on solvent-annealing is represented by the dotted arrow, which is obtained by the vertical shift of the solid arrow.

morphology to the disorder state. This case is represented by a further diagonal shift on the dashed line in the phase diagram. Our results show that the optimum swelling factor to form a well-defined hexagonally packed dot pattern with $PMMA_{25}$-*b*-$PMAPOSS_{13}$ is in the range between 140 and 150%.

Similarly, I investigated the effect of t_{DS} on the self-assembled structures of $PMMA_{34}$-*b*-$PMAPOSS_{18}$ and $PMMA_{27}$-*b*-$PMAPOSS_{14}$ possessing the $\phi_{PMAPOSS}$ values of 83% and 84%, respectively, which are similar to the $\phi_{PMAPOSS}$ values for $PMMA_{41}$-*b*-$PMAPOSS_{29}$ and $PMMA_{25}$-*b*-$PMAPOSS_{13}$ (see Figures 4-10 and 4-11). The results are summarized in Figure 7, which presents the phase diagram of the self-assembled structures of the solvent annealed PMMA-*b*-PMAPOSS. The open circles and diamonds denote the spherical and cylindrical morphologies, respectively, while the open triangles indicate coexistence of the spheres and cylinders. Figure 4-12 shows that the phase boundary for the cylinder-to-sphere transition shifts towards the higher values of t_{DS} with increasing M_n of PMMA-*b*-PMAPOSS. This can be understood qualitatively in terms of $\chi_{eff}N$ and $\phi_{PMAPOSS,eff}$ in the swollen state using Figure 4-9. As t_{DS} increases on swelling with CS_2, χ_{eff} decreases while $\phi_{PMAPOSS,eff}$ increases due to the higher affinity of CS_2 for PMAPOSS. It eventually induces the morphology transition from cylinders to spheres as represented by the arrow in Figure 4-10 for the PMMA-*b*-PMAPOSS with a smaller M_n. On the other hand, an increase in M_n of PMMA-*b*-PMAPOSS increases $\chi_{eff}N$ and prompts the backward shift along the arrow. Thus, a larger t_{DS}, which further reduces the χ_{eff} value, is necessary for the PMMA-*b*-PMAPOSS with a larger M_n to undergo the morphological transition from cylinders to spheres. Consequently, the phase boundary for the cylinder-to-sphere transition shifts towards the higher values of t_{DS} with increasing M_n of PMMA-*b*-PMAPOSS as shown in Figure 4-12. Although the discussion given above is qualitative, it suggests that I need to optimize the degree of swelling in the solvent

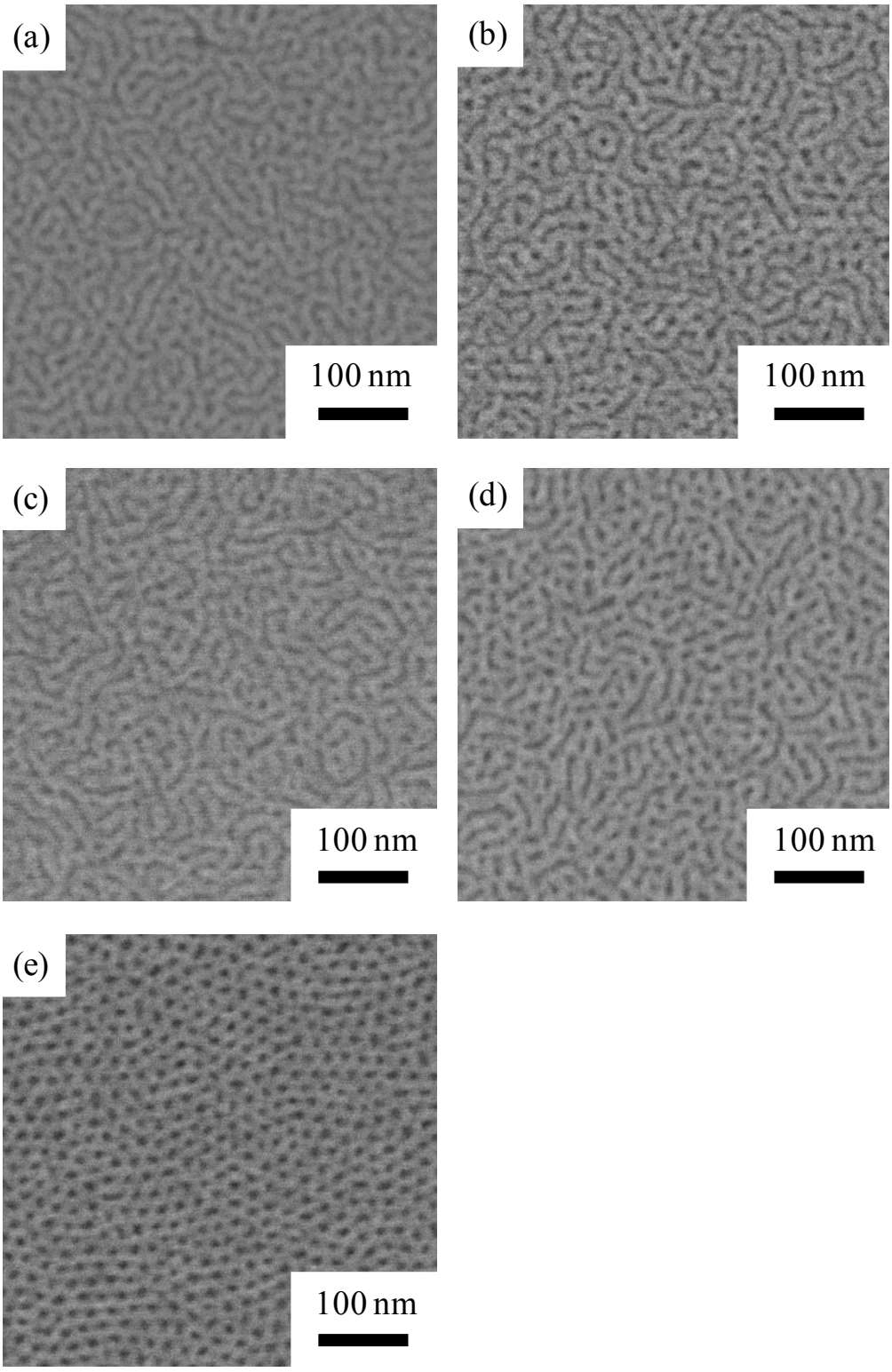

Figure 4-10. SEM images of the $PMMA_{34}$-*b*-$PMAPOSS_{18}$ films on the Si substrates. (a) As-spun film. (b)-(f) Solvent-annealed films. The films were solvent-annealed on the Si substrates at various degrees of swelling: (b) t_{DS} = 120%, (c) t_{DS} = 130%, (d) t_{DS} = 140%, and (e) t_{DS} = 150%. The dark and bright parts of the SEM images correspond to the PMMA and PMAPOSS domains, respectively.

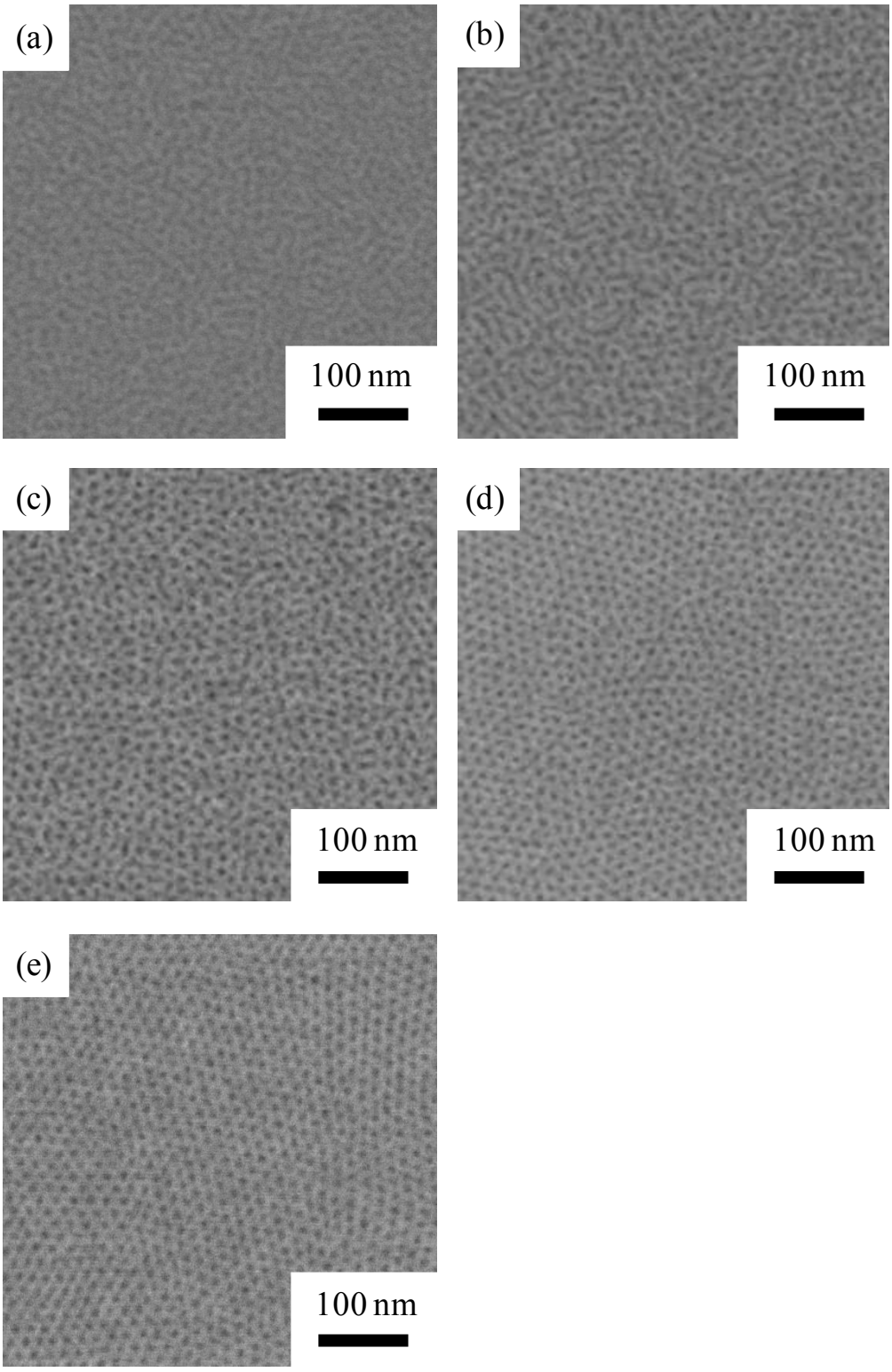

Figure 4-11. SEM images of the $PMMA_{27}$-*b*-$PMAPOSS_{14}$ films on the Si substrates. (a) As-spun film. (b)-(f) Solvent-annealed films. The films were solvent-annealed on the Si substrates at various degrees of swelling: (b) t_{DS} = 120%, (c) t_{DS} = 130%, (d) t_{DS} = 140%, and (e) t_{DS} = 150%. The dark and bright parts of the SEM images correspond to the PMMA and PMAPOSS domains, respectively.

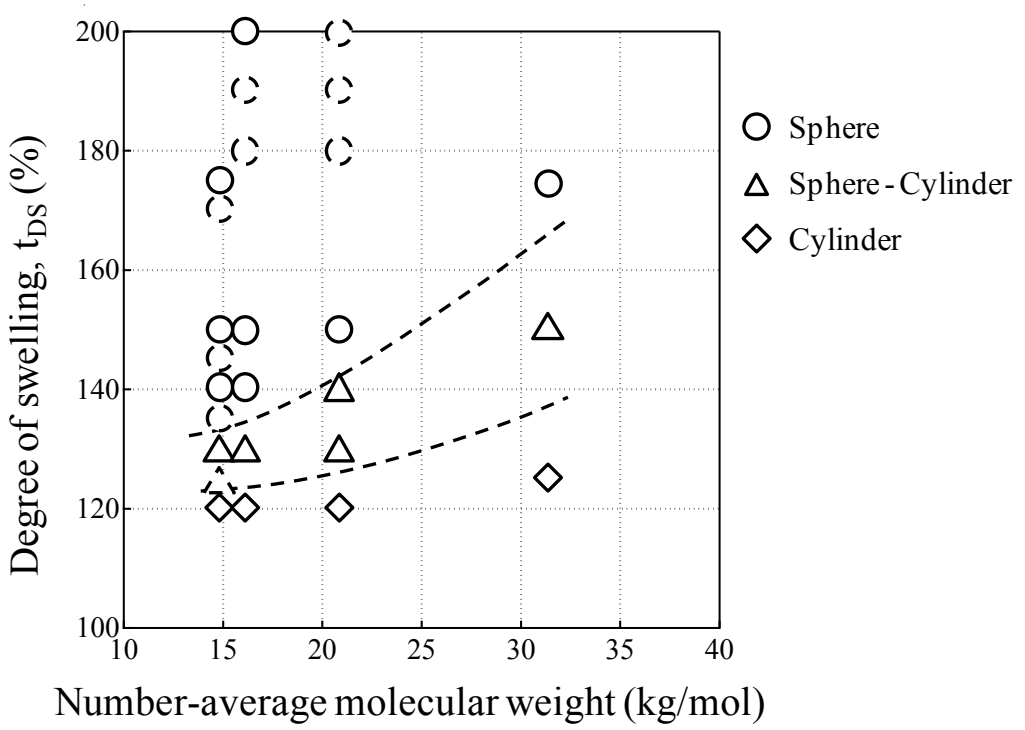

Figure 4-12. Phase diagram showing the morphologies of PMMA-*b*-PMAPOSS assembled via solvent-annealing with CS_2 vapor as a function of degree of swelling, t_{DS}, and number-average molecular weight of PMMA-*b*-PMAPOSS. The volume fraction of PMAPOSS in the PMMA-*b*-PMAPOSS samples, $\phi_{PMAPOSS}$ was in the range of 83-87 %. Open circles, triangles and diamonds represent sphere, mixtures of sphere and cylinder, and cylinder morphologies of the PMMA domains, respectively.

annealing to obtain the desired hexagonally packed dot pattern depending on the M_n of PMMA-*b*-PMAPOSS.

4.3.3 Characteristics of Chemically Patterned Template Surface.

In the previous section, I have determined the optimized solvent-annealing conditions to prepare well-defined highly-ordered arrays of dots of PMMA-*b*-PMAPOSS BCPs on the Si substrates. I now consider, directing the self-assembly process during the solvent annealing with chemical heteroepitaxy. Figure 4-13 shows a schematic illustration of the directed self-assembly process of PMMA-*b*-PMAPOSS, which forms PMMA spheres in PMAPOSS matrix on a chemically patterned template. The template with chemical contrast

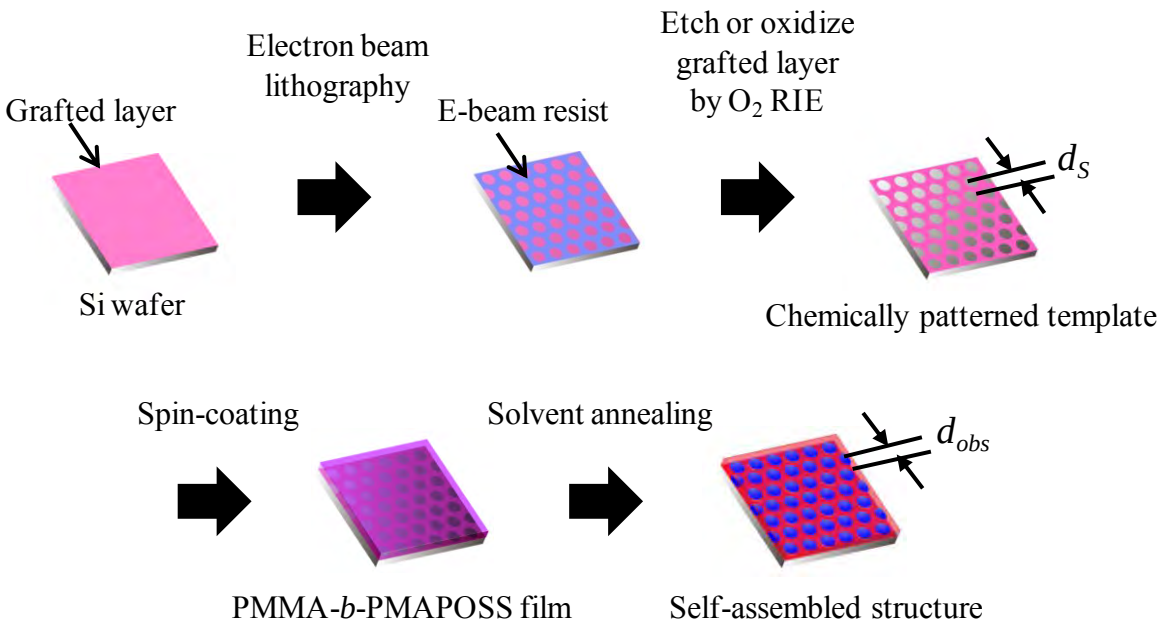

Figure 4-13. Schematic illustration of the directed self-assembly process with a chemically patterned template.

Table 4-3. Characteristics of the Patterns Formed with EB Lithography

d_S (nm)	L_S (nm)	d_{eb} (nm)	σ_{eb} (nm)
23	26	23.3	3.4
24	28	24.6	2.1
26	30	26.3	2.2
28	32	28.4	2.7

was composed of a hexagonal array of circular dots preferentially wetted by PMMA surrounded by a background matrix with higher affinity for PMAPOSS. The lattice spacing, the distance between adjacent planes, is denoted as d_S while the lattice constant, the distance between nearest neighbors, is represented as L_S. The preparation of the chemically patterned grafted film was described above. The patterned template had an array of etched dots that had surface affinity for the PMMA component of the BCP. The surrounding matrix of unetched surface favored the PMAPOSS component of the BCP.

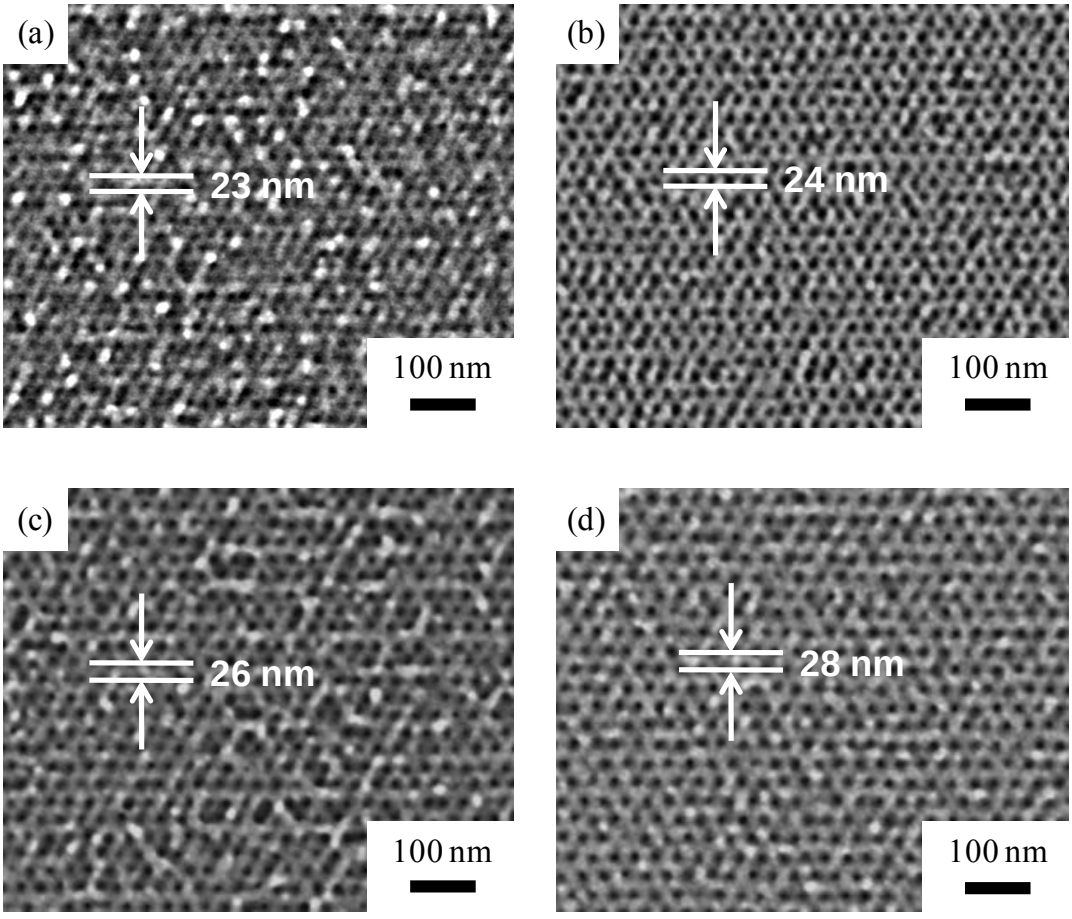

Figure 4-14. SEM images of the PMMA e-beam resist layer formed by e-beam lithography, which was employed to prepare the chemically patterned substrates. The resist pattern was etched with the oxygen plasma required to change the chemistry of the substrate. (a) d_S = 23 nm, (b) d_S = 24 nm, (c) d_S = 26 nm, and (d) d_S = 28 nm.

The geometric components of the e-beam lithography defined chemically patterned templates, d_S and L_S, are listed in Table 4-3. To evaluate the pattern quality of the chemically patterned templates, I evaluated the PMMA e-beam resist patterns on the PS brush after development. The surface of the PMMA e-beam resist was sputter coated with about 1 nm thick layer of Pt prior to SEM observations. Figure 4-14 shows the SEM images of the resist layer. The dark and bright parts of the SEM images correspond to the patterned holes in the PMMA e-beam resist layer and the remaining PMMA resist layer, respectively. As shown in Figure 4-14, there were several defects in the patterns with d_S = 23 nm (part a), while there were almost no defects in the patterns with d_S = 24, 26, and 28 nm (parts b, c, and d, respectively). The summary of the characteristics of the observed patterns in Figure 4-14 is given in Table 4-3. The average lattice spacing of the patterns, as measured by our SEM, are denoted as d_{eb}, and its standard deviation σ_{eb}. The method employed to evaluate d_{eb} and σ_{eb} was described in the previous study.[23] The d_{eb} values almost agreed with the designed values, d_S. The pattern with d_S = 23 nm showed the largest σ_{eb} value of 3.4 nm, but the σ_{eb} values of the other patterns were less than 3 nm.

4.3.4 Chemical Heteroepitaxy with Chain Mobility from Solvent Annealing.

I investigated the effect of the solvent annealing on the chemical heteroepitaxy for the thin films of PMMA-*b*-PMAPOSS on the chemically patterned templates of grafted PS-OH on the Si substrates. Thin films of $PMMA_{41}$-*b*-$PMAPOSS_{29}$ with d_0 = 23.7 nm were spin-coated onto the chemically patterned substrates and solvent-annealed for 3h. The solvent annealing was performed with a swelling factor of t_{DS} = 185% so that $PMMA_{41}$-*b*-$PMAPOSS_{29}$ self-assembled in the well-defined hexagonal array of dots. The thickness of the $PMMA_{41}$-*b*-$PMAPOSS_{29}$ film was optimized to 12 nm to prevent the spherical PMMA domains from forming two layers upon swelling. At t_{DS} = 185%, the

thickness of the film is expected to increase by swelling from 12 nm to 22 nm, which is nearly equal to d_0 inherent to $PMMA_{41}$-*b*-$PMAPOSS_{29}$.

Figure 4-15 shows that chemical epitaxial direction can be achieved with the sphere forming block copolymer solvent annealing conditions. The SEM image and the corresponding 2D-FFT image of a thin film of $PMMA_{41}$-*b*-$PMAPOSS_{29}$ self-assembled on the chemically patterned template with d_S = 23 nm is shown in Figure 4-15(a). The self-assembled structure on the template with d_S = 23 nm resulted in a single hexagonal lattice with almost no point defects, in contrast to the relatively poor quality of the chemically patterned template shown in Figure 4-14(a). The 2D-FFT image exhibits only spots as expected from the single hexagonal lattice, with the peaks to at least the fifth order. The lattice spacing of the self-assembled structure on the template, denoted as d_{obs}, calculated from the 2D-FFT image was 23.2 nm, which is the same as that of the underlying template, d_S = 23 nm. This result demonstrates that with appropriate solvent annealing conditions PMMA-*b*-PMAPOSS can self-assemble to form a well-oriented hexagonal lattice pattern with a long-range order along the chemically patterned template and rectify the defects of the chemically patterned template as can thermally annealed PS-*b*-PMMA.[23]

In Figures 4-15(b) and (c), I examined the effect of the lattice mismatch of the chemically patterned template on the quality of the self-assembled structure. As shown in Figure 15(b) and (c), single hexagonal lattices were also observed on the templates with d_S = 24 nm and 26 nm, which were both slightly larger than the d_0 (= 23.7 nm) of $PMMA_{41}$-*b*-$PMAPOSS_{29}$. The corresponding 2D-FFT images exhibited only spots, with the peaks at least to the sixth order. The d_{obs} values of the self-assembled structures for Figure 4-15(b) and (c) were 24.3 nm and 26.5 nm, respectively, which agreed with the d_S values of the template patterns. This result suggests that the lattice spacing d_{obs} of the self-assembled structures can be stretched to match the d_S of the underlying templates, at least up to 12%

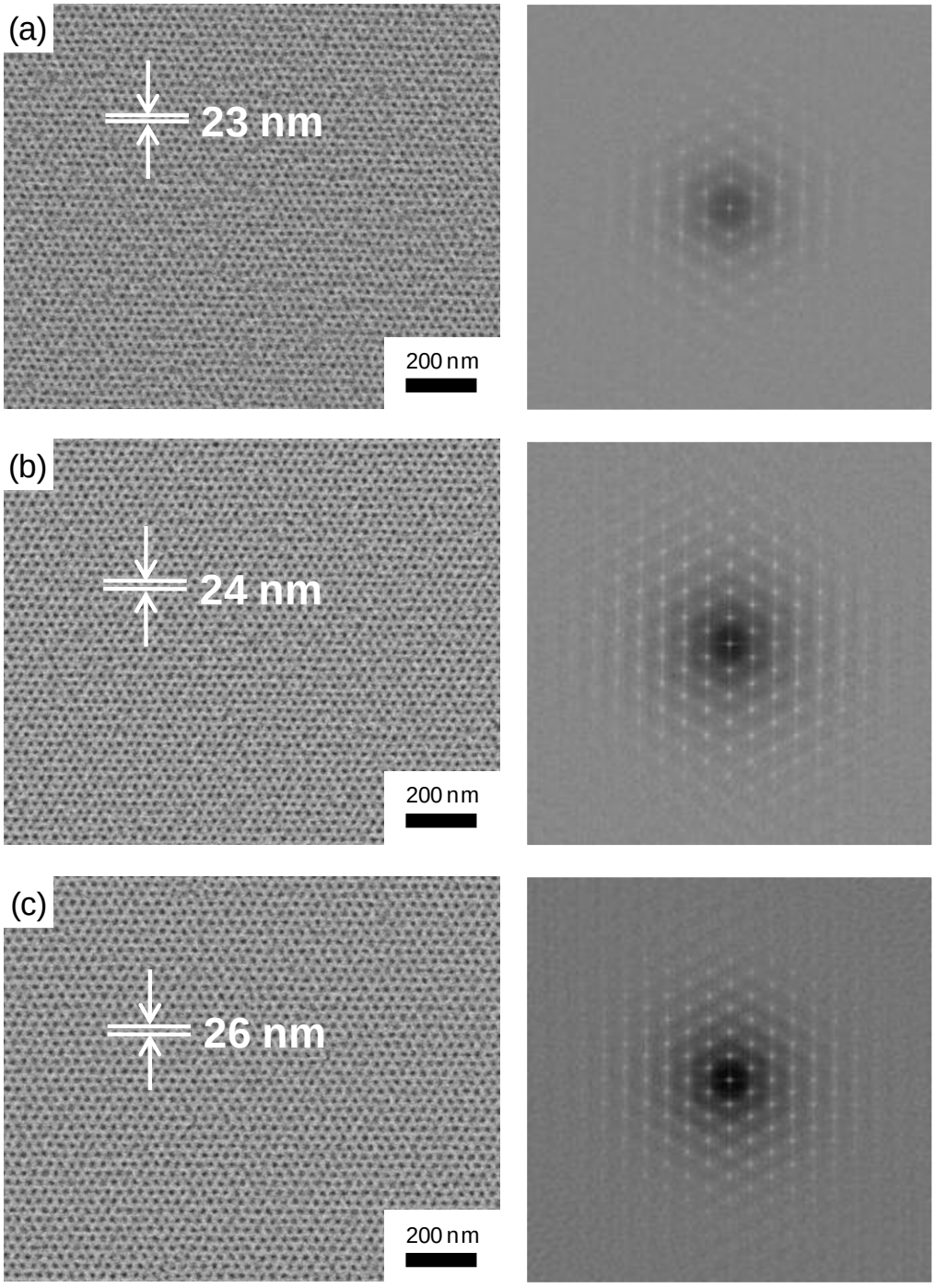

Figure 4-15. SEM images and the corresponding 2D-FFT images of the $PMMA_{41}$-*b*-$PMAPOSS_{29}$ thin films solvent-annealed on the chemically prepatterned templates composed of the PS-OH grafted layer. (a) d_S = 23 nm, (b) d_S = 24 nm, and (c) d_S = 26 nm. The film thickness is 12 nm.

(d_{obs}/d_0 = 26.5/23.7 = 1.12) larger than d_0. This finding implies some extended flexibility in the chemically patterned template design.

Xiao *et al.*[25] proposed that the spherical microdomains of a BCP formed on the chemically patterned templates could be spherical, hemispherical, or disk-like, depending on the relative size of the patterned features with respect to the inherent size of the BCP spherical domains. I also believe that the morphology of the spherical microdomains on the patterned template might have been deformed by the favorable interaction between the PMMA blocks and the Si substrate of the patterned template. However, confirming such a hypothesis requires a direct observation of the cross-sectional images of the BCP thin films by SEM or TEM, which is beyond the scope of this work.

The limit of the commensurability may be determined by the two competing thermodynamic factors: the interfacial free energy reduction by the lattice matching between the BCP microdomains and the template patterns, and the conformational entropy loss as the chains stretch or shrink to achieve the template lattice spacing.

4.3.5 Effect of PMAPOSS Grafted Surface of the Chemically Patterned Template.

Next, I examined the use of a PMAPOSS-OH chemically patterned template for the ordering of a thin film of $PMMA_{41}$-*b*-$PMAPOSS_{29}$ with solvent annealing, again with chemical pattern pitch 23, 24, and 26 nm. The samples were solvent annealed under conditions for a swelling factor of t_{DS} = 185% for 3 h.

Figure 4-16 shows the SEM images and the corresponding 2D-FFT images of the self-assembled structures on the templates prepared with PMAPOSS-grafted surface. Ordering on the d_S = 23 nm template pattern, shown in Figure 4-16(a), gave mixed results. Some grains of the BCP self-assembled structure matched their lattice to that of the underlying template with d_S = 23 nm, but large dark regions were also observed, differing from the case of the PS-grafted template. The 2D-FFT image presented in Figure 4-16(a)

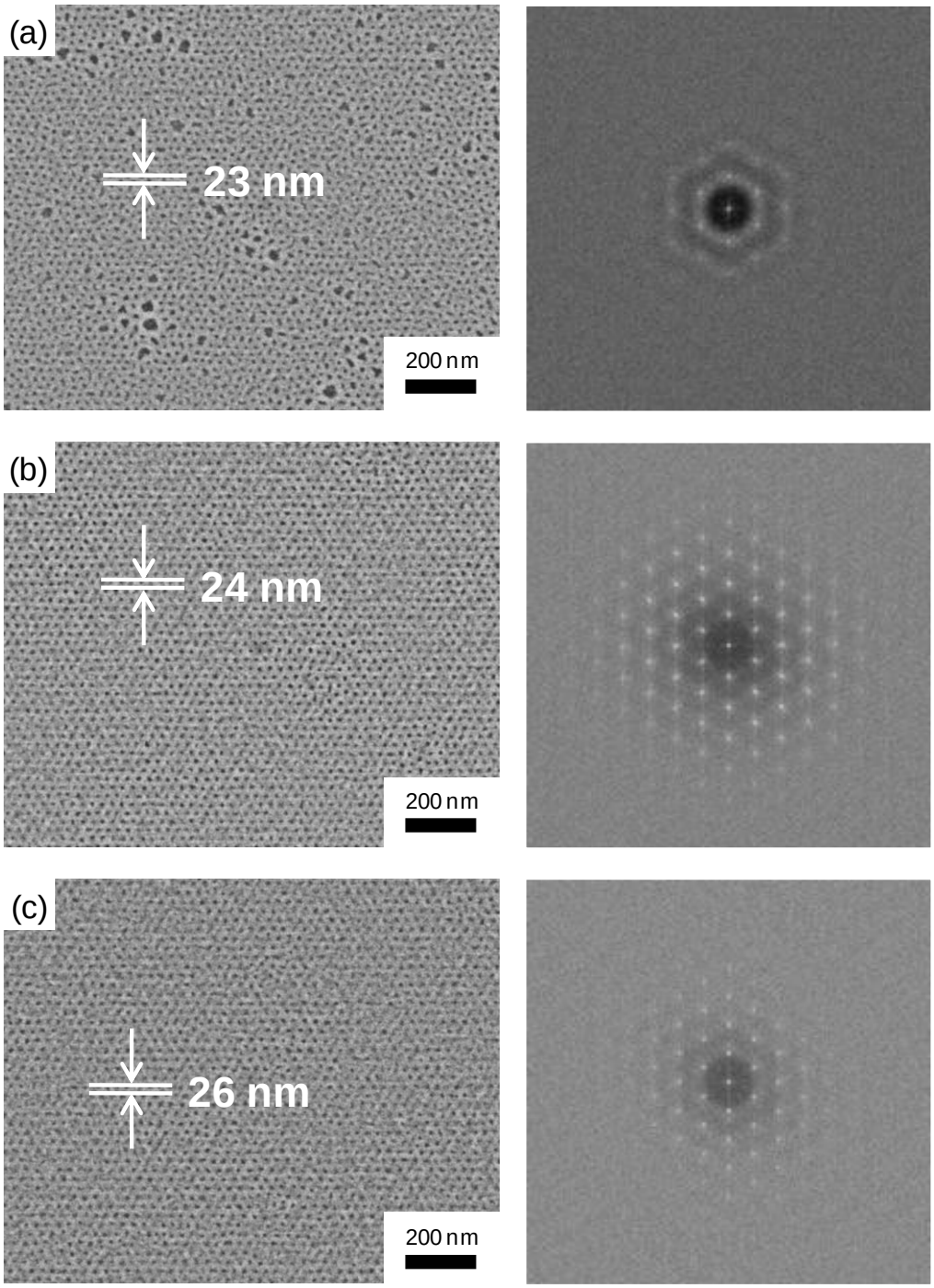

Figure 4-16. SEM images and the corresponding 2D-FFT images of the $PMMA_{41}$-*b*-$PMAPOSS_{29}$ thin films solvent-annealed on the chemically prepatterned templates composed of PMAPOSS-OH grafted layer. (a) d_S = 23 nm, (b) d_S = 24 nm, and (c) d_S = 26 nm. The film thickness is 12 nm.

exhibited a spot and halo pattern. Better results were obtained from the chemically patterned template patterns with d_S = 24 nm and 26 nm. Single well ordered hexagonal lattices were observed as shown in Figure 4-16(b) and (c), respectively. The accompanying 2D-FFT images exhibit only spots, with peaks up to fourth order. Thus well ordered self-assembled structures formed on chemically patterned templates of PMAPOSS-OH patterned with d_S = 24 and 26 nm. However the d_s = 23 nm lattice clearly formed more readily on the chemically patterned PS-OH template than on the chemically patterned PMAPOSS-OH template. Table 4-2 shows a comparison of the wettability of a PMMA homopolymer to a PS-grafted surface and to a PMAPOSS-grafted surface. The interfacial energy of the PMMA component of the block copolymer to the PS grafted surface is less than that on the PMAPOSS-grafted surface. The lower chemical contrast of the PS surface could explain the wider latitude in lattice spacing on the PS grafted surface. These results may imply that the template prepared by patterning the PS-grafted layer is more suitable for the directed self-assembly of PMMA-*b*-PMAPOSS compared to that fabricated employing the substrate with the PMAPOSS-grafted layer. However, for thorough understanding of the effect, the dependences on M_n and/or grafting density of the grafted polymer have to be studied.

4.3.6 Directed Self-assembly of PMMA-*b*-PMAPOSS with Density Multiplication.

The primary motivation for use directed BCP self-assembly is to enhance the achievable lithographic resolution. With the use of lower molecular weight BCPs, I examine the ability to multiply the density of the lithographic chemical pattern arrays. I examined the directed self-assembly of $PMMA_{25}$-*b*-$PMAPOSS_{13}$ with d_0 = 12.4 nm on the chemically patterned PS-OH templates with d_S = 26 nm under CS2 solvent annealing. $PMMA_{25}$-*b*-$PMAPOSS_{13}$ films, of 9 nm thickness, were annealed under CS_2 vapor with swelling factors of t_{DS} = 130, 140, and 150%. In the swollen state, the film thicknesses were expected to be about 12, 13,

and 14 nm at t_{DS} = 130, 140, and 150%, respectively, which nearly correspond to d_0 of the $PMMA_{25}$-*b*-$PMAPOSS_{13}$ BCP.

Figure 4-17(a), (b) and (c) present the SEM images and the corresponding 2D-FFT images of the thin films of $PMMA_{25}$-*b*-$PMAPOSS_{13}$ solvent-annealed on chemically patterned templates with $d_S = 26 \text{ nm} \approx 2d_0$ at t_{DS} = 130, 140, and 150%, respectively. Figure 4-17(a) shows the film annealed at t_{DS} = 130%. Here the $PMMA_{25}$-*b*-$PMAPOSS_{13}$ self-assembled to form a dot structure of PMMA, but the accompanying 2D-FFT image shows on halos indicating the lack of long range order in the array. Under solvent annealing a swell factor of t_{DS} = 130% components did not have sufficient mobility to fully order. Figure 4-17(b) shows the $PMMA_{25}$-*b*-$PMAPOSS_{13}$ film on the PS chemically patterned substrate, with d_S = 26 nm, annealed with a swelling factor t_{DS} = 140%. Both the SEM image on the left and the 2D-FFT of the image on the right show a long range ordered hexagonal array of dots with lattice spacing of 13.4 nm, which was a almost half of the d_S value (= 26 nm) of the template. In contrast, the film annealed with a swelling factor of t_{DS} = 150%, shown in Figure 4-17(c) shows a distorted hexagonal lattice pattern and streaks on the spots in the accompanying 2D-FFT of the image. These results show that solvent annealing with a swell factor of t_{DS} = 140% is optimal for the directed self-assembly of $PMMA_{25}$-*b*-$PMAPOSS_{13}$ with density multiplication by a factor of four.

To evaluate the orientation distribution of the lattice patterns in Figure 4-17, I examined the azimuthal distribution of the first-order peak intensity in the 2D-FFT images. Figure 4-18 shows the azimuthal angle, ψ, dependence of the intensity, I, of the first-order peak positions in the 2D-FFT images shown in Figure 4-17. Peaks were observed at every 60 degrees of the azimuthal angle the samples annealed with swelling factors t_{DS} = 140% and 150%. Little or no azimuthal variation in intensity of the first order ring was observed from the sample annealed with swelling factor, t_{DS} = 130%. The azimuthal angular widths of the peaks of the sample annealed with a t_{DS} = 140% swelling factor were narrower than those of

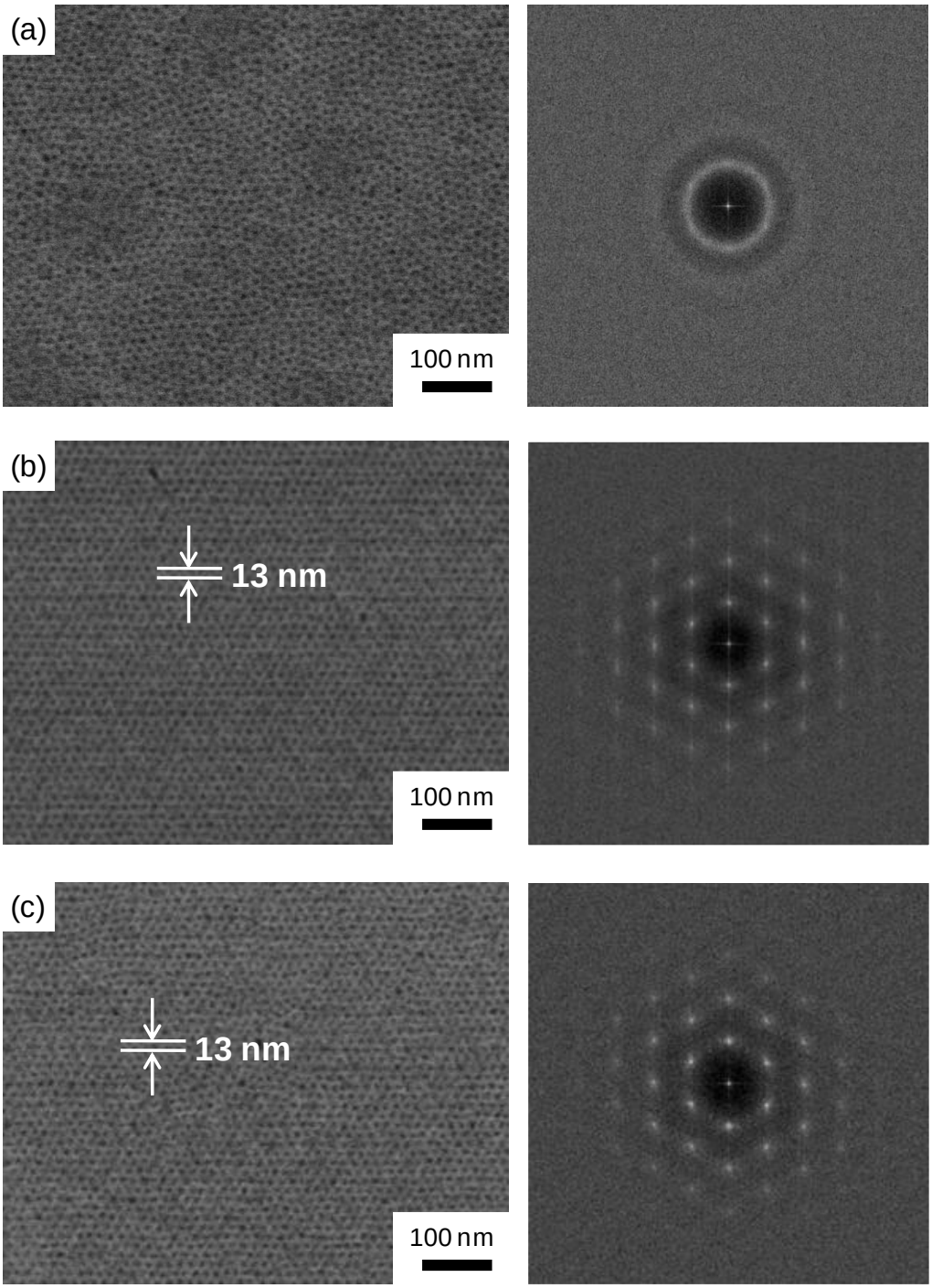

Figure 4-17. SEM images and the corresponding 2D-FFT images of the $PMMA_{25}$-*b*-$PMAPOSS_{13}$ thin films solvent-annealed on the chemically prepatterned template with ds = 2d0 = 26 nm at various t_{DS}. (a) t_{DS} = 130%, (b) t_{DS} = 140%, and (c) t_{DS} = 150%. The film thickness is 9 nm. The chemically patterned templates were fabricated employing PS-OH grafted layer.

the sample annealed with a swelling factor of t_{DS} = 150%. The widths, w, obtained by fitting the peaks at 180° with Gaussian function,

$$I = I_0 + A\exp\left\{-\left(\frac{\psi - \psi_0}{w}\right)^2\right\}$$

were 5.8° and 9.2° for the samples annealed with swelling factors of t_{DS} = 140% and 150%, respectively. The results of the $PMMA_{25}$-*b*-$PMAPOSS_{13}$ ordering on the chemically patterned PS-OH template are summarized in Table 4-4. The length scale of the lithographically directed patterns lattice spacing was 13.4 nm as compared to a 12.4 nm length scale of the unguided block copolymer lattice spacing on the substrates. The standard deviation, σ, of the center-to-center distance of the dots in the self-assembled structures can be compared with that for the template pattern, σ_{eb}, listed in Table 4-3. The spacing σ values of the solvent annealed lattices with swelling factors of t_{DS} = 140% and 150% were calculated to be 1.5 nm and 1.7 nm, respectively. The self-assembled lattice spacing σ's were 20-30% smaller than the σ_{eb} values of the chemically patterned template (d_S = 26 nm), which was 2.2 nm. As can be expected, σ values at t_{DS} = 140% were found to be the smallest and significantly smaller than the σ_{eb} value of the underlying chemically patterned template at one quarter the BCP pattern density. The lower perfection exhibited by the BCP annealed with a swelling factor of t_{DS} = 150% than that of the BCP annealed with a swelling factor of t_{DS} = 140% may be caused by a slight difference in the lattice spacing of the self-assembled structure at the swollen state. Further work, such as *in-situ* grazing incidence small-angle X-ray scattering in the swollen BCP may elucidate the result.

The density multiplication occurs with PMMA dots interpolating between dots in the substrate chemically patterned template pattern and the placement accuracy of the quadruple density pattern is 20-30% better than that of the original lithographic pattern on the template. The pattern density multiplication can be achieved by careful optimization of the amount of BCP swelling during solvent annealing

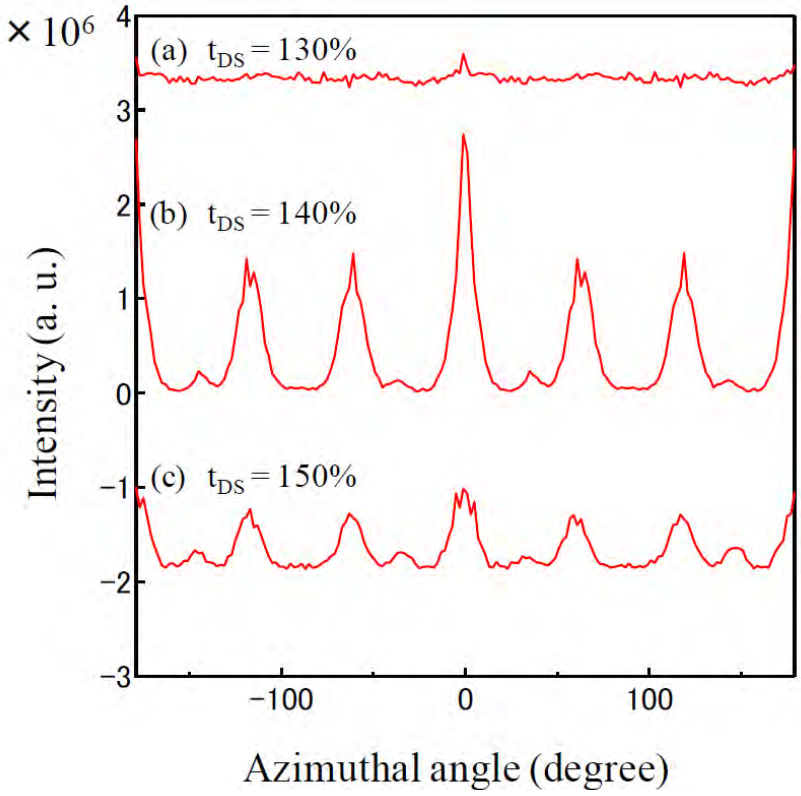

Figure 4-18. Azimuthal angle dependence of the first-order peak intensity of the 2D autocorrelation pattern from the 2D-FFT images of the $PMMA_{25}$-*b*-$PMAPOSS_{13}$ thin films solvent-annealed on the chemically patterned templates with $d_S = 2d_0 = 26$ nm at various t_{DS}. (a) $t_{DS} = 130\%$, (b) $t_{DS} = 140\%$, and (c) $t_{DS} = 150\%$.

Table 4-4. Quantitative Comparison of d, σ, and w among the Self-Assembled Structures of $PMMA_{25}$-*b*-$PMAPOSS_{13}$ on the Chemically Patterned Templates with $d_S = 2d_0 = 26$ nm

t_{DS}	Self-assembled structure		
	d_{obs}	σ	w
130%	13.4 nm	-	-
140%	13.4 nm	1.5 nm	5.8°
150%	13.0 nm	1.7 nm	9.2°

4.3.7 Effects of the Lattice Mismatch between d_S and d_0 on Density Multiplication.

Next, I investigated the effect of lattice mismatch between the $PMMA_{25}$-*b*-$PMAPOSS_{13}$ BCP length scale and that of the original lithographic chemically patterned template pattern. The lattice spacing of $PMMA_{25}$-*b*-$PMAPOSS_{13}$ self-assembled on the Si substrate without a chemically patterned template was found to be d_0 = 12.4 nm. I examined the directed assembly of the $PMMA_{25}$-*b*-$PMAPOSS_{13}$ with CS_2 solvent annealing with chemically patterned template pre-patterns slightly above and below the value of $2d_0$ for 4× density multiplication. The $PMMA_{25}$-*b*-$PMAPOSS_{13}$ films were spun on chemically patterned PS-OH layers on Si substrates and annealed in CS_2 with a swelling factor of 140%. The length scales of the hexagonal lattices on the chemically patterned templates were, d_S = 23, 24 and 28 nm. The SEM images and the associated 2D-FFT images of the resulting ordered BCP are shown in Figure 4-19.

In Figure 4-19(a), is the resulting directed self assembled BCP lattice on a chemically patterned template with a single hexagonal lattice pattern spacing of d_S = 23 nm. From the first-order peak positions in the circular-averaged 2D-FFT image, the dot lattice spacing of the self-assembled structures on the template was determined d_{obs} = 13.2 nm. Also note that the orientation of the BCP self-assembled lattice pattern was rotated by 30° with respect to that of the template pattern as schematically illustrated in Figure 4-20. Therefore, the interpolation of the dots occurred as illustrated in Figure 4-20, resulting in the hexagonal lattice with the orientation rotated by 30° with respect to the chemical pattern and the density of the self-assembled BCP is three times the density of the underlying chemically patterned template.[25]

In Figure 4-19(b), the underlying chemically patterned template pattern was 24 nm in interplane spacing and 28 nm in the dot-to-dot spacing on axis. The directed BCP, assembled in a single hexagonal lattice as shown the Figure 4-19(b). The corresponding 2D-FFT image exhibits a spot-like pattern with 3 orders of peaks. Analysis of the first order

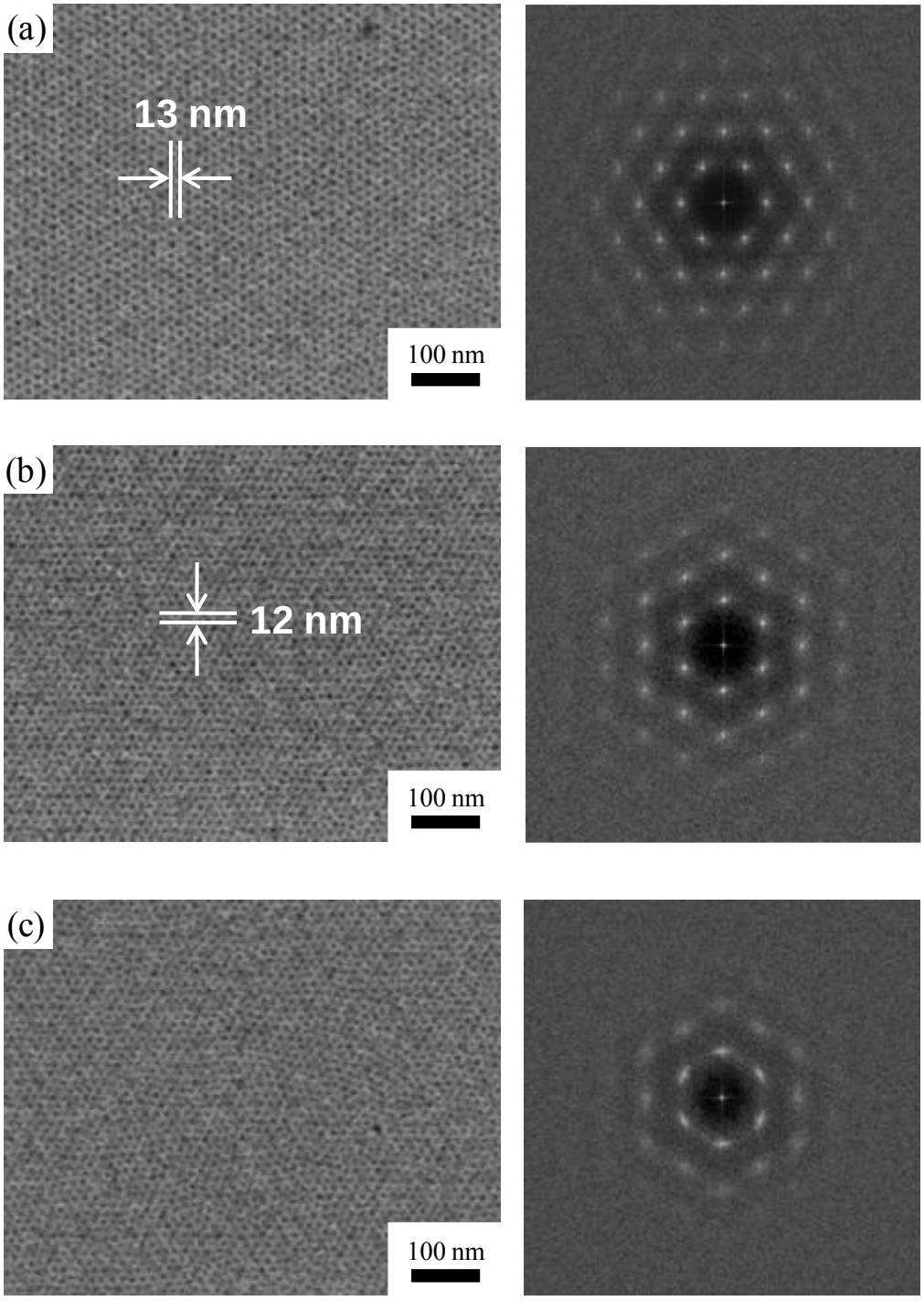

Figure 4-19. SEM images and the corresponding 2D-FFT images of the $PMMA_{25}$-*b*-$PMAPOSS_{13}$ thin films solvent-annealed at t_{DS} = 140% on the chemically patterned template with $d_S \approx 2d_0$. (a) d_S = 23 nm, (b) d_S = 24 nm, and (c) d_S = 28 nm. The film thickness is 9 nm. The chemically prepatterned templates were fabricated employing the PS-OH grafted layer.

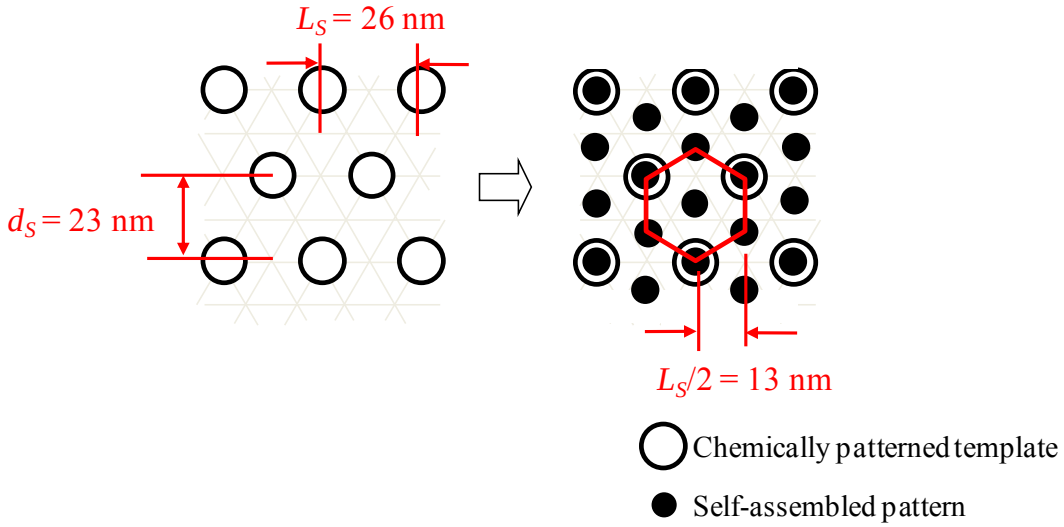

Figure 4-20. Schematic illustration of the density multiplication for the case shown in Figure 19(a). The orientation of the hexagonal lattice of the self-assembled structure (filled circles) is rotated by 30° with respect to that of the chemically patterned template with d_S = 23 nm (open circles). The lattice spacing of the self-assembled structure, d_{obs}, corresponds to a half of the nearest center-to-center spacing of the dot like holes (open circles) in the chemically patterned template, L_S.

peaks gave an average lattice inter row spacing of d_{obs} = 12.3 nm, which was a half of the value of the lithographically defined chemical pattern, d_S = 24 nm. As determined above, the lattice spacing of the BCP self-assembled structure on the Si, d_0, was 12.4 nm. In this case, the directed BCP lattice had the same spacing as the spacing of the BCP lattice on Si. Areal density of hexagonal lattice pattern with lattice inter row spacing of d_{obs} = 12.3 nm achieved in this study corresponds to 3.7 Tdot/inch^2. Most importantly I have demonstrated successful template pattern density multiplication with a PMMA-*b*-PMAPOSS BCP to an ultrahigh pattern density.

Figure 4-19(c) shows the directed self-assembled PMMA$_{25}$-*b*-PMAPOSS$_{13}$ BCP and its 2D-FFT image on a chemically patterned template with d_S = 28 nm. The mismatch chemical pattern on the substrate is further from the period of the PMMA$_{25}$-*b*-PMAPOSS$_{13}$ BCP lattice on Si than the sample in Figure 4-19(a) and (b), and the long-range order of the

self-assembled structure looks worse. However, the closer observation of the 2D-FFT image in Figure 4-19(c) shows the superposition of two different hexagonal lattices different lattice spacings shown in Figure 4-21, namely d_{obs} = 12.3 nm and 13.8 nm. The first-order peaks for lattice spacing d_{obs} = 12.3 nm contain streaks, which suggest much broader orientation distribution of the hexagonal lattice than those shown in Figure 4-19(a) and (b). This result suggests that a number of hexagonal lattice of the self-assembled structure with d_{obs} = 12.3 nm with slightly different orientations give rise to the arc-like peaks. It should be noted that d_{obs} = 12.3 nm is almost identical to d_0 = 12.4 nm of the self-assembled structure on the Si substrate, suggesting that the lattice spacing of the majority of the self-assembled structures was not affected by the template lattice spacing. The first order peaks of the lattice pattern

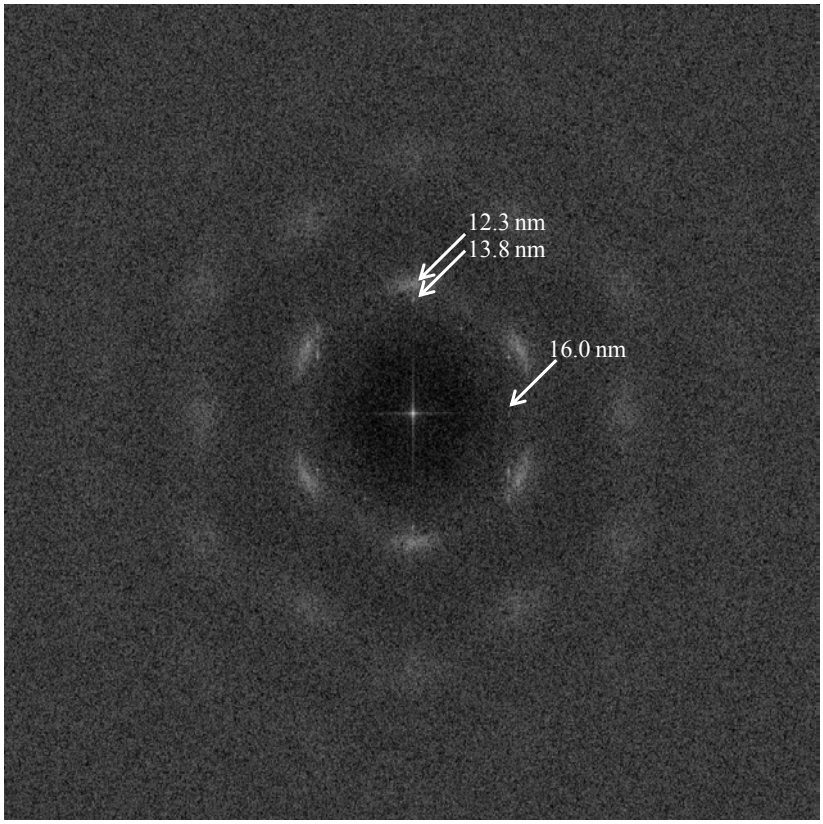

Figure 4-21. The 2D-FFT image of the $PMMA_{25}$-*b*-$PMAPOSS_{13}$ thin film solvent-annealed on the chemically patterned template with d_S = 28 nm. The image has been processed by enlarging and contrast-enhancing the 2D-FFT image presented in Figure 19(c).

with d_{obs} = 13.8 nm, appear as the sharp points in the 2D-FFT image as shown in Figure 4-21. In the latter lattice the spacing is ~ 2× the lithographic pattern spacing and the BCP matrix stretched by 11% (d_{obs}/d_0 = 13.8/12.4 = 1.11) relative to lattice spacing of the self-assembled structure on the Si substrate as the result of the chemically patterned template with d_S = 28 nm. Thus, Figure 4-17(b) and Figure 4-19 show one region where the self-assembled BCP is directed by the template with d_S = 26 nm and another which is directed by d_S =23 nm. Both lattices formed a ~ 4× density multiplication of the original lithographic pattern, but the orientation in the d_{obs} = 13.8 nm is better controlled.

From these results, the reduction of the interface interaction enthalpy between the template surface and the polymer can overcome the loss of the conformational entropy of the block chains up to a 8% (d_{obs}/d_0 = 13.4/12.4 = 1.11) stretch in terms of d_{obs}/d_0 induced by the template pattern with d_S.

4.4 Conclusion

I have demonstrated that the directed self-assembly of POSS containing BCP, PMMA-*b*-PMAPOSS, can realize a 4× density multiplication over the chemically patterned substrate by solvent annealing with CS_2, thereby achieving the dot density of about 4 Tbit/inch^2. The key factor for the successful density multiplication with a sufficient long-range order is to control the degree of swelling during the solvent annealing process because the lattice spacing of the self-assembled structure of the PMMA-*b*-PMAPOSS film is sensitive to the degree of swelling. It was observed that the lattice spacing of the self-assembled structure changed slightly depending on the degree of swelling even if the same chemically patterned substrate with the hexagonally packed dot pattern was used. The mismatch in the lattice spacing between the template pattern and the BCP microdomains causes a reduction in the long-range order of the self-assembled structure. The swelling with CS_2 is necessary also to provide sufficient mobility to PMMA-*b*-PMAPOSS for self-assembling. Therefore, control of the degree of swelling during the solvent annealing process under the optimum condition is critical.

Furthermore, I showed that the PMMA-*b*-PMAPOSS thin film could undergo morphological transition from cylinders to spheres depending on the degree of swelling as well as the molecular weight of PMMA-*b*-PMAPOSS due to the selectivity of CS_2 to PMAPOSS. It was found that the choice of the material for the grafting layer in the chemical heteroepitaxy was also important. PS-OH was found to be more suitable than PMAPOSS-OH as a chemically patterned template layer for making the defect-free self-assembled structures of PMMA-*b*-PMAPOSS. The self-assembled structure of PMMA-*b*-PMAPOSS can tolerate 12% and 8% mismatch between the lattice spacing of the chemically patterned template and the inherent lattice spacing of the BCP with and without a 4× density multiplication, respectively.

The results show that solvent annealing can be applied to the directed self-assembly with a density multiplication under a controlled annealing environment. With solvent annealing, a wider variety of BCPs can be utilized in the lithographic applications than thermal annealing. The relative selectivity of the solvent for each of the two blocks allows further control of the morphology. In this study, I have limited the study to apply the technique only to the hexagonally packed dot pattern, but the results strongly support the possibility to adapt the technique to other domain structures as well as to more complex features.

4.5 Supporting Information Paragraph.

Materials and Methods.

To modify the Si surface with PMAPOSS, I was supported by Prof. Hayakawa and coworkers, Tokyo Institute of Technology, with synthesis of hydroxyl-terminated PMAPOSS. First, a DPE derivative (DPE-OTMS), possessing a pendant hydroxyl group protected by a trimethylsilyl group (TMS), was synthesized. Protection is necessary because the proton in the hydroxyl group can deactivate the active carbanion end group. PMAPOSS-OTMS was synthesized with the protected DPE-OTMS via living anionic polymerization, and then the TMS was removed under acidic conditions to obtain PMAPOSS-OH.

Synthesis of PMAPOSS-OH.

Scheme S1 shows the synthesis of DPE-OTMS. DPE-OTMS was synthesized using 3-bromobenzaldehyde as the starting material through six steps. Scheme S2 shows the synthesis of PMAPOSS-OH. 40 mL of tetrahydrofuran (THF) was transferred to a glass reactor containing 20 mg of dry LiCl (0.48 mmol), and the glass reactor was cooled to -78°C. 0.5 mL of 1.0 M *sec*-BuLi solution in hexane/cyclohexane was added and the solution was left to stand for 30 min at room temperature. The reactor was cooled back to -78°C, and 140 μL of 1.0 M *sec*-BuLi solution in hexane/cyclohexane was added. Next, 140 μL of DPE-OTMS (144 mg, 0.5 mmol) was added to the reactor and the solution was stirred for 30 min. 1.8 g of MAPOSS (1.9 mmol), predissolved in THF (4.0 mL), was transferred from the monomer reservoir to the polymerization flask via a cannula and then vigorously stirred for 7 h. 10 mL of the MeOH solution, a mixture of hydrochloride aqueous solution and MeOH, was added to the reactor. The reaction was quenched by the addition of 10 mL of 1:1 methanol:concentrated hydrochloric acid solution. The polymer was then precipitated into MeOH, filtered, and dried under vacuum at 80°C for 24 h.

Scheme S1. Synthesis of DPE-OTMS.

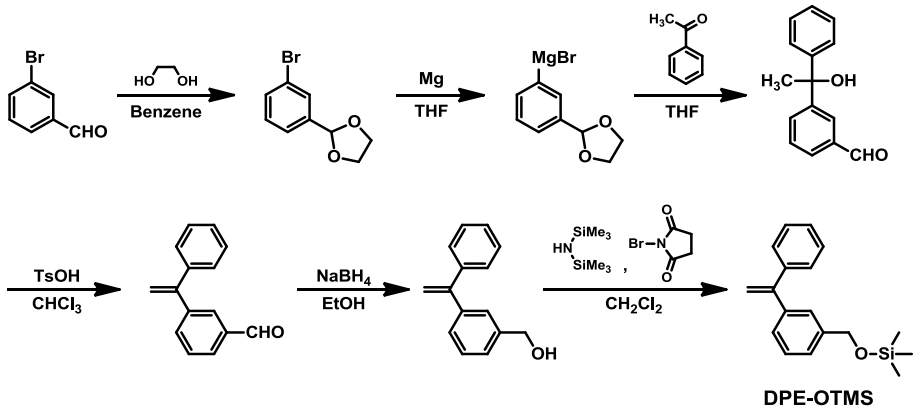

Scheme S2. Synthesis of PMAPOSS-OH.

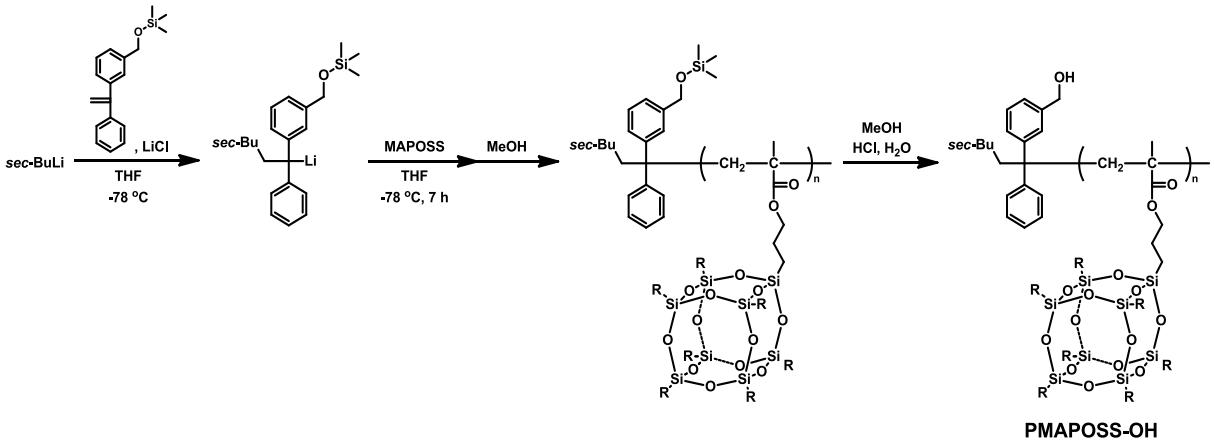

Characterization.

Gel permeation chromatography (GPC) was performed with THF as the eluent at 40°C with a flow rate of 1mL min^{-1}. Relative molecular weights are quoted with monodispersed polystyrenes as the standards. The structure of the DPE-OTMS and PMAPOSS-OH was determined by ^{1}H and ^{13}C NMR spectra, as shown in Figure S1. ^{1}H and ^{13}C NMR spectra in $CDCl_3$ were recorded on a JEOL JNM-AL 300 spectrometer at 300 and 75 MHz, respectively.

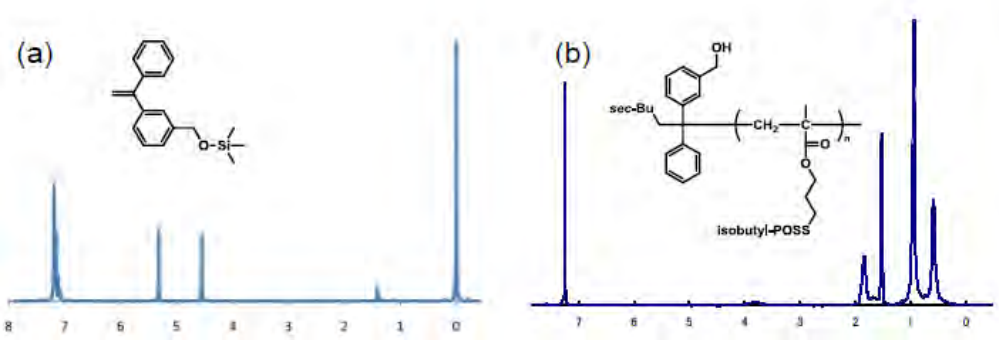

Figure S1. ^{1}H NMR spectra of (a) DPE-OTMS and (b) PMAPOSS-OH.

4.6 References

1. Park, M.; Harrison, C.; Chailin, P. M.; Register, R. A.; Adamson, D. H. *Science* **1997**, *276*, 1401.
2. Kim, H.-C.; Park, S.-M.; Hinsberg, W. D. *Chem. Rev.* **2010**, *110*, 146.
3. Galatsis, K.; Wang, K. L.; Ozkan, M.; Ozkan, C. S.; Huang, Y.; Chang, J. P.; Monbouquette, H. G.; Chen, Y.; Nealey, P. F.; Botros, Y. *Adv. Mater*. **2010**, *22*, 769.
4. Khandpur, A. K.; Forster, S.; Bates, F. S.; Hamely, I. W.; Ryan, A. J.; Bras, W.; Almdal, K.; Mortensen, K. *Macromolecules* **1995**, *28*, 8796.
5. Bate, F. S.; Fredrickson, G. H. *Annu. Rev. Phys. Chem.* **1990**, *41*, 525.
6. Hashimoto, T., In *Thermoplastic Elastmers*; Legge, N. R.; Holden, G., Schroeder, H. E., Eds.; Hanser: Vienna, 1996.
7. Matsen, M. W.; Schick, M. *Phys. Rev. Lett.* **1994**, *72*, 2660.
8. Takenaka, M.; Wakada, T.; Akasaka, S.; Nishitsuji, S.; Saijo, K.; Shimizu, H.; Kim, M. I.; Hasegawa, H. *Macromolecules* **2007**, *40*, 4399.
9. Bita, I.; Yang, J. K. W.; Jung, Y. S.; Ross, C. A.; Thomas, E. L.; Berggren, K. K. *Science* **2008**, *321*, 939.
10. Black, C. T.; Guarini, K. W.; Milkove, K. R.; Baker, S. M.; Russell, T. P.; Tuominen, M. T. *Appl.Phys.Lett.* **2001**, *79*, 409.
11. Segalman, R. A.; Yokoyama, H.; Kramer, E. J., *Adv. Mater.* **2001**, *13*, 1152.
12. Sundrani, D.; Sibener, S. J. *Macromolecules* **2002**, *35*, 8531.
13. Cheng, J. Y.; Ross, C. A.; Thomas, E. L.; Smith, H. I.; Vancso, G. J. *Appl. Phys. Lett.* **2002,** *81*, 3657.
14. Cheng, J. Y.; Mayes, A. M. *Nat. Mater.* **2004**, *3*, 823.
15. Xiao, S. G.; Yang, X. M.; Edwards, E. W.; La, Y. H.; Nealey P. F. *Nanotechnology* **2005**, *16*, S324.

16. Chen, F.; Akasaka, S.; Inoue, T.; Takenaka, M.; Hasegawa, H.; Yoshida, H. *Macromol. Rapid. Commun.* **2007**, *28*, 2137.

17. Rockford, L.; Liu, Y.; Mansky, P.; Russell, T. P.; Yoon, M.; Mochrie, S. G. J. *Phys. Rev. Lett.* **1999**, *82*, 2602.

18. Kim, S. O.; Solak, H. H.; Stoykovich, M. P.; Ferrier, N. J.; de Pablo, J. J.; Nealey, P. F. *Nature* **2003**, *424*, 411.

19. Edwards, E. W.; Stoykovich, M. P.; Solak, H. H.; Nealey, P. F. *Macromolecules* **2006,** *39*, 3598.

20. Welander, A. M.; Kang, H.; Stuen, K. O.; Solak, H. H; Müller, M.; de Pablo, J. J.; Nealey, P. F. *Macromolecules* **2008,** *41*, 2759.

21. Ruiz, R.; Kang, H.; Detcheverry, F. A.; Dobisz, E.; Kercher, D. S.; Alberecht, T. R.; de Pablo, J. J.; Nealey, P. F. *Science* **2008**, *321*, 936.

22. Cheng, J. Y.; Rettner, C. T.; Snaders, D. P.; Kim, H. C.; Hinsberg, W. D. *Adv. Mater.* **2008**, *20*, 3155.

23. Tada, Y.; Akasaka, S.; Yoshida, H.; Hasegawa, H.; Dobisz, E.; Kercher, D.; Takenaka, M. *Macromolecules*, **2008**, *41*, 9267.

24. Tada, Y.; Akasaka, S.; Takenaka, M.; Yoshida, H.; Ruiz, R.; Dobisz, E.; Hasegawa, H. *Polymer* **2009**, *50*, 4250.

25. Xiao, S.; Yang, X. M.; Park, S.; Weller, D.; Russell, T. P. *Adv. Mater.* **2009**, *21*, 2516.

26. Wan., L.; Yang, X. M. *Langmuir* **2009**, *25*, 12408.

27. Cheng, J. Y.; Snaders, D. P.; Truong, H. D.; Harrer, S.; Friz, A.; Holmes, S.; Colburn, M.; Hinsberg W. D. *ACS Nano* **2010**, *4*, 4815.

28. Stoykovich, M. P.; Kang, H.; Daoulas, K. C.; Liu, G.; Liu, C.-C.; Pablo, J. J.; Muller, M.; Nealey, P. F. *ACS Nano* **2007**, *1*, 168.

29. Ruiz, R.; Dobisz, E.; Albrecht, T. R. *ACS Nano* **2011**, *5*, 79.

30. Kang, H.; Crag, G. S. W.; Nealey, P. F. *J. Vac. Sci. Technol. B* **2008**, *26*, 2495.

31. Liu, G.; Thomas, C. S.; Craig, G. S. W.; Nealey, P. F. *Adv. Funct. Mater.* **2010**, *20*, 1251.

32. Jung, Y. S.; Ross, C. A. *Adv. Mater.* **2009**, *21*, 2540.

33. Jung, Y. S.; Ross, C. A. *Nano. Lett.* **2007**, *7*, 2046.

34. Jung, Y. S.; Chang, J. B.; Verploegen, E.; Berggren, K. K.; Ross, C. A. *Nano. Lett.* **2010**, *10*, 1000.

35. Park, S.; Lee, D. H.; Xu, J.; Kim, B.; Hong, S. W.; Jeong, U.; Xu, T.; Russell, T. P. *Science* **2009**, *323*, 1030.

36. Takenaka, M.; Aburaya, S.; Akasaka, S.; Hasegawa, H.; Hadjichristidis, N.; Sakellariou, G.; Tada, Y.; Yoshida, H. *J. Polym. Sci. Part B.: Polym. Phys.* **2010**, *48*, 2297.

37. Mori, K.; Hasegawa, H.; Hashimoto, T. *Polymer* **1990**, *31*, 2368.

38. Bosworth, J. K.; Paik, M. Y.; Ruiz, R.; Schwartz, E. L.; Huang, J. Q.; Ko, A. W.; Smilgies, D.-M.; Black, C. T.; Ober, C. K. *ACS Nano* **2008**, *2*, 1396.

39. Paik, M. Y.; Bosworth, J. K.; Smilges, D.-M.; Schwartz, E. L.; Andre, X.; Ober, C. K. *Macromolecules*, **2010**, *43*, 4253.

40. Saraf, R. F.; Niu, S.; Stumb, E. *Appl. Phys. Lett.* **2002**, *80*, 4425.

41. Niu, S.; Saraf, R. F. *Macromolecules* **2003**, *36*, 2428.

42. Bosworth, J. K.; Dobisz, E.; Ruiz, R. *J. Photopolym. Sci. Technol.* **2010**, *23*, 145.

43. Hirai, T.; Leolukman, M.; Hayakawa, T.; Kakimoto, M.; Gopalan, P. *Macromolecules* **2008**, *41*, 4558.

44. Hirai, T.; Leolukman, M.; Jin, S.; Goseki, R.; Ishida, Y.; Kakimoto, M.; Hayakawa, T.; Ree, M.; Gopalan, P. *Macromolecules* **2009**, *42*, 8835.

45. Hirai, T.; Leolukman, M.; Jin, S.; Liu, C. C.; Han, E.; Kim, Y. J.; Ishida, Y.; Hayakawa, T.; Kakimoto, M.; Nealey, P. F.; Gopalan, P. *Adv. Mater.* **2009**, *21*, 4334.

46. Kim, B.; Ryu, D. Y.; Pryamitsyn, V.; Ganesan, V. *Macromolecules* **2009**, *42*, 7919.

47. Ishida, Y.; Tada, Y.; Hirai, T.; Goseki, R.; Kakimoto, M.; Yoshida, H.; Hayakawa, T. *J. Photopolym. Sci. Technol.* **2010**, *23*, 155.

48. Fourier transfer of a real space image results in a matrix of complex number, which cannot be plotted in a 2D plane. Therefore, its 2D power spectrum density function was plotted and defined as a 2D-FFT image.
49. Hanley, K. J.; Lodge, T. P.; Huang, C.-I. *Macromolecules* **2000**, *33*, 5918.
50. Tokarev, I.; Krenek, R.; Burkov, Y.; Schmeisser, D.; Sidorenko, A.; Minko, S.; Stamm, M. *Macromolecules* **2005**, *38*, 507.

SUMMARY

In Chapter 1, I first explained the motivation and the objective of this thesis and reviewed the self-assembly of the block copolymers in bulk and thin films. In particular, I described that the morphology and the orientation of microdomain structure of block copolymer thin films are significantly affected by the interfacial interaction at polymer/air, polymer/substrate, and the film thickness. The microdomain structures of block copolymers are useful to form fine patterns at nano-meter scale due to the self-assembling system. However, many challenges still exist in applying BCPs for practical use in electronics applications. One of the key challenges is to control the morphology and placement of the micorodomain structures. Directed self-assembly of block copolymers, which utilize lithographically defined templates, namely topographic relief structure (graphoepitaxy) or chemically prepatterned surface regions (chemical hetero epitaxy), has attract much attention for solving this problem. To fabricate ultra high density pattern, I dealt with the directed self-assembly of BCPs with chemical hetero epitaxy through this thesis and revealed the effect of the interfacial interaction and the film thickness, and so on, on pattern fidelity under the directed self-assembly process.

In Chapter 2, I demonstrated that the microdomain structure of PS-*b*-PMMA can be well-aligned by chemical hetero epitxy, where the driving force is the interfacial energy between polymer and substrate surface. Actually, cylinder-forming PS-*b*-PMMA self-assembled to form perpendicularly oriented cylinders with a long-range order over arbitrarily large areas on the chemically patterned templates prepared by EB lithography. I also demonstrated that defects in chemically prepatterned substrate can be rectified by self-assembly of block copolymer due to the short-range order of microdomain structure. Furthermore, self-assembly of block copolymer could interpolate points in between chemical lattice pattern, thus multiplying the pattern density which is the hexagonally closed packed

pattern with lattice spacing of 24 nm, corresponding to ca. 1tera dot/inch^2. I found that the block copolymer film thickness is very important to interpolate the lithographic pattern. These results suggest that combination of top-down (EB lithography) and bottom-up (self-assembly) technologies can overcome the limitation of current lithography technique.

In Chapter 3, I demonstrated 9× feature density multiplication by perpendicularly oriented cylinders of PS-*b*-PMMA on chemically prepatterned substrate to enhance the resolution and throughput of EB lithography. I found that the film thickness is confined within a narrow range to attain perpendicularly oriented cylinder of PS-*b*-PMMA on the interpolation points. Furthermore, the tolerance of the lattice mismatch between the template pattern and domain spacing for 9× feature density multiplication was smaller than that for 4× feature density multiplication. I also clarified that the critical dimension formed by the block copolymer domains is independent of that defined by the EB pre-patterned features. These results indicate that the directed self-assembly with feaature density multiplication by using PS-*b*-PMMA cannot only reduce the lattice spacing of chemical pattern but also reduce the pattern radius. Therefore, directed self-assembly can provide alternative route to reduce pattern up to the size which is difficult for current lithography to achieve.

In Chapter 4, I demonstrated the hexagonally closed packed dot pattern with the lattice spacing of 12 nm, corresponding to ca. 4 tera dot/inch^2, by applying POSS containing block copolymer to fabricate ultra high density pattern which cannot be achieved by current lithography. Solvent annealing was applied to form microdomain structure of POSS containing block copolymer. I found that precise control of the degree of swelling during solvent annealing is required to attain the microdmain structure with long-range order. Furthermore, I showed that the morphological transition from cylinders to spheres is induced depending on the degree of swelling as well as the molecular weight of the block copolymer because of the selective solvent. Therefore, these results suggest that the key factor to attain

the successful density multiplication is to control the degree of swelling precisely during solvent annealing. I also showed that the microdomain structures formed on the chemically prepatterned template by solvent annealing could tolerate several percent of the lattice mismatch between the domain spacing of the block copolymer and that of the template.

Finally, I dealt with the directed self-assembly of block copolymers with chemical hetero epitaxy to fabricate ultra high density pattern. The key point to attain the successful directed self-assembly is to control the morphology and orientation of microdomain structure by the interfacial energy, conformational entropy, and so on. The directed self-assembly of block copolymers might be powerful tool to attain nanometer-scale pattern which cannot be achieved by current lithography technique. However, this technique has been including challenges to fabricate the complex pattern. I expect that the directed self-assembly supports the potential application of the technique and drives the breakthrough in the semiconductor industry.

LIST OF PUBLICATIONS

(1) "Directed Self-Assembly of Diblock Copolymer Thin Films on Chemically-Patterned Substrates for Defect-Free Nano-Patterning"

Tada, Y.; Akasaka, S.; Yoshida, H.; Hasegawa, H.; Dobisz, E.; Kercher, D.; Takenaka, M. *Macromolecules* 2008, 41, (23), 9267-9276.

(Chapter 2)

(2) "Nine-fold density multiplication of hcp lattice pattern by directed self-assembly of block copolymer"

Tada, Y.; Akasaka, S.; Ruiz, R.; Dobisz, E.; Takenaka, M.; Hasegawa, H.; Yoshida, H. *Polymer* 2009, 50, (17), 4250-4256.

(Chapter 3)

(3) "Directed Self-Assembly of POSS Containing Block Copolymer on Lithographically Defined Chemical Template with Morphology Control by Solvent Vapor"

Tada, Y.; Yoshida, H.; Ishida, Y.; Hirai, T.; Bosworth, J. K.; Dobisz, E.; Ruiz, R.; Takenak, M.; Hayakawa, T.; Hasegawa, H. *Macromolecules* 2012, 45, (1), 292-304.

(Chapter 4)

(4) "Density Multiplication by Directed Self-assembly of Block Copolymer Binary Blends"

Tada, Y.; Akasaka, S.; Chen, F.; Yoshida, H.; Takenaka, M.; Hasegawa, H. *J. Photopolym. Sci. Tech.* 2009, 22, (2), 229-233.

(Not included in this thesis)

(5) “Directed Self-assembly of Cage Silsesquioxane Containing Block Copolymers via Graphoepitaxy Techniques”

Ishida, Y.; Tada, Y.; Hirai, T.; Goseki, R.; Kakimoto, M.; Yoshida, H.; Hayakawa, T. *J. Photopolym. Sci. Tech.* 2010, 23, (2), 155-159.

(Not included in this thesis)

(6) “Formation of long-range stripe patterns with sub-10-nm half-pitch from directed self-assembly of block copolymer”

Takenaka, M.; Aburaya, S.; Akasaka, S.; Hasegawa, H.; Hadjichristidis, N.; Sakellariou, G.; Tada, Y.; Yoshida, H. *J. Polym. Sci. Part B: Polym. Phys.* 2010, 48, (22), 2297-2301.

(Not included in this thesis)

(7) “Directed Self-assembly with Density Multiplication of Cage Silsesquioxane-containing Block Copolymer via Controlled Solvent Annealing”

Yoshida, H.; Tada, Y.; Ishida, Y.; Hayakawa, T.; Takenaka, M.; Hasegawa, H. *J. Photopolym. Sci. Tech.* 2011, 24, (5), 577-580.

(Not included in this thesis)

(8) “Cross-sectional Image of Block Copolymer Thin Films on Chemically Patterned Surfaces”

Liu, G.; Kang, H.; Craig, G. S. W.; Detcheverry, F.; de Pablo, J. J.; Nealey, P. F.; Tada, Y.; Yoshida, H. *J. Photopolym. Sci. Tech.* 2011, 23, (2), 149-154.

(Not included in this thesis)

(9) “Analysisi on Deterioration Mechanism of Release Layer in Nanoimprint Process”

Tada, Y.; Yoshida, H.; Miyauchi, A. *J. Photopolym. Sci. Tech.* 2007, 20, (4), 545-548.

(Not included in this thesis)

(10) “Photoresponsive Change of the Surface Potential Generated by Helical Peptide Self-Assembled Monolayers”

Tada, Y.; Morita, T.; Umemura, Junzo.; Iwamoto, M.; Kimura, S. *Polym. J.* 2005, 37, (8), 599-607.

(Not included in this thesis)

ACKNOWLEDGEMENTS

This thesis is based upon the study carried out under the guidance of Professor Hirokazu Hasegawa, at Department of Polymer Chemistry, Graduate School of Engineering, Kyoto University, from 2009 to 2012.

The author would like to express his sincere gratitude to Professor Hirokazu Hasegawa for his continuous guidance, encouragement, valuable suggestions and discussions in the course of his studies.

The author also wishes to thank Professor Mikihito Takenaka, at Department of Polymer Chemistry, Graduate School of Engineering, Kyoto University, for his kind advices, valuable comments and discussion in the course of his studies.

The author would like to be grateful to Professor Teruaki Hayakawa, at Department of Organic and Polymeric Materials, Tokyo Institute of Technology, for his kind advices, valuable comments and discussions.

The author wishes to express his thanks to Dr. Ricardo Ruiz, Dr. Elizabeth Dobisz, Dr. Joan K. Bosworth, at San Jose Research Center, Hitachi Global Storage Technologies, for their kind collaborations, supports in experimental, and valuable discussions.

The author is deeply grateful to Dr. Satoshi Akasaka, Mr. Shusuke Aburaya, and Mr. Kenichiro Yamaguchi, at Department of Polymer Chemistry, Graduate School of Engineering, Kyoto University, for their supports in experimental and valuable discussions.

The author would like to be grateful to Dr. Tomoyasu Hirai, Dr. Yoshihito Ishida, Mr. Haruka Mikami, Mr. Mizuki Sato, Ms. Chiharu Hirano, at Department of Organic and Polymeric Materials, Tokyo Institute of Technology, for their kind collaborations, supports in experimental, and valuable discussions.

The author is deeply grateful to Professor Paul F. Nealey, Dr. Huiman Kang, Dr. Chi-Chun Liu, at Department of Chemical and Biological Engineering, University of Wisconsin, for their kind collaborations, supports in experimental, and valuable discussions.

The author deeply acknowledges to Dr. Hiroshi Yoshida, at Hitachi Ltd., for his kind advices, valuable comments and discussion in the course of his studies.

The author wish to express his thanks to Dr. Kohhei Aida, at Hitachi Ltd., for supports in experimental and valuable discussions.

The author also thank to secretaries of Hasegawa Laboratory, Ms. Kayo Kawamura and Ms. Naoko Oda, for their kind care and helps.

Part of this work was funded by the “Development of Nanobit Technology for Ultra-high Density Magnetic Recording (Green IT project)” of NEDO, Japan.

Finally, and most of all, the author expresses his sincere gratitude to his parents, Toshihiko and Yumiko Tada, and his wife, Mizuho Tada for their unlimited supports and encouragements during his studies.

January, 2012 Yasuhiko Tada